UNIVERSITY OF COPENHAGEN
FACULTY OF SCIENCE

PhD thesis

Nanomechanical Slot Waveguide Phase Shifters for Integrated Quantum Photonics

Clara Celeste Qvotrup

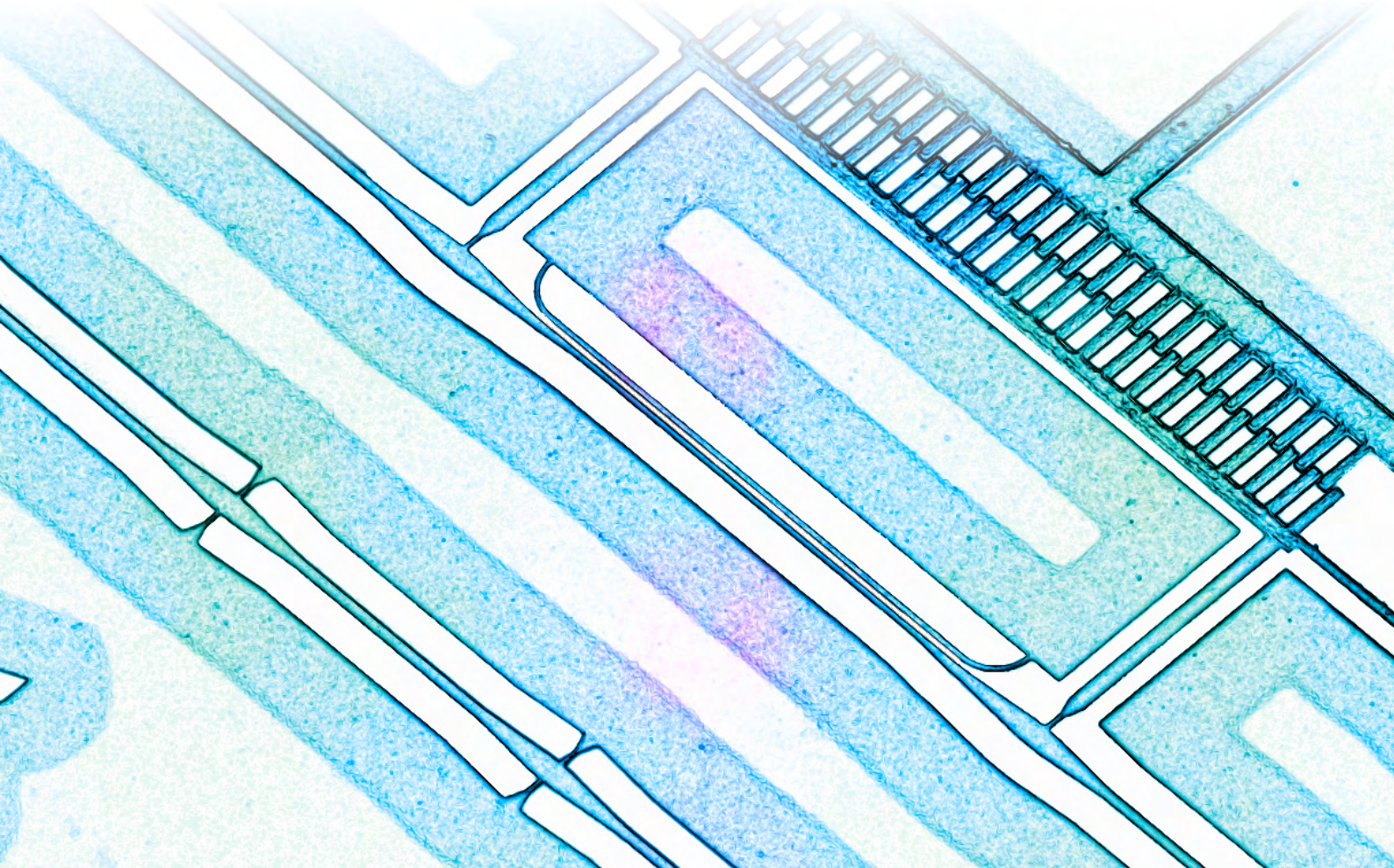

Nanomechanical Slot Waveguide Phase Shifters for Integrated Quantum Photonics

Author: Clara Celeste Qvotrup

Advisor: Assoc. Prof. Leonardo Midolo

UNIVERSITY OF COPENHAGEN

Quantum Photonics
Center for Hybrid Quantum Networks (Hy-Q
The Niels Bohr institute

This thesis has been submitted to
the PhD School of The Faculty of Science
University of Copenhagen
January 2025

Abstract

Integrated photonic circuits with embedded single-photon emitters represent a promising platform for quantum computing. Specifically, suspended gallium arsenide (GaAs) membranes with self-assembled indium arsenide (InAs) quantum dots (QDs) enable the emission of highly indistinguishable and pure single photons directly into guided modes with near-unit coupling efficiencies.

The implementation of a quantum photonic circuit requires reliable, low-loss reconfigurable elements such as beam splitters and phase shifters. Thermo- and electro-optic routing, while well-developed techniques, both suffer critical shortcomings for the GaAs platform utilizing light in the InAs QD emission range (920-945 nm) while operating under cryogenic conditions $T \leq 10\,\mathrm{K}$, as the thermo-optic coefficient goes towards zero at low temperatures, while electro-optic routing induces a large loss via the Franz-Keldysh effect due to the proximity to the bandgap. Nano-opto-electro-mechanical systems (NOEMS) provide a strategy for active control of compact reconfigurable elements compatible with the desired platform. Slot waveguides, comprising two narrow, high-index-material cantilevers, guide light through the narrow, low-index gap between the cantilevers. The strong non-linear gap dependence of the guided mode's effective refractive index enables precise phase control via electromechanical actuation. This thesis presents the design, fabrication, and characterization of a slot waveguide phase shifter employing a comb drive actuator.

The loss associated with slab-to-slot waveguide couplers is extensively analyzed both theoretically and experimentally. A broadband phase shifter with a slot waveguide length of $10\,\mu\mathrm{m}$ and a total footprint of less than $(60 \times 20\,\mu\mathrm{m}^2)$ was fabricated and characterized, and exhibited a half-wave-voltage length product of $V_\pi L = 7.7 \cdot 10^{-3}\,\mathrm{V \cdot cm}$ at room temperature and $V_\pi L = 12 \cdot 10^{-3}\,\mathrm{V \cdot cm}$ at cryogenic temperatures. Reduced phase shifts at low temperatures are likely due to factors such as temperature-induced stiffening of the gold membrane leading to smaller cantilever displacements.

Lastly, the thesis presents a circuit that uses a NOEMS phase shifter to dynamically modulate the emission properties of a quantum dot by altering the optical path length to a distant mirror, tuning its lifetime and intensity via the local density of states. This capability was experimentally confirmed, which revealed variations in the intensity and decay rate visibilities spanning $\nu_I = 0.42$–0.83 and $\nu_\tau = 0.08$–0.27 across quantum dots in different lateral positions. This work marks a significant step toward scalable integrated circuits for the manipulation of quantum emitters at low temperatures.

Sammenfatning

Integrerede fotoniske kredsløb med indlejrede enkelt-fotonskilder repræsenterer en lovende platform for kvantecomputere. Mere specifikt tillader suspenderede galliumarsenid (GaAs) membraner med selvsamlede indiumarsenid (InAs) kvantepunkter (KP) udsendelsen af stærkt ensartede og rene enkeltfotoner direkte ind i bølgeledere med koblingseffektivitet tæt på 1. Implementeringen af et kvantefotonisk kredsløb kræver pålidelige rekonfigurerbare elementer såsom bølgesplittere og faseskiftere med lave tab. Termo- og elektrooptiske routere, som er veludviklede teknikker, lider begge under kritiske mangler for GaAs platformen, der bruger lys i InAs KP udsendelsesintervallet (920-945 nm), og opererer under kryogeniske forhold $T \leq 10\,\mathrm{K}$. Den termooptiske koefficient går mod nul ved lave temperaturer, hvorimod elektrooptiske routere inducerer et stort tab via Franz-Keldysh effekten grundet nærheden til båndgabet.

Nanooptoelektromekaniske systemer (NOEMS) udgør en strategi for aktiv kontrol af kompakte rekonfigurerbare elementer kompatible med den ønskede platform. Slot bølgeledere, bestående af to smalle bjælker af materiale med højt refraktivt indeks, leder lys igennem et smalt gap af materiale med lavt refraktivt indeks. Den stærkt ulineære gapsafhængighed af det ledte modes effektive refraktive indeks tillader præcis fasekontrol via elektromekanisk aktuering. Denne afhandling præsenterer designet, fabrikationen og karakteriseringen af en slot bølgeleder faseskifter med en kamdrevsaktuator.

Tabet associeret med søjle-til-slot bølgeleder kopleren er omfattende karakteriseret, både teoretisk og eksperimentelt. En bredbånds faseskifter med en slot bølgeleder længde på $10\,\mu\mathrm{m}$ og et totalt fodaftryk på mindre end $(60 \times 20\,\mu\mathrm{m}^2)$ var fabrikeret og karakteriseret, og udviste et halvbølge-spændings-længde produkt på $V_\pi L = 7.7 \cdot 10^{-3}\,\mathrm{V}\cdot\mathrm{cm}$ ved stuetemperaturer, og $V_\pi L = 12 \cdot 10^{-3}\,\mathrm{V}\cdot\mathrm{cm}$ ved kryogeniske temperaturer. Det reducerede faseskifte ved lave temperaturer er sandsynligvis grundet faktorer såsom temperatur-inducerede forandringer til stivheden af guldmembranen, hvilket leder til en mindre forskubbelse af bjælken.

Til sidst præsenterer afhandlingen et kredsløb der bruger en NOEMS faseskifter til at dynamisk modulere udsendelsesegenskaberne af et kvantepunkt ved at ændre den optiske stilængde til et fjernt spejl, hvilket indstiller dets intensitet og livstid via den lokale tilstandstæthed. Denne evne blev bekræftet gennem eksperimenter der afslørede variationer af intensitets og henfaldsraterne der spændte over respektivt $\nu_I = 0.42$–0.83 and $\nu_\tau = 0.08$–0.27 for en serie af kvantepunkter i forskellige laterale positioner. Dette arbejde markerer et signifikant skridt mod skalerbare integrerede kredsløb for lavtemperaturs manipulation af kvanteudsendere.

Preface

This thesis marks the conclusion of three and a half years of research carried out in the Quantum Photonics group at the Niels Bohr Institute. Research is a deeply collaborative effort, and to properly extend the gratitude I feel towards everybody involved, past or present, would be impossible.

First, I would like to sincerely thank my advisor, Leonardo Midolo, for giving me the opportunity to contribute to this fascinating, complex, and at times seemingly impossible project. This thesis marks the end of almost five years of involvement in the Quantum Photonics group, with Leonardo Midolo as my advisor. His infectious passion for investigating the complex phenomena taking place in integrated photonic devices has been a driving force throughout my time in the Quantum Photonics group, and excitement for pushing the boundaries of what is possible in this field has inspired me to approach challenges with curiosity and determination.

Some people deserve special recognition, as my thesis would never have suceeded without their aid. I would like to extend my deepest gratitude to Ying Wang and Marcus Albrechtsen, for their invaluable aid during the last stretch of my research. I would also like to thank Rodrigo Thomas for, with endless patience, teaching me the ins and outs of experimental characterization of NOEMS devices. I would like to thank Zhe Liu for his aid in the clean room, both for fabricating some of my samples, and for patiently guiding me during my own fabrication processes. I would also like to thank my summer intern, Jasper, who carried out several supremely boring tasks so that I did not have to, including the manual classification of several hundred measurements affected by a data storage bug. I would also like to thank all of the people who have assisted with advice, proofreading, and feedback during the writing process, those being Marcus, Ying, Eric, Patrik, Hania, Nikos, Leonardo, and Rodrigo.

I would like to thank the whole Quantum Photonics group, past and present, and in extension the HyQ-center and the Quantum Optics section, for creating a warm and welcoming work environment. Special shout out to the following: Evi, for all the weird and fun places we've tried out together, Ying, with whom I have shared many meals after a late night of work, Patrik, who taught me how to do my first pull-up, Eric, who during my thesis writing process was always ready to distract me with a chat or a card game, Carlos, with whom I've been writing both my master and my PhD in parallel with, and who's always been ready to lend a listening ear, Hania, who I've battled the cleanroom with, and Nikos, who spreads endless positivity everywhere he goes.

I would also like to thank each and every one of my office mates from a series of rotating offices. Thank you, Mikkel, Sofie, Hans, Yu, Vasso, Evi, Hania, Kasper, and

Johan, for creating a friendly and relaxed working space.

I would furthermore like to thank Carsten Schuck and Marco Butz of the University of Münster, for welcoming me to carry out my external stay in their group. While the work I participated in there did not make it to the final cut of my thesis, primarily due to time constraints, I highly appreciate the knowledge of and the insight into the fascinating field of inverse design of photonics that I gained during my stay there.

To my boyfriend Emil, thank you for always being by my side. You are my grounding rock and my stability in tough times. When shared with you, good times become better, and bad times become less bad. My life would be a lot dimmer without you. To my parents, Mie and Troels, thank you for your endless support throughout my entire life, for always believing in my abilities, and for encouraging me to follow my dreams. Last but not least, I would like to extend my gratitude to my cats Bulbasaur and Spaghetti, two fellow physicists whose curiosity, ingenuity, and persistence in carrying out their important research within the fields of free-falling objects and doorknob mechanics never fail to amuse me.

Publication List

Journal Articles

[1] Rodrigo A. Thomas, Celeste Qvotrup, Zhe Liu, and Leonardo Midolo. "Noise Performance of On-Chip Nano-Mechanical Switches for Quantum Photonics Applications". *Advanced Quantum Technologies* n/a.n/a (2024), p. 2400012.

[2] Celeste Qvotrup, Zhe Liu, Camille Papon, Andreas D. Wieck, Arne Ludwig, and Leonardo Midolo. "Curved GaAs cantilever waveguides for the vertical coupling to photonic integrated circuits". *Opt. Express* 32.3 (Jan. 2024), pp. 3723–3734.

Conference Proceedings

[5] Celeste Qvotrup, Rodrigo Thomas, Zhe Liu, Marcus Albrechtsen, Arne Ludwig, Andreas D. Wieck, and Leonardo Midolo. "Nanomechanical Phase Shifting on a Gallium Arsenide Platform". *The 25th European Conference on Integrated Optics*. June 2024.

Book Chapters

[6] Leonardo Midolo and Celeste Qvotrup. *Nano-Opto-Electro-Mechanical Systems for Integrated Quantum Photonics*. John Wiley and Sons, Ltd, 2023. Chap. 21, pp. 581–597. ISBN: 9783527837427.

Journal Articles in Preperation

[3] Celeste Qvotrup, Ying Wang, Marcus Albrechtsen, Rodrigo A. Thomas, Zhe Liu, Sven Scholz, Arne Ludwig, and Leonardo Midolo. "Controlling emitter-field coupling in waveguides with nanomechanical phase shifters". *In preparation* ().

[4] Celeste Qvotrup, Ying Wang, Marcus Albrechtsen, Rodrigo A. Thomas, Zhe Liu, Sven Scholz, Arne Ludwig, and Leonardo Midolo. "A nanomechanical phaseshifter on a suspended gallium arsenide platform towards integrated quantum photonics". *In preparation* ().

Contents

Journal Articles 7
Conference Proceedings 7
Book Chapters 7
Journal Articles in Preperation 7

Contents **8**

1 Introduction **11**

2 Integrated Quantum Photonics on a GaAs platform **17**
2.1 Photonics 17
2.1.1 Material platforms for integrated photonics 18
2.1.2 Optical elements in integrated photonics 20
2.2 Quantum computing 23
2.3 Optical quantum computing 23
2.3.1 Dual rail encoding 24
2.3.2 Single-photon sources 25
2.4 Quantum dots as single photon emitters 29
2.4.1 Excitation and emission 30
2.4.2 Decay dynamics and selection rules 31
2.4.3 Coupling 31
2.4.4 Emission and collection 32
2.5 Summary and connection 32

3 Control in Integrated Photonics **35**
3.1 Programmability and unitary gates 35
3.1.1 Beam splitters and phase shifters 35
3.1.2 Mach-Zender-Interferometers containing lossy phase shifters . 39
3.1.3 Unitary gates 39
3.2 Modulation strategies 40
3.2.1 Thermo-optic modulation 40
3.2.2 Electro-optic modulation 41
3.2.3 Phase change materials 42
3.2.4 Mechanical actuation - NOEMS 43
3.2.5 Summary and comparison 44
3.3 Active components in integrated quantum photonics 45
3.3.1 Integrated waveguides 45

3.3.2 Directional coupler beam splitters . . . 48
3.3.3 Slot waveguide phase shifters . . . 52
3.4 Summary and connection . . . 54

4 Design of a Slot Mode Phaseshifter 55
4.1 Introduction . . . 55
4.2 The slot waveguide device . . . 55
4.2.1 Optical displacement simulations . . . 56
4.2.2 Actuation mechanism . . . 61
4.2.3 Electromechanical simulations . . . 62
4.3 Conclusion and outlook . . . 64

5 Nanofabrication of integrated Photonics on a GaAs platform 65
5.1 Nanofabrication . . . 65
5.1.1 The GaAs platform . . . 66
5.1.2 Fabrication procedure . . . 66
5.1.3 Lithography . . . 67
5.1.4 Metal deposition . . . 69
5.1.5 Etching . . . 71
5.1.6 Wet etching . . . 73
5.1.7 Fabrication limitations and design considerations . . . 74
5.2 Fabrication results . . . 76
5.2.1 Device uniformity and reproducibility . . . 76
5.3 Conclusion and outlook . . . 76

6 Engineering of Strain in Thin Films 79
6.1 Solid mechanics . . . 79
6.1.1 Strain-induced bandgap change . . . 81
6.2 Bilayer strain . . . 83
6.2.1 Thermal expansion simulations . . . 83
6.2.2 Bent waveguide couplers . . . 87
6.3 Connection and outlook . . . 94

7 A Suspended Platform Slot Mode Phaseshifter 95
7.1 Introduction . . . 95
7.2 Chip layout . . . 95
7.3 Experimental setup . . . 95
7.4 Loss of the slot waveguide coupler . . . 97
7.4.1 Theory and simulations . . . 98
7.5 Phaseshift characterization . . . 104
7.5.1 Phase Shift at 293K . . . 105
7.5.2 Phase shift at 10K . . . 110
7.5.3 Comparison to state of the art . . . 113
7.6 Connection and outlook . . . 114

8 Control of QD emission with a Distant Mirror 115

8.1 Spontaneous emitters and local density of states 115
8.1.1 Intensity modulation of a quantum dot in a 1D system 116
8.1.2 Lifetime modulation of a quantum dot in a 1D system 118
8.2 Experiment 121
8.2.1 Conclusion of experiments 124
8.3 Outlook 125

9 Conclusion and Outlook **127**

Bibliography **129**

A Comparison of BCW Devices **143**

B Derivation of the Lifetime of an Emitter near a Mirror **145**

Chapter 1

Introduction

At the end of the 19th century, many scientists considered physics to be a largely solved topic. A famous quote, misattributed to Lord Kelvin, goes, "There is nothing new to be discovered in physics now. All that remains is more and more precise measurement." While there is no evidence Lord Kelvin ever uttered those words [1], the sentiment mirrors attitudes present in several great theoretical and experimental physicists. Albert A. Michelson, of the famous Michelson-Morley experiment seeking to measure the relative motion of Earth compared to that of the luminiferous aether, uttered in 1894, and repeated in the 1896 Annual Register of the University of Chicago [2] the following:

> *' ... it seems probable that most of the grand underlying principles [of physics] have been firmly established ... An eminent physicist remarked that the future truths of physical science are to be looked for in the sixth place of decimals.'*
>
> (Prof. Albert A. Michelson, 1894)

In a 1924 essay, Max Planck reflected upon how his esteemed professor, Prof Phillip von Jolly, back in 1878 recommended against him going into theoretical physics [3].

> *'[von Jolly] described physics to me as a highly developed, nearly fully matured science, that ... will arguably soon take its final stable form. ... the system as a whole is secured, and theoretical physics is noticeably approaching its completion to the same degree as geometry did centuries ago.'*
>
> (Max Planck, 1924)

However, already back then the limitations of classical physics had begun to make themselves clear. Mysterious incongruities between theory and experiment were showing up at the boundaries of understood phenomena. These include, among others, the ultra-violet catastrophe where the classical Rayleigh-Jeans law predicted that an ideal black body would emit an infinite amount of high-frequency electromagnetic radiation and the total failure to detect the luminiferous aether thought to propagate light. While the latter would eventually be solved in the form of special relativity, the former issue was solved by Planck in 1900, who posited that light was emitted and absorbed in quanta having an energy proportional to the wavelength [4].

Planck saw the concept of quanta as merely a phenomenological construct needed to mathematically explain the behavior of light. However, Planck's theory became the first of many to deal with the topic of fundamental quanta. Albert Einstein's theory of the photoelectric effect from 1905 [5] and Niels Bohr's atomic model from 1913 [6] both relied on the notion of quantized packets of energy to explain hitherto unsolved phenomena.

In 1924, Louis de Broglie introduced the concept of wave-particle duality [7]. The conceptualization of electrons and other fundamental building blocks of physics as being simultaneously waves and matter laid the groundwork for modern quantum mechanics, with both Heisenberg [8] and Schrödinger [9] publishing their compatible theories of matrix mechanics and wave mechanics in the following years. This theory of quantum mechanics has revolutionized the understanding of the behavior of solid matter, processes on (sub)atomic scale, and the behavior of light. This so-called first quantum revolution, which took place in the early and middle 20th century, led to revolutionary technologies such as the laser, the transistor, and the atomic clock. The transistor, which was invented at the Bell Laboratories in the late 1940s [10], enabled the packing of many elements in a small space, making computers smaller and smaller while steadily increasing computing power. This first quantum revolution relied primarily on the increasing understanding of the behavior of materials, making it possible to produce semiconductors, crystals, and atomic clocks with the desired properties.

Now, in the first half of the 21st century, a second quantum revolution is ramping up. This time, advances in nanofabrication have enabled the design and fabrication of devices capable of manipulating the quantum states of their elements. The highly complex behavior of entangled states in superposition theoretically enables computations beyond the capabilities of machines with classical bits. Richard Feynman's 1981 lecture "Simulating Physics with Computers" is considered one of the starting points for the rush towards building a quantum computer [11]. The lecture, dealing with the concept of computability, posits that as the world is quantum mechanical in nature, carrying simulations of quantum mechanical systems using classical computers is, in principle, intractable. While the probabilities of a wavefunction to yield a given result after collapse can be simulated, the sheer complexity of quantum mechanical systems causes the dimensions of the simulation to scale exponentially with the number of degrees of freedom in the system. Compared to a classical system, where n two-level systems can be completely described with n bits, a similar quantum system requires $2^n - 1$ complex numbers [12]. Feynman posited that instead of attempting to simulate quantum systems classically, new insight about the behavior of quantum mechanical systems could be obtained by instead building models of quantum states corresponding to those of the desired systems, and measuring how these evolve under a given input. This approach, called quantum simulation, is considered one of the main applications of a quantum computer.

DiVincenzo's seven criteria for quantum information processing, of which only the first five are necessary for quantum computing, provide an overview of the requirements for a successful quantum computing system [13]. These are A: a scalable physical system with well-characterized qubits, B: the ability to initialize the qubits in a well-defined state, C: long decoherence times of the utilized qubits, D: a set of

universal quantum gates, and E: the ability to measure the state of qubits.

Along a multitude of candidates for qubits, such as majorana fermions [14], trapped ions [15] and superconducting circuits [16], single photons have emerged as a promising qubit platform due to their low decoherence and high-speed travel [17]. Integrated quantum photonics fulfill several of DiVincenzo's criteria, such as the long decoherence times and the well-characterized two-level systems [17]. However, due to the lack of photon-photon interaction, the realization of two-qubit gates between photons is nontrivial. A breakthrough came in 2001, however, when a paper by E. Knill, R. Laflamme and G. J. Milburn presented a scheme that enabled efficient quantum computation only using single photon sources and detectors, and linear gates such as beam splitters and phase shifters [18]. Central to the integrated photonics for quantum computing is the reconfigurable phase shifter. Any lossless experimental setup with N inputs and N outputs can be modeled as an $N \times N$ unitary matrix [19]. Conversely, it has been shown that any $N \times N$ unitary operator can be realized in a circuit consisting exclusively of waveguides, passive 50/50 beam splitters and reconfigurable phase shifters [20].

However, the realization of quantum computing has proved to be an immense technical challenge. Quantum systems are fragile, and prone to errors due to decoherence. Many forms of quantum information processing require temperatures close to absolute zero, either because emergent quantum phenomena such as superconductivity only show up under cryogenic conditions, or to freeze out thermal vibrations that can disrupt qubits and cause their quantum states to decohere into classical states. Fabrication imperfections such as surface roughness can cause a mismatch between modes in couplers and dimensions different from the design files, all of which can induce loss, or cause different effects than what was simulated during the design process.

According to the no-cloning theorem, it is impossible to create a copy of an arbitrary unknown quantum state without destroying the original version of the state [21]. In comparison to classical photonics, where any given signal can be amplified to provide protection against signal losses, a lost or decohered qubit is therefore lost forever. It is therefore imperative to design a quantum information processing platform with as little loss as possible. One big source of loss in photonics and electronics is interconnects. By integrating single-photon sources in a circuit containing waveguides, single-photon gates such as beam splitters and phase shifters, and single-photon detectors, a scalable platform for quantum processing can be realized [22, 23]. Quantum dots (QDs), which are clusters of $\sim 10^5$ atoms, exhibit quantized energy states just like single atoms, and can be embedded in waveguides, where they function as bright and pure sources of indistinguishable single photons [24].

Design of photonic integrated circuits requires a keen understanding of meso-scale material physics. While the ideal circuit is small, robust, efficient, broadband, easily fabricated, and low-loss, many of these features are contradictory, and device parameters must be carefully considered.

Gallium Arsenide, when grown with embedded (InAs) QDs acting as high-quality single photon emitters, is a promising platform for quantum information processing [25]. However, little research has been carried out on the implementation of phase shifters in an integrated GaAs platform. While electro-optic modulation is infeasible

due to the large Franz-Keldysh absorption at the desired wavelengths [26], efficient nanomechanical beam splitters have been presented on suspended GaAs membranes [27]. Using similar design principles as the beam splitters, nanomechanical phase shifters using perturbing cantilevers [28, 29, 30] or slot waveguides [31, 32] have been presented on a variety of integrated photonic platforms. However, to the best of the author's knowledge, the current literature does not cover experimental implementations of nanomechanical phase shifters on a GaAs platform. This thesis covers the design, fabrication, and characterization of a nanomechanically actuated phase shifter on a (GaAs) platform, as well as the application of a phase shifter to control quantum dot emission properties by shifting the effective path length between the quantum dot and a mirror.

In chapter 2, the theoretical background of integrated photonics for quantum computing is introduced. An introduction to the fundamentals of quantum information is given, and different platforms for integrated quantum photonics are presented.

While passive circuits, where the behavior of all devices and components are set at fabrication, can function for some purposes, integrated quantum photonics generally requires reconfigurable devices. In chapter 3, the theory of controllable integrated photonics is presented. Integral components such as beam splitters and phase shifters are presented, and approaches for controllable integrated photonics are laid out. The different approaches are compared, and their advantages and disadvantages, both generally and for the gallium arsenide platform utilized in this thesis, are laid out.

Utilizing the principles laid out in the previous chapter, chapter 4 presents a phase shifter in the form of a nano-opto-electro-mechanical system (NOEMS) slot waveguide. Preliminary simulations characterizing the phase shift and electromechanical deformation are carried out and used to guide the design of the phase shifter.

In chapter 5, the field of micro- and nanofabrication is introduced, with special focus on the design and fabrication of devices on suspended gallium arsenide, the platform utilized in this thesis. Common fabrication issues are addressed, and the special measures necessary when fabricating delicate nano-scale devices are laid out.

In chapter 6 an introduction to nano-scale materials physics is made, and the fabrication of three-dimensional couplers obtaining a vertical orientation by utilizing the intrinsic stress mismatch between the two layers of a bilayer cantilever is presented.

In chapter 7, a thorough theoretical and experimental analysis of the loss of the slab-to-slot waveguide coupler is carried out. Following, the phase shifter is characterized at room temperature (T = 293 K) and cryogenic temperatures (T = 10 K) by investigating the wavelength- and voltage-dependence of the interference fringes of a Mach-Zender-Interferometer with a phase shifter in one arm.

Finally, in chapter 8 the use of a phase shifter to change the effective path length

between an emitter and a mirror is investigated, and the change to quantum dot lifetime and intensity of emitted light is characterized.

Chapter 2

Integrated Quantum Photonics on a GaAs platform

In this chapter, an introduction is given to the fields of photonics, quantum computing and semiconductor physics, with the purpose of building a theoretical understanding of the quantum photonics platform of choice, namely integrated suspended gallium arsenide (GaAs) with embedded indium arsenide (InAs) quantum dots functioning as single photon emitters. The field of integrated photonics is introduced. Important material platforms for integrated quantum photonics are presented, and their advantages and disadvantages are discussed. Gallium arsenide, the material of choice, is presented, and its material properties are explored. Common active and passive components are introduced, with special consideration on the components utilized in this thesis, such as waveguides, chip-to-fiber couplers and directional couplers. The topic of optical quantum computing is introduced, and the encoding of single photons is discussed. The quantum mechanical properties of indistinguishable single photons are presented, and important benchmark experiments showcasing these are discussed. Different strategies for the generation of indistinguishable single photons are discussed, and the deterministic generation of indistinguishable single photons using quantum dots is presented. Finally, the relevant semiconductor physics of InAs quantum dots embedded in a GaAs platform is presented.

2.1 Photonics

Photonics is a branch of optics, the science of light, which concerns itself with the application of photons for technological purposes [33]. Photonic devices generate, detect, route, and manipulate photons by utilizing techniques such as emission, amplification, and modulation. Examples of photonic technologies are fiber-optic cables used for high-speed telecommunications, photovoltaic cells that can convert sunlight into electricity, and lasers, which can emit highly coherent light of a single wavelength by exploiting stimulated emission.

Similarly to the field of electronics, a large fraction of research activity into photonics has been focusing on miniaturization, or the packing of a larger number of photonic components in a tighter space. While individual free-space optical components

can be made smaller, and packed tighter, there is a lower limit to the distance between optical elements. Furthermore, tight packing of separate elements complicates aligning. By integrating photonic waveguides and optical components on a chip, the seamless placement of large numbers of components in a tight space can be realized. Furthermore, as the optical path in integrated circuits is defined by the waveguides, the elements of an integrated circuit do not require individual alignment. By additionally integrating photon sources and detectors on chip, losses from interconnects and chip-to-fiber couplers can be minimized [34].

2.1.1 Material platforms for integrated photonics

The development of a material platform that is compatible with embedded high-quality single photon emitters and can facilitate low-loss guiding through waveguides, as well as active control of light at cryogenic temperatures has proven itself a tremendous technological challenge. This is in part because a given material property might induce both desirable and undesirable behavior in an integrated photonic circuit. Developing a platform for integrated quantum photonics thus involves carefully considering the specific requirements of the final product, while taking precautions to cancel out disadvantages of the platform [35]. Properties to keep in mind when choosing a platform for integrated quantum photonics include low propagation loss, large refractive index contrast, toxicity, ease of fabrication, ability to integrate high-quality single photon sources, compatibility with existing technologies, and the presence of desirable material properties such as a lack of inversion symmetry which enables an abundance of material responses and properties.

Silica and silicon photonics

Silicon-based platforms are well-developed, mature, and extensively used platforms for integrated photonics [36]. Silica (SiO_2) is a dominant material in fiber optics due to its abundance, its wide transparency ($0.2 - 3\,\mu m$) as well as its record low loss, which can be as low as 0.2 dB/km at 1550 nm, the wavelength most commonly used for telecommunications [37]. Its low refractive index ($n = 1.44$), however, makes it unsuitable for use as waveguides in integrated photonics, as the small index contrast requires very large bending radii to prevent losses. However, silica is still sometimes used as a platform for integrated quantum photonics, as the large mode size minimizes the impact of surface roughness and enables easy chip-to-fiber coupling [38].

Silicon-on-Insulator (SoI), where silicon ($n_{Si} = 3.45$) is grown on top of an insulator such as SiO_2, was originally chosen for integrated electronics, but was adapted for optical waveguides in the 1990s. The high index contrast between silicon and SiO_2 allows for the fabrication of small features with tight bends [39]. However, as silicon is a centrosymmetric material, it lacks a second-order optical nonlinear susceptibility, which is required for important electro-optic properties such as the Pockels effect and second-harmonic generation. While nonlinear effects can be induced via breaking the crystalline symmetry with an inhomogeneous applied strain [40] or a strong electric field causing the dipole moments to orient themselves in the field direction [41], this

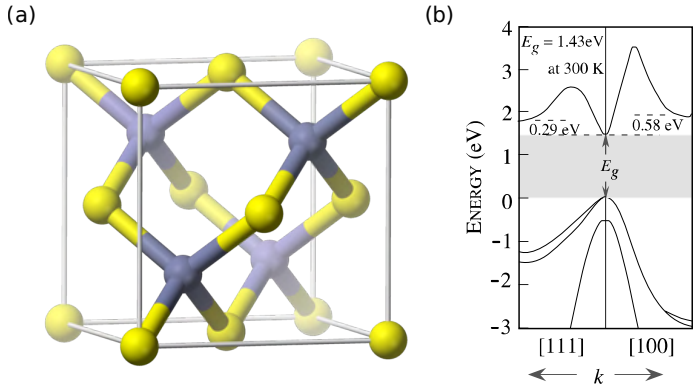

Figure 2.1: (a): Structure of zincblende crystal. Source: Wikipedia [45] (released into public domain by creator). (b): GaAs band structure close to the zone center. Adapted from [46]

adds additional complexity in the fabrication process and the experimental protocol, and it is therefore desirable to explore platforms capable of active electric control. Furthermore, the indirect bandgap of Si complicates the integration of single photon emitters [42].

Lithium niobate

Lithium Niobate on Insulator (LNOI) is an emerging platform for integrated quantum photonics [43]. Favorable properties of LNOI include a large transparency window ($0.4-5\,\mu$m) [39], a large electro-optic coefficient $r_{33} = 30\,\text{pm/V}$, which in combination with the large, indirect bandgap ($E_g = 3.77\,\text{eV}$) facilitates electro-optic modulation at near-infrared wavelengths. A strong second-order nonlinear coefficient $d_{33} = 27\,\text{pm/V}$ furthermore makes lithium niobate a promising platform for nonlinear optical technologies such as second harmonic generation and frequency conversion, as well as spontaneous parametric down-conversion (SPDC) [44].

III—V photonics

III—V semiconductors refer to compounds consisting of materials in group III of the periodic table, such as aluminum (Al), gallium (Ga) and indium (In), combined with group V materials such as arsenic (As), nitrogen (N), antimony (Sb) and phosphorus (P) [47]. Important III—V semiconductors in photonics include gallium arsenide (GaAs), indium arsenide (InAs), indium phosphide (InP), as well as the ternary alloy aluminum gallium arsenide ($\text{Al}_x\text{Ga}_{1-x}\text{As}$), where the x refer to the fraction of the group III atoms being aluminum. These materials typically take the form of zincblende crystals, where each of the materials is ordered in a face centered cubic crystal structure, with the two materials having their origin at respectively $[0,0,0]$ and $[1/4,1/4,1/4]$, as seen in Fig. 2.1. This structure is not centrosymmetric, meaning important material properties such as piezoelectricity, the Pockels effect and second order nonlinear coefficient are present. Many III—V semiconductors such as GaAs, InP and InAs additionally have direct bandgaps [46], making them desirable platforms

for realizing integrated quantum photonics. Additionally, the large refractive indices ($n_{\mathrm{GaAs}} \sim 3.45$ at 930 nm) of some III—V materials enable tight confinement of light in narrow waveguides with sharp bends. III-V materials can be grown epitaxially on top of each other enabling fabrication of heterostructures [48]. The direct bandgap of III—V semiconductors enables the growth of heterostructure quantum dots where light is strongly confined in all three directions [25]. These quantum dots function as highly efficient single photon emitters, allowing the integration of III—V platforms with highly efficient deterministic single photon devices. For this reason, the platform for this thesis was chosen to be GaAs membranes with InAs quantum dots.

In addition to the mentioned materials, there is a plethora of other platforms, all with unique advantages and disadvantages. Furthermore, research into heterogeneous integration technologies such as die-to-wafer bonding [49] and pick-and-place [50] promises the opportunity to combine several material platforms, such as by combining efficient single-photon emitters with otherwise incompatible platforms. These techniques, while promising, are still in their infancies and more research is needed to improve losses.

2.1.2 Optical elements in integrated photonics

Integrated photonics is a well-developed field, and a rich variety of both active and passive components exists. This section will provide a short overview of the important building blocks in integrated photonics, several of which will be expanded upon in chapter 3, which covers the control of light in an integrated photonic circuit.

Passive components form the foundation of all integrated photonics technologies. They route, couple, and interfere the light propagating through the circuit, forming the basis with which active, controllable elements can be integrated. Examples of passive components utilized in this thesis are waveguides, which propagate light across the integrated photonics circuit, the couplers, which couple light in and out of the circuit, directional couplers, and mirrors. Other commonly used passive components include disc and ring resonators, which can act as notch or add-drop filters with wavelength intervals equal to the free spectral range (FSR) of the ring, polarization rotators, and waveguide crossings [51].

Active components allow for the creation, control, and detection of light in integrated photonic circuits. Passive components, such as directional couplers, can be made active by adding the option to control the splitting ratio. The main objective of this thesis is to build a tunable phase shifter, which is an example of an active device. Single-photon sources in the form of quantum dots are also active components utilized in this device. Other common active devices are lasers, modulators, amplifiers, and detectors.

Waveguides

Integrated photonics is often considered an optical analogy to integrated electronics. However, the significant differences between the two technologies become apparent

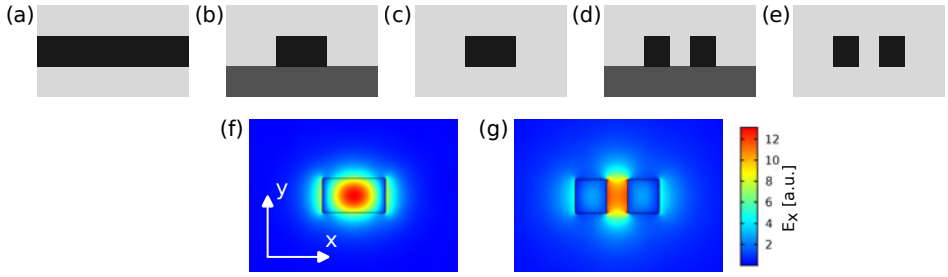

Figure 2.2: Different types of waveguides. Darker color corresponds to higher material index of refraction. Features reaching the edge of the illustration are assumed to be infinite in width. a: Infinite slab waveguide. b: Strip waveguide. c: Buried or suspended strip waveguide. d: Slot waveguide. e: Buried or suspended slot waveguide. f: Electric field distribution of the fundamental TE mode for a buried or suspended strip waveguide. g: Electric field distribution of the fundamental TE mode for a buried or suspended slot waveguide.

when considering the most fundamental element of integrated photonics, namely the waveguide. The electronic band structure of a given material will either allow or forbid conduction of free electrons for respectively conductors and insulators. The integrated electronics analogy to a waveguide, the wire, can thus be created simply by surrounding a strip of conductive material with an insulating material.

A chief challenge in integrated photonics is engineering environments capable of confining and guiding light. An essential element in the photonic integrated circuit is the waveguide, which often, but not always, consists of a core of higher index material surrounded by lower index material. Taking advantage of the property of total internal reflection, light can be fully confined in the higher index material, forcing it to propagate along the waveguide [52].

In Fig. 2.2, an overview of different types of waveguides can be seen. Fig. 2.2(a) shows an infinite slab waveguide. The modes of these waveguides can be derived analytically, and as a result, they serve as the starting points for the analytical calculation of the effective refractive indices in a waveguide. Figs. 2.2(b) and (c) show strip waveguides, which are higher index beams surrounded by lower index materials. Strip waveguides are often fabricated from high-index material grown or deposited on top of a lower-index substrate. Capping the waveguide with a different material can protect the surface of the material from unwanted oxidation and reduce the losses due to surface scattering [53]. However, the index contrast between the substrate and the cladding leads to an asymmetry in the mode, which is undesirable if the design requires the maximum intensity of the electric field to be in the middle of the waveguide. By making the cladding and the substrate the same material, in what is known as a buried waveguide, as shown in Fig. 2.2(c), this can be avoided. Mathematically similar to the buried waveguide is the suspended waveguide, which consists of free-floating cantilevers supported by tethers where the underlying substrate has been removed, for example, by utilizing a wet etch. Although suspended waveguides are fragile, prone to collapse, and can suffer from undesired effects from interacting with the environment, they are the backbone of photonic nano-electro-mechanical systems

(NEMS), where changes to the optical properties of the system are induced by electromechanical displacement of the cantilevers. Furthermore, suspended waveguides have great confinement due to the large effective index contrast.

In comparison to strip waveguides, slot waveguides, shown in Figs. 2.2(d) and (e), consist of two narrow, high-index cantilevers placed close together. In a slot waveguide, the bulk of the electric field distribution is confined within the gap between the cantilevers [54]. The effective refractive index of the slot waveguide mode is highly gap-dependent, making suspended slot waveguides promising candidates for nanomechanically actuated phase shifters [31]. A comparison of the transverse electric field distribution for the fundamental TE mode for respectively a buried/suspended strip waveguide and a buried/suspended slot waveguide is shown in Figs. 2.2(f) and (g).

The photonics analogy of the electronic insulator is photonic crystals, which are nanomaterials with periodic variations of their refractive index. By engineering the periodicity of a photonic crystal, photonic bandgaps with forbidden wavelengths can be designed, making it impossible for light of those wavelengths to propagate through the crystal. This technology can be used for photonic crystal mirrors, for engineering the surroundings of a waveguide containing single-photon emitters to ensure optimal emission efficiency into the guided mode, and for creating photonic crystal cavities [25].

Couplers

Typical wavelengths in the integrated photonics platform used for this thesis are in the order of $900-970\,\text{nm}$, with waveguides having typical widths in the order of $200-300\,\text{nm}$. Core diameters of fibers for this wavelength are, however, typically much larger. For instance, the waveguides utilized in this thesis have a cross-section area of $0.160\,\mu\text{m} \times 0.300\,\mu\text{m} = 0.048\,\mu\text{m}^2$. A typical fiber used for the measurements in this thesis is Thorlabs 780HP [55], which has a core diameter of $4.4\,\mu\text{m}$, equivalent to an area of $15.2\,\mu\text{m}^2$, giving a Gaussian mode size $\approx 10\,\mu\text{m}^2$. Modes from free-space lasers can be even larger. While the mode sizes can be decreased using focusing lasers, the area will still be of the order of $1\,\mu\text{m}^2$. These dimensional differences necessitate efficient chip-to-fiber coupling strategies. These typically fall into one of two categories [56]. Edge coupling using inverted tapers allows for high efficiency and polarization-independent coupling, but requires horizontal access and limits device placement to the edges of the chip. Out-of-plane couplers typically consist of sets of gratings, which scatter the light into the desired waveguide mode. These have flexible placement, allowing for a higher density of devices, but have limited bandwidth and are polarization-dependent.

Beam splitters and phase shifters

Beam splitters and phase shifters are essential optical elements, which form the backbone of integrated photonic information processing, such as quantum computing [18]. Compared to free-space beam splitters, which typically are semi-transparent mirrors, integrated beam splitters are typically sets of narrow waveguides placed close to each other. This design is also known as a directional coupler. The narrower the waveguide,

the larger the proportion of the light being located in the exponential tail outside the waveguide rather than confined inside the waveguide itself. If a second waveguide is placed beside the first waveguide, so close that the exponential tail overlaps with the second waveguide, the light will begin to couple between the two waveguides, oscillating between them with a beat length dependent on the coupling strength between the waveguides. This allows the set of waveguides to act as a beam splitter with a splitting ratio dependent on the length and the separation between the waveguides. The coupling strength will increase with decreased separation distance, enabling the use of beam splitters with controllable separation distances to actively route light in a circuit [27].

Integrated phase shifters are typically realized by changing the effective refractive index of the guided mode in a section of the waveguide [57]. As the accumulated phase in a section of the waveguide is the integral over the effective refractive index,

$$\phi_x = \frac{2pi}{\lambda_0} \int_0^L n(x)\,\mathrm{dx}, \tag{2.1}$$

changing the effective refractive index of a waveguide mode over a section of a waveguide will modulate the accumulated phase. The derivation of the behavior of integrated beam splitters and slot waveguide phase shifters will be carried out in chapter 3.

2.2 Quantum computing

Classical computation involves the use of binary bits, which can be either in the 0 or 1 state, often encoded as "off" and "on" states. While the development of the computer has greatly improved the computational power available to researchers, enabling calculations and simulations, which would have been infeasible to carry out by hand, the binary, classical nature of standard computers has proven inadequate when dealing with the rapid complexity scaling of problems involving superpositions of entangled quantum particles [11]. The potential use of quantum bits, which can be in any superposition of two states $|0\rangle$ and $|1\rangle$, has been proposed to be used in quantum computers. While this thesis covers the use of single photons as qubits, many quantum computing platforms have been proposed. Examples of alternatives to photonic quantum computing are trapped ions [58] and superconducting qubits [16].

2.3 Optical quantum computing

Optical quantum computing uses the single photon as a quantum particle. Photons have the advantage of being relatively easy to generate compared to other qubit platforms, as well as being compatible with the well-developed fields of free-space optics and integrated photonics. Another key advantage of photons as qubits is their high coherence [17]. A large disadvantage to the use of photons as qubits is their high loss rate [59], as well as the difficulties in storing photons. Due to this, the interfacing of quantum photonics with other quantum systems acting as memories is required for large-scale quantum systems [60].

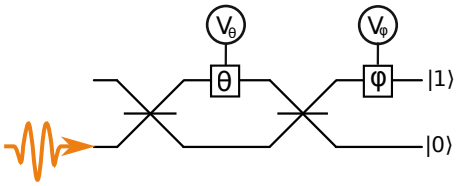

Figure 2.3: Unitary gate enabling preparation of arbitrary quantum state in the dual rail encoding using path modes. The crosses represent beam splitters, which under ideal conditions are lossless, balanced and symmetric, with boxes ϕ and θ representing phase shifters programmable using respectively voltages V_ϕ and V_θ.

2.3.1 Dual rail encoding

An arbitrary two-level quantum state, where global phase is disregarded, can be mathematically described as the following,

$$|\phi\rangle = \alpha_0 |0\rangle + e^{i\phi} \alpha_1 |1\rangle , \tag{2.2}$$

with $|\alpha_0|^2 + |\alpha_1|^2 = 1$. This encodes a quantum state that upon measurement has $|\alpha_0|^2$ chance of being in state $|0\rangle$, and $|\alpha_1|^2$ of being measured in state $|1\rangle$, and the $|1\rangle$ state has $e^{i\phi}$ phase relative to the $|0\rangle$ state. The chosen state depends highly on the physical phenomena used to create the qubit. In the single rail encoding of a single photon qubit, the absence of a photon is used as state $|0\rangle$, while the presence of a photon is used as state $|1\rangle$ [61]. In this encoding, it is impossible to distinguish between the loss of a photon in the $|1\rangle$ state and a photon in the $|0\rangle$ state, which will lead to a large dephasing. A widely used technique is instead the dual rail encoding, in which the $|0\rangle$ and $|1\rangle$ states are encoded as two orthogonal states. This encoding can be carried out in several different ways. Free-space optics often encode the information in the polarization of the photons [62], while optical fibers often use time-bin encoding [63]. An encoding commonly utilized in integrated photonics, and which will be investigated in this thesis, is path encoding, where the two respective states correspond to two different spatial locations [64]. Here, the photon can travel along two physical paths, with one path corresponding to $|0\rangle$ and the other path corresponding to $|1\rangle$ [65], as can be seen in Fig. 2.3.

As photons do not interact with each other outside of highly engineered nonlinear environments, creating deterministic two-photon gates in the path encoding is very challenging and involves exploiting light-matter interactions. However, universal quantum computing can still be carried out by using linear, probabilistic optical elements [18]. By utilizing either variable beam splitters or static beam splitters combined with programmable phase shifters in Mach-Zender Interferometers (MZI), the qubit can be switched between the two states. Variable phase shifters outside MZIs can be used to control the relative phase between the two states. Fig. 2.3 shows a unitary gate in the path encoding. The phase shifter with label θ switches between the $|0\rangle$ and $|1\rangle$ states, while the phase shifter with label ϕ controls the relative phase between the states.

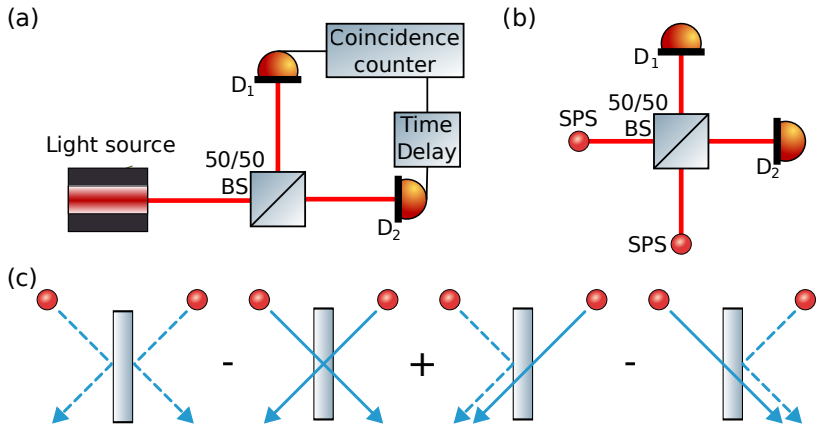

Figure 2.4: (a): Hanbury-Brown-Twiss experiment. (b): Hong-Ou-Mandel (HOM) experiment. (c): Visualisation of the probability amplitudes in the HOM experiment

2.3.2 Single-photon sources

Optical quantum computing requires efficient single-photon sources. Important figures of merit for a single-photon source are the following [24]:

- Purity — the source emitting one and only one photon at a time.
- Brightness — the repetition rate of the source.
- Indistinguishability — how identical the photons are. This includes wavelength and polarization.
- Deterministic-ness — whether the the single photon source can produce a photon on demand.

Purity

The purity of a single photon source refers to the degree to which the source achieves to emit single photons only, with no multi-photon events. Most protocols for linear optical quantum computing assume the presence of single photons only [18], and as such multi-photon events will lead to incorrect preparation of quantum states, causing computational errors.

The purity of the photons can be measured with the Hanbury-Brown-Twiss experiment, a schematic of which can be seen in Fig. 2.4(a) [66]. This experiment is used to measure the bunching or antibunching tendencies of a photon source. A 50/50 beam splitter divides the incoming light into two beams. Two photon detectors D_1 and D_2 are placed at equal distances from a beam splitter. A variable time delay τ is placed just after D_2. This allows the measurement of a delayed coincidence rate where one detector registers a count at time t and the other at $t+\tau$.

The second order quantum correlation function $g^{(2)}(\tau)$ is [67]

$$g^{(2)}(\tau) = \frac{\left\langle \hat{E}^{(-)}(t)\hat{E}^{(-)}(t+\tau)\hat{E}^{(+)}(t)\hat{E}^{(+)}(t+\tau)\right\rangle}{\langle I(t)\rangle \langle I(t+\tau)\rangle}. \tag{2.3}$$

The second order quantum correlation function describes the tendency of a photon source to fluctuate. The special case $\tau = 0$ is of special importance, as it describes the tendency of photons to bunch together. For $\tau = 0$, three important cases can be distinguished.

$$\begin{cases} g^{(2)}(0) > 1 & \text{Light is bunched} \\ g^{(2)}(0) = 1 & \text{Light is coherent} \\ g^{(2)}(0) < 1 & \text{Light is antibunched} \end{cases} \tag{2.4}$$

$g^{(2)}(0)$ describes the probability of a photon to arrive at detector D_2 if a photon is measured at detector D_1, *relative* to the chance of detecting a photon at D_1. Coherent light, which has $g^{(2)} = 1$ and is said to exhibit Poissonian statistics, shows completely random behavior, without tendencies towards bunching or antibunching. Light with $g^{(2)} < 1$ is equivalent to $P_2 P_1 < P_1^2$, where P_1 is the probability of detecting one photon, and P_2 is the probability of detecting two photons *if at least one photon is detected*. This causes antibunching, or sub-Poissonian, behavior of the photons. For an ideal single-photon source there will never be photons arriving at D_1 and D_2 simultaneously, and as such $g^2(0) = 0$. This makes the $g^{(2)}(0)$-value one of the most important benchmarks for single photon sources [68].

Indistinguishability

Indistinguishable photons are required for operations that create superpositions of multiple photons, and the indistinguishability of the single photons is thus another of the most important benchmark parameters for a single photon source. The indistinguishability of single photons can be measured with the HOM experiment first performed by Hong, Ou, and Mandel, which is illustrated on Fig. 2.4(b-c) [69]. A beam of single photons is split into two paths, and one path is given a controllable time delay ensuring that the two single photons will simultaneously interfere on a 50/50 beam splitter.

For a 50:50 beam splitter, the input modes $\hat{a}_0^\dagger$ and $\hat{a}_1^\dagger$ and output modes $\hat{a}_2^\dagger$ and $\hat{a}_3^\dagger$ are related according to the following beam splitter transformations [67]

$$\hat{a}_0^\dagger = \frac{1}{\sqrt{2}}\left(\hat{a}_2^\dagger + i\hat{a}_3^\dagger\right), \quad \hat{a}_1^\dagger = \frac{1}{\sqrt{2}}\left(i\hat{a}_2^\dagger + \hat{a}_3^\dagger\right). \tag{2.5}$$

Starting with a state containing two identical photons,

$$|Q\rangle = |1\rangle_0 |1\rangle_1 = \hat{a}_0^\dagger \hat{a}_1^\dagger |0\rangle_0 |0\rangle_1, \tag{2.6}$$

applying the beam splitter transformations leads to

$$\begin{aligned} |Q\rangle &= \frac{1}{\sqrt{2}}\left(\hat{a}_2^\dagger + i\hat{a}_3^\dagger\right)\frac{1}{\sqrt{2}}\left(i\hat{a}_2^\dagger + \hat{a}_3^\dagger\right)|0\rangle_0 |0\rangle_1 \\ &= \frac{1}{2}(i\hat{a}_2^\dagger\hat{a}_2^\dagger + i\hat{a}_3^\dagger\hat{a}_3^\dagger + \hat{a}_2^\dagger\hat{a}_3^\dagger - \hat{a}_3^\dagger\hat{a}_2^\dagger)|0\rangle_0 |0\rangle_1 = \frac{1i}{\sqrt{2}}(|2\rangle|0\rangle + |0\rangle|2\rangle), \end{aligned} \tag{2.7}$$

where the results follow from the commutation relation $\left[\hat{a}_2^\dagger, \hat{a}_3^\dagger\right] = \hat{a}_2^\dagger \hat{a}_3^\dagger - \hat{a}_3^\dagger \hat{a}_2^\dagger = 0$ assuming indistinguishable photons. The probability amplitudes of the two photons taking two separate paths are illustrated visually in Fig. 2.4(c). This demonstrates the remarkable property of indistinguishable single photons simultaneously interfering on a beam splitter, namely that the photons will cluster together and will always take the same output path of the beam splitter.

Weak coherent states as single photon sources

Early implementations of single photon sources in quantum cryptography often used weak coherent states (WCS) [70]. A coherent state is a classical-like state consisting of a superposition of Fock states.

$$|\alpha\rangle = \exp\left(-\frac{1}{2}|\alpha|^2\right) \sum_{n=0}^{\infty} \frac{\alpha^n}{\sqrt{n!}} |n\rangle \tag{2.8}$$

Here $|\alpha\rangle$ is an eigenstate of the annihilation operator, $\hat{a}|\alpha\rangle = \alpha|\alpha\rangle$ [67]. Finding the expectation value of the photon number operator, $\hat{n} = \hat{a}^\dagger \hat{a}$,

$$\bar{n} = \langle\alpha|\hat{n}|\alpha\rangle = \langle\alpha|\hat{a}^\dagger \hat{a}|\alpha\rangle = |\alpha|^2, \tag{2.9}$$

makes it clear that the average photon number is $|\alpha|^2$. For a WCS where $|\alpha| \ll 1$, the first few terms of the coherent state are

$$|\alpha\rangle \approx |0\rangle + \alpha|1\rangle + \frac{\alpha^2}{2}|2\rangle \ldots \tag{2.10}$$

This means that the probabilities of each of the states are

$$P_{|0\rangle} \approx 1, P_{|1\rangle} \approx \alpha^2, P_{|2\rangle} \approx \frac{\alpha^4}{4} \ldots \tag{2.11}$$

The rate of single photons to two-photon states,

$$P_{|1\rangle}/P_{|2\rangle} = \frac{\alpha^2}{\alpha^4/4} = \frac{4}{\alpha^2}, \tag{2.12}$$

thus scales with $1/\alpha^2$, leading to a higher rate of photons the higher α is, at the expense of a higher probability of multi-photon events. WCS are easy to create, as they can be realized utilizing a faint pulsed laser. However, given that coherent states always have a $g^{(2)}(0) = 1$, they will obey Poissonian statistics. While the probability of a two-photon state might be low, the development of true single photon sources exhibiting sub-Poissonian photon statistics is a main challenge towards the development of an optical quantum computer.

Spontaneous parametric processes

In the presence of light with an electric field **E**, the polarization response of a dielectric material will be the following

$$\mathbf{P}(\mathbf{E}) = \varepsilon_0 \left(\chi^{(1)} \cdot \mathbf{E} + \chi^{(2)} : \mathbf{EE} + \chi^{(3)} \vdots \mathbf{EEE} + ... \right). \tag{2.13}$$

Here, χ^n is the n'th order coefficient of a Taylor expansion of the material electric susceptibility, which is a tensor of rank $n+1$ [71]. Writing out the tensor multiplication explicitly, the equation can also be written as

$$P_i = \varepsilon_0 \left(\chi^{(1)}_{ij} E_j + \chi^{(2)}_{ijk} E_j E_k + \chi^{(3)}_{ijkl} E_j E_k E_l \right), \tag{2.14}$$

where any repeating indices imply summation over those indices.

While all dielectric materials have a non-zero $\chi^{(1)}$ term, only materials lacking inversion symmetry exhibit a non-zero $\chi^{(2)}$ term. The $\chi^{(3)}$ term is also present in all dielectrics, but of a much smaller magnitude than the preceding terms, and its effects thus require large fields to yield measurable results.

Spontaneous parametric down-conversion (SPDC) is the spontaneous splitting of a photon with frequency ω_1 into two other photons with energies ω_2 and ω_3, while obeying energy conservation $\omega_1 = \omega_2 + \omega_3$ and momentum conservation $\vec{k}_1 = \vec{k}_2 + \vec{k}_3$ [72]. These are called the phase matching conditions and control the conditions under which SPDC is possible. SPDC is a second-order nonlinear phenomenon whose efficiency scales linearly with the second-order nonlinear susceptibility $\chi^{(2)}$ and is thus only present in crystals lacking inversion symmetry. The momentum conservation requires that

$$|\vec{k}_1| = |\vec{k}_2| + |\vec{k}_3| = \frac{n_1 \omega_1}{c} = \frac{n_2 \omega_2}{c} + \frac{n_3 \omega_3}{c}. \tag{2.15}$$

Spontaneous four-wave mixing (SFWM) is a third-order nonlinear effect where two photons with energies ω_1 and ω_2 combine to form two new photons with energies ω_3 and ω_4 while obeying energy conservation, $\omega_1 + \omega_2 = \omega_3 + \omega_4$ and momentum conservation, $\vec{k}_1 + \vec{k}_2 = \vec{k}_3 + \vec{k}_4$. SFWM is proportional to $\chi^{(3)} E^3$, and typically requires very strong electric fields to get a significant photon generation. Both of these methods are probabilistic rather than deterministic. However, as each of the processes produces two photons, they enable heralded single photon emission [73]. Here, the two photons are split utilizing a beam splitter and one photon is led into a detector, alerting about the existence of the other photon.

Two level systems as single photon emitters

Deterministic approaches to creating single photon sources allow on-demand generation of indistinguishable single photons with nearly ideal sub-Poissonian photon statistics [74]. If a two-level system is excited with a pulse taking an electron from its ground state $|g\rangle$ to its excited state $|e\rangle$, it will emit a single photon with a frequency corresponding to the transition energy of the two-level system. The latency between excitation and photon emission is determined by the lifetime of the emitter, which in

the simplest theoretical models undergoes pure exponential decay, and sets the upper limit of the repetition rate of single photons from a single quantum emitter [75]. Examples of structures with two-level systems that have been used to generate single photons are single emitters such as atoms, or composite structures such as quantum dots and color centers.

Single atoms such as Rubidium-85 are nearly ideal isolated quantum systems [76]. As all atoms of a given isotope are identical, this allows for easy production of indistinguishable emitters. However, these atoms need to be trapped in complex magneto-optic traps that guide the captured atoms into free-space optical cavities. Ultimately, this technology is limited by the finite trapping time [77]. Color centers are a type of point defects in diamond where a carbon atom is replaced by another atom, such as a Nitrogen atom (NV type) or Silicon atom (SiV type), leaving a neighboring lattice site vacant [78]. These systems have high electron spin coherence times. However, the quality of single photons emitted by these centers tends to have low purity and indistinguishability, as well as a low yield into the zero-phonon line [79].

Semiconductor quantum dots are clusters of the order of 10^5 atoms that can be grown by utilizing techniques such as molecular beam epitaxy (MBE). Due to their small size, they act as 0-dimensional artificial atoms. Quantum dots are widely studied as single photon emitters, and can act as deterministic single photon sources with high purity and indistinguishability [22, 23, 80]. However, due to random fluctuations during fabrication, individual quantum dots have different energy levels. While the bandgap of a quantum dot can be tuned with electro-optic [81] or strain-tuning [82] methods, this tuning range is far from the distribution of quantum dot emission energies, which for the platform utilized in this thesis fell in the range of $\sim (935 \pm 10)$ nm. This poses a challenge for the scalability of technologies utilizing quantum dots as single photon sources. Semiconductor quantum dots, however, can be embedded directly in integrated photonics circuits, where their surroundings can be engineered to facilitate their emission into waveguide modes.

2.4 Quantum dots as single photon emitters

As mentioned in the previous section, III—V quantum dots can perform as highly pure and indistinguishable single photon emitters. In this work, a platform consisting of GaAs with embedded InAs quantum dots is utilized. The lattice constant of GaAs is 565.315 pm, while the lattice constant of InAs is 605.83 pm. When InAs is grown epitaxially on top of GaAs, the first few monolayers of InAs will adopt the GaAs lattice constant. This 7% offset will lead to a large intrinsic strain in the InAs, which after a few layers will lead to the nucleation of islands [84]. These islands are approximately 15-20 nm wide and 5-10 nm tall. Following MBE of InAs, the quantum dots are topped with another layer of GaAs. This technique of producing self-assembled quantum dots is called Stranski-Krastanov growth [85].

This technique leads to scattered quantum dots with varied energy levels due to the random nature of the self-assembly process. While techniques exist to locate the quantum dots before fabrication and deterministically place devices at desired loca-

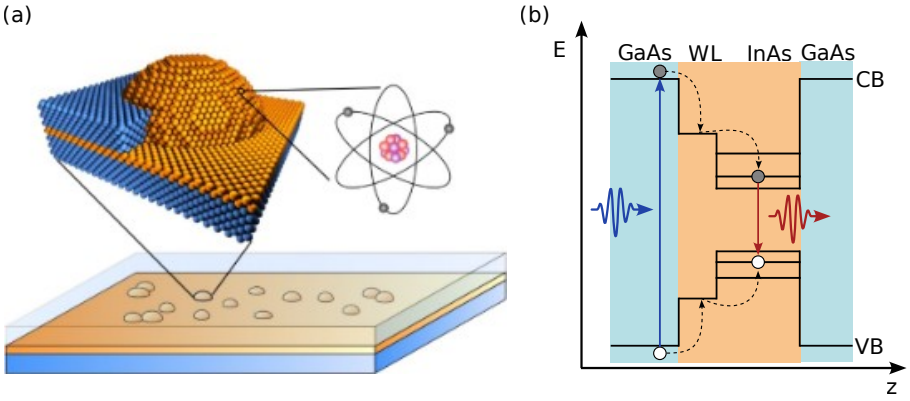

Figure 2.5: a: Illustration showing quantum dots grown using the Stranski-Krastanov method. b: Energy levels in an InAs-in-GaAs quantum dot. Figure adapted from [83]

tions [86], these methods add additional fabrication complexity. If the addition of extra steps is considered undesirable, many devices can be placed instead in the hope that some will have high-quality quantum dots at the desired locations. Furthermore, while a large part of the intrinsic strain in the InAs is relaxed upon the quantum dot nucleation, a strain will still be present in the quantum dots, which can lead to changed material properties.

2.4.1 Excitation and emission

Nanoscale structures and devices may exhibit striking emergent phenomena not present in bulk materials. Once the scale of a device approaches the limit of the Bohr radius of an exciton, the device is said to exhibit quantum confinement in said dimension [87]. As quantum dots are strongly confined in all three dimensions, they take on characteristics of a 0-dimensional structure. At 10K, where the excitation of the quantum dots takes place, the band gap of unstrained bulk GaAs is 1.52 eV (816 nm) [88], and the band gap of unstrained bulk InAs is 0.41 eV (3.024 µm) [89]. The bandgap in quantum dots, however, is larger than the bandgap of the same material in bulk. An approximation for the energy gap in a quantum dot can be calculated using the Brus formula,

$$E_{g,\text{dot}} \approx E_g + E_{\text{confinement}} + E_{\text{Coulomb}} \approx E_g + \frac{\hbar^2\pi^2}{2R^2}\left[\frac{1}{m_e} - \frac{1}{m_h}\right] - \frac{1.8e^2}{\varepsilon R}. \qquad (2.16)$$

Here $\hbar = h/2\pi$ is the reduced Planck's constant, R the diameter of the quantum dot, $m_{e/h}$ the effective mass of the electron (hole) [90]. For low values of R, the positive term will be dominant and the bandgap will thus increase as the size of the dot decreases. The bandgaps of the InAs quantum dots grown on the wafers utilized for this thesis have been experimentally found to lie in the interval 1.31-1.35 eV (920-945 nm). Optical excitation with an above-band laser with a photon energy $E > E_{g,\,\text{GaAs}}$ will excite an electron from the bulk GaAs valence band to the bulk GaAs conduction band, as can be seen in Fig. 2.5(b). This electron, and the corresponding hole in the valence

band, will form a bound state called the exciton, which is free to move. The exciton will be carried to the wetting layer and then the quantum dot where it eventually will recombine, emitting a photon with energy $E_{g,\,\mathrm{dot}}$ in the process.

2.4.2 Decay dynamics and selection rules

Epitaxially grown InAs quantum dots have a large discrepancy in their dimensions. Due to the quantum dots being significantly more confined in the z-direction than the x- or y-direction, the natural quantization axis is oriented along the z-direction. This confinement splits up the heavy hole (HH) and light hole (LH) states, which are otherwise degenerate at the zone center [91].

Electrons and holes are both fermions, which by definition have half-integer total angular momentum, which is given as $j = l + s$, where l is the orbital angular momentum and s is the spin [92]. The HH_z state of the valence band has angular momentum, j, and projection along the growth direction, j_z, is $|j = 3/2, j_z = \pm 3/2\rangle$. The electron in the conduction band has the state $|j_e = 3/2, j_{e,z} = \pm 1/2\rangle$. From this, there are four states characterized by the total spin $j_{\mathrm{tot}} = j_z + j_{e,z}$. It can be seen that the possible values for j_{tot} are ± 1 and ± 2. As photons have angular momentum ± 1, the only allowed recombination is $j_{\mathrm{tot}} = \pm 1$. For this reason, exciton doublets with $j_{\mathrm{tot}} = \pm 1$ and $j_{\mathrm{tot}} = \pm 2$ are respectively called bright and dark excitons.

While the bright exciton can emit a photon straight away by recombining the hole and the electron, the dark exciton can only decay after undergoing a spin flip. This leads to the decay being explained by a biexponential model [93],

$$\rho(t) = A_f \mathrm{e}^{-\gamma_f t} + A_s \cdot \mathrm{e}^{-\gamma_s t}. \tag{2.17}$$

2.4.3 Coupling

In the Jaynes-Cummings model, the Hamiltonian of a single two-level atom or emitter interacting with a single mode electric field can be described as a sum of three Hamiltonians

$$H_{\mathrm{tot}} = H_{\mathrm{A}} + H_{\mathrm{F}} + H_{\mathrm{int}}. \tag{2.18}$$

Here $H_{\mathrm{A}} = \frac{1}{2}\hbar\omega_0\hat{\sigma}_3$ is the free atomic Hamiltonian, $H_{\mathrm{F}} = \hbar\omega\hat{a}^\dagger\hat{a}$ the free-field Hamiltonian, and $H_{\mathrm{int}} = -\hat{\mathbf{d}}\cdot\hat{\mathbf{E}}$, where $\hat{\mathbf{d}} = \mathbf{d}^*\hat{\sigma}_{eg} + \mathbf{d}\hat{\sigma}_{ge}$ is the transition dipole moment and $\hat{\mathbf{E}} = \mathbf{E}(\hat{a} + \hat{a}^\dagger)$ [67]. The interaction Hamiltonian thus has four terms,

$$H_{\mathrm{int}} = -(\mathbf{d}^*\hat{\sigma}_{eg} + \mathbf{d}\hat{\sigma}_{ge})\cdot\mathbf{E}(\hat{a} + \hat{a}^\dagger) \tag{2.19}$$

$$= -\left(\mathbf{d}^*\cdot\mathbf{E}\hat{\sigma}_{eg}\hat{a} + \mathbf{d}^*\cdot\mathbf{E}\hat{\sigma}_{eg}\hat{a}^\dagger + \mathbf{d}\cdot\mathbf{E}\hat{\sigma}_{ge}\hat{a} + \mathbf{d}\cdot\mathbf{E}\hat{\sigma}_{ge}\hat{a}^\dagger\right). \tag{2.20}$$

Two of the four terms, however, are unphysical. This is $\hat{\sigma}_{eg}\hat{a}^\dagger$ and $\hat{\sigma}_{ge}\hat{a}$, which respectively correspond to the emitter going from the excited state to the ground state while absorbing a photon, and the emitter going from the ground state to the excited state while emitting a photon. By changing into the interaction picture, it can be seen that these terms oscillate rapidly. These terms correspond to extremely short-lived forces

mediated by virtual photons, and can safely be neglected, leaving the final interaction Hamiltonian in the rotating wave approximation as [94]

$$H_{\text{int}} = -\left(\mathbf{d}^* \cdot \mathbf{E}\hat{\sigma}_{eg}\hat{a} + \mathbf{d} \cdot \mathbf{E}\hat{\sigma}_{ge}\hat{a}^\dagger\right). \tag{2.21}$$

The interaction Hamiltonian is thus dependent on the dot product of the interaction dipole and the electric field, requiring those to have overlapping vector components. This mediates possible interactions between the different waveguide modes, and the quantum dot dipoles.

2.4.4 Emission and collection

An important figure of merit for quantum emitters is the β-factor, which is the proportion of the emitted photons being channeled into the desired mode, calculated as

$$\beta = \frac{\gamma_{\text{wg}}}{\gamma_{\text{wg}} + \gamma_{\text{rad}} + \gamma_{\text{nrad}}}. \tag{2.22}$$

Here γ_{wg} is the decay rate of the quantum dot into the guided mode of the waveguide, γ_{rad} is the non-guided radiative decay rate, meaning radiated light that fails to couple into the waveguide mode, and γ_{nrad} is the non-radiative decay rate. The β-factor is one important contribution to the brightness, with the repetition rate of the pump laser being another. The ultimate limit for the brightness of a single quantum dot is its lifetime, as that signifies the maximum rate that the quantum dot can emit single photons at [95].

In addition to the quality of the single photon source itself, the collection efficiency must also be considered. While thin suspended films of GaAs with InAs quantum dots in theory can function as single photon emitters, the collection efficiency will be exceedingly low. Efficient collection of emitted single photons thus requires engineering of the surrounding media to ensure that emission of light into undesirable modes is suppressed, while emission of light into desirable modes or directions is enhanced. Coupling can happen with microcavities [96], micropillars [97] or by emitting the single photons directly into a waveguide.

By placing the quantum emitters in suspended waveguides, the emitted single photons can be guided directly into the waveguide mode. This can further be enhanced in photonic crystal waveguides, which can be engineered to make the emission wavelength a forbidden wavelength for the photonic crystal surrounding the waveguide, enforcing emission into the waveguide and the waveguide only. In photonic crystal waveguides, $\beta \geq 98.4\%$ has been measured in [25].

2.5 Summary and connection

The purpose of this chapter was to build an overview of the fields of integrated photonics and quantum computation separately, and then unify them into the topic of integrated quantum photonics. Out of the many potential platforms for quantum computing, integrated quantum photonics has unique advantages of miniaturization and

scalability, as well as the qubit of choice — the single photon — being easy to create in abundance.

In integrated photonics, the material platform of choice shapes the capabilities of the integrated photonics circuit, with each platform providing both advantages and disadvantages. Choosing a platform requires deciding on non-negotiable qualities, while developing methods of offsetting or compensating for the drawbacks of the respective platforms. III—V materials provide promising platforms for integrated quantum photonics, as the compatibility with quantum dots enables direct interfacing with high-quality single-photon emitters. By utilizing an integrated photonics platform containing passive beam splitters and programmable phase shifters, a unitary gate providing complete control of the photon state can be created. Having presented the fundamentals of integrated quantum photonics on a GaAs platform, the natural next topic is control of guided modes in integrated photonics, which will be presented in the next chapter.

Chapter 3

Control in Integrated Photonics

Programmable integrated photonics provide a promising platform for quantum computing utilizing photons as flying qubits [98]. The active control of the propagation of light in an integrated circuit is carried out by changing the effective refractive index of a guided mode. Due to the richness of material physics, many avenues of obtaining such a change are possible, although constraints set by the material platform or experimental requirements might render certain strategies impossible or infeasible. This section will contain an overview of commonly used switching strategies, such as thermo-optic, electro-optic, and nano-opto-electro-mechanical systems (NOEMS) [99] switching. The methods will be introduced and discussed, and advantages and disadvantages of the different types of switching will be compared and discussed, and the decision to use NOEMS as the actuation mechanism of choice is justified. A review of two of the most common optical devices - the beam splitter and the phase shifter - is carried out, and the application of NOEMS to realize such devices is discussed.

3.1 Programmability and unitary gates

Programmability in integrated photonics refers to the ability to dynamically modify the embedded optical elements, changing the properties of the integrated circuit. Reconfigurable optical elements can allow for the implementation of arbitrary unitary gates, leading to control over the photon states. By cascading reconfigurable systems, large programmable circuits capable of carrying out complex operations can be created.

3.1.1 Beam splitters and phase shifters

Beam splitters allow for power splitting and directional control of light in both integrated, fiber, and free-space setups. While the beam splitters considered for theoretical purposes often fall under the special case of lossless, balanced, and symmetric beam splitters, considering the general case of lossy, imbalanced, and asymmetric beam splitters yields important knowledge about the propagation of light in a non-idealized system. Furthermore, as any optical setup with two inputs and two outputs

can be modeled as a series of compounded scattering matrices, developing a solid understanding of the behavior of arbitrary beam splitters can provide a shortcut to understanding complex optical circuits.

Scattering matrices describe a transformation of a 2×2 mode [100],

$$\begin{bmatrix} E_{O,1} \\ E_{O,2} \end{bmatrix} = \begin{bmatrix} S_{11} & S_{12} \\ S_{21} & S_{22} \end{bmatrix} \begin{bmatrix} E_{I,1} \\ E_{I,2} \end{bmatrix}, \tag{3.1}$$

where $E_I = [E_{I,1}, E_{I,2},]^T$ is the input mode and $E_O = \left[E_{O,1}, E_{O,2},\right]^T$ is the output mode. To get the intensity, each channel on the output is squared, and the absolute value is taken.

$$\begin{aligned} I_1 &= \frac{cn\varepsilon_0}{2}|E_{O,1}|^2 = |S_{11}E_{I,1} + S_{12}E_{I,2}|^2, \\ I_2 &= \frac{cn\varepsilon_0}{2}|E_{O,2}|^2 = |S_{21}E_{I,1} + S_{22}E_{I,2}|^2. \end{aligned} \tag{3.2}$$

Cascaded optical elements can be modeled by compounding scattering matrices from the last to the first,

$$S_{\text{tot}}\mathbf{E}_I = S_n ... S_2 S_1 \mathbf{E}_I, \tag{3.3}$$

If utilized for quantum optical purposes, the quantum optical scattering matrix must be unitary, with the transformation imposed by the scattering matrix conserving the Euclidean norm of the input vector. Lossy beam splitters can, however, be modeled in quantum mechanical formalisms with the addition of noise operators [101]. When dealing with classical elements, there is no such requirement, and losses can be incorporated by defining non-unitary scattering matrices. A scattering matrix describing an attenuation $I = I_0 L$ or $E = E_0\sqrt{L}$, where $0 \leq L \leq 1$ on one path while not transforming the other path can be written out as

$$S_L = \begin{bmatrix} \cos(\theta_L) & 0 \\ 0 & 1 \end{bmatrix}, \tag{3.4}$$

where $\theta_L = \arccos\left(\sqrt{L}\right)$. Similarly, a scattering matrix describing a phase shifter with phase shift ϕ can be written as

$$S_\phi = \begin{bmatrix} e^{i\phi} & 0 \\ 0 & 1 \end{bmatrix}. \tag{3.5}$$

An arbitrary beam splitter can be described with the following scattering matrix [102]

$$S_{\text{BS}} = \begin{bmatrix} t & \rho e^{i\phi_2} \\ r e^{i\phi_1} & \tau \end{bmatrix}, \tag{3.6}$$

where t, τ, r and ρ are positive real numbers, and ϕ_1 and ϕ_2 are phases describing the phase difference between transmission and reflection for respectively input port 1 and 2. As mentioned earlier, the scattering matrix S_{BS} need not be unitary, although energy conservation requires that $t^2 + r^2 \leq 1$ and $\tau^2 + \rho^2 \leq 1$. Special cases for the beam splitter include the balanced beam splitter for which $t = r$ and $\tau = \rho$, as well

as the symmetric beam splitter where $t = \tau$ and $re^{i\phi_1} = \rho e^{i\phi_2}$ [102]. For a lossless system, the determinant of the scattering matrix is 1,

$$\det(S) = t\tau - r\rho e^{i(\phi_1+\phi_2)} = 1. \tag{3.7}$$

As all values in the scattering matrix are positive real numbers with an amplitude less than 1, it can clearly be seen that this is the case only for $\phi_1 + \phi_2 = \pi$. Furthermore, by inserting the energy conservation terms, $t^2 + r^2 = 1$ and $\tau^2 + \rho^2 = 1$, it can be shown that any lossless beam splitter is additionally symmetric, $t = \tau$ and $r = \rho$. A scattering matrix for an arbitrary lossless beam splitter can therefore be written up as

$$S = \begin{bmatrix} t & i\sqrt{1-t^2} \\ i\sqrt{1-t^2} & t \end{bmatrix} = \begin{bmatrix} \cos(\theta) & i\sin(\theta) \\ i\sin(\theta) & \cos(\theta) \end{bmatrix}, \tag{3.8}$$

where θ is an angle corresponding to the rotation of the light between the two output states.

The scattering matrix formalism can be utilized to illuminate the dynamics of complex optical circuits. As an example, one can assume an MZI containing two identical lossless symmetric beam splitters with transmission t and reflectivity r, and a lossless phase shifter inducing a phase shift ϕ on one arm. The total circuit can be written up as

$$\begin{bmatrix} E_{O,1} \\ E_{O,2} \end{bmatrix} = \begin{bmatrix} t & ir \\ ir & t \end{bmatrix} \begin{bmatrix} e^{i\phi} & 0 \\ 0 & 1 \end{bmatrix} \begin{bmatrix} t & ir \\ ir & t \end{bmatrix} \begin{bmatrix} E_{I,1} \\ E_{I,2} \end{bmatrix} \tag{3.9}$$

$$= \begin{bmatrix} e^{i\phi}t^2 - r^2 & irt\left(e^{i\phi}+1\right) \\ irt\left(e^{i\phi}+1\right) & t^2 - e^{i\phi}r^2 \end{bmatrix} \begin{bmatrix} E_{O,1} \\ E_{O,2} \end{bmatrix}. \tag{3.10}$$

Inserting that $r^2 = 1 - t^2$ and $r = \sqrt{1-t^2}$,

$$\begin{bmatrix} E_{O,1} \\ E_{O,2} \end{bmatrix} = \begin{bmatrix} t^2(e^{i\phi}+1) - 1 & it\sqrt{1-t^2}\left(e^{i\phi}+1\right) \\ it\sqrt{1-t^2}\left(e^{i\phi}+1\right) & t^2(1+e^{i\phi}) - e^{i\phi} \end{bmatrix} \begin{bmatrix} E_{I,1} \\ E_{I,2} \end{bmatrix}. \tag{3.11}$$

This compound system is symmetric and lossless. Furthermore, the transformation imposed by the scattering matrix system is identical for transmittivity values $t = x^2$ and $t = \sqrt{1-x^2}$, as can be confirmed from the individual entries of the matrix in equation (3.11).

Fig. 3.1 shows the behavior of a lossless MZI with a variable phase shifter ϕ and identical two symmetric beam splitters with transmittivity t. Defining the transmissive (reflective) paths as the terms described by the diagonal (off-diagonal) entries in the scattering matrix, it can be seen that both the transmissive and reflective paths are symmetric. The possible paths taken for a single photon on a transmissive (reflective) path are shown in Fig. 3.1(a) with the label T (R), with the color of each path corresponding to the equivalent matrix element in Eq. 3.11. The behavior of the lossless MZI with two identical beam splitters is shown in Figs. 3.1(b) and (c), where the phase-dependent behavior of the intensity in respectively the transmissive and reflective paths is shown. It can be seen that as t^2 approaches 0, the intensity will go towards

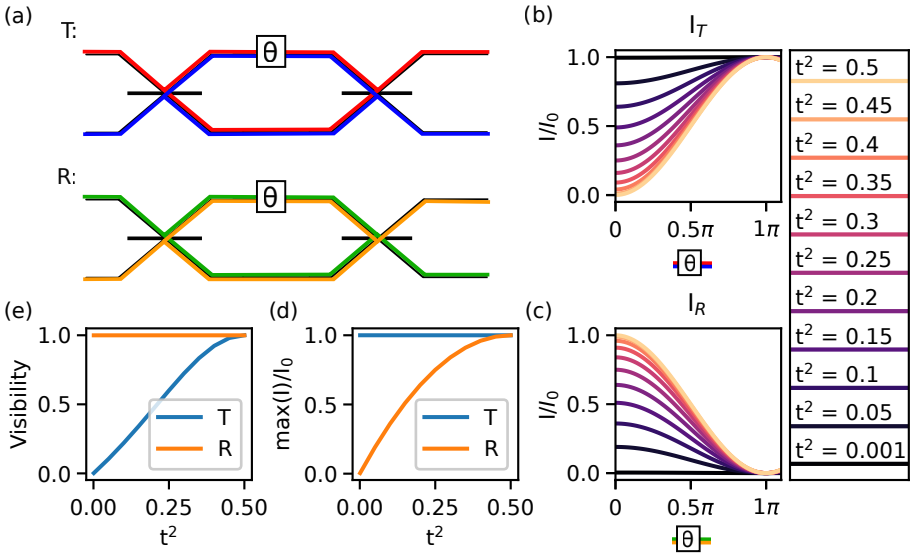

Figure 3.1: Transmittivity dependent behavior of the lossless MZI with a tunable phase on one arm and two identical symmetric beam splitters. Note the clockwise ordering of the subfigures. a: Transmissive (top) vs reflective (bottom) paths The color of each path corresponds to the color of the corresponding matrix entry in Eq. 3.11. b: Phase- and transmittivity-dependent intensity in the transmittive arms. c: Phase- and transmittivity-dependent intensity in the reflective arms. d: Transmittivity-dependence of the maximum fraction of the light channeled into respectively the transmissive and reflective arms. e: Transmittivity-dependence of the visibility in respectively the transmissive and reflective arms.

$I_0(0)$ for the T (R) paths. In Fig. 3.1(e), one of the most important properties of a beam splitter is illustrated, namely visibility, defined as the ability of a given beam splitter arm to obtain full extinction. The visibility of an arm in a MZI is defined as

$$\nu = \frac{I_{\max} - I_{\min}}{I_{\max} + I_{\min}}. \tag{3.12}$$

The maximum possible value of the visibility is $\nu = 1$, which signifies total extinction in that arm for $I_{\min}$, and the smallest possible value is $\nu = 0$, which signifies a total non-response to the phase shift.

In addition to visibility, it is useful to define an additional figure of merit that describes to which extent the MZI can channel all power into one arm. This can be described using the extinction ratio, which is typically measured in dB

$$ER = 10\text{dB}\log_{10}(I_i/I_j), \tag{3.13}$$

where $I_i(\phi)$ and $I_j(\phi)$ are the intensity in the i'th and j'th output path of the interferometer. The extinction ratio, however, is not normalized. An alternative is to use the fraction of the total optical power channeled into the desired path, $\max(I)/I_0$.

Figs. 3.1(e) and 3.1(d) illustrate respectively the visibility and the maximum fraction of the intensity for the transmissive and reflective paths of the symmetric lossless MZI with variable phase, plotted against t^2, or the square of the transmittivity of the

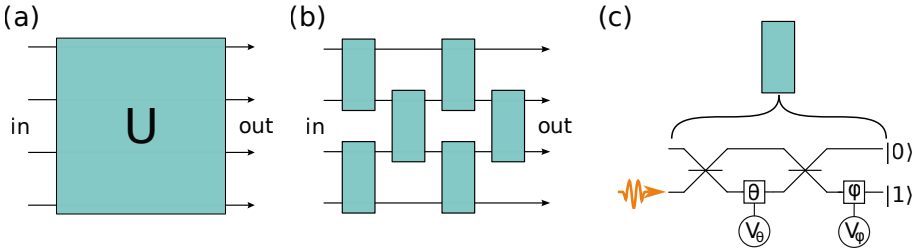

Figure 3.2: a: Sketch of a circuit showing an arbitrary unitary operator acting on N = 4 modes. b: Individual beam splitters acting on two modes. c: Photonic circuit capable of implementing arbitrary rotation of photon state upon application of a voltage V.

individual beam splitters. Due to the uniform behavior for $t = x^2$ and $t = \sqrt{1-x^2}$, only the interval $0 \leq t^2 \leq 0.5$ is being swept over. It can be seen how, as values for t^2 diverge from 0.5, the visibility and maximum intensity transfer of a path are inversely correlated. Once again considering Figs. 3.1(b) and (c), the paths that retain $v = 1$ will have the minimum stay constant, while the maximum intensity is lowered, and the paths for which total power transfer is possible will retain their maximum intensity while the minimum intensity rises.

3.1.2 Mach-Zender-Interferometers containing lossy phase shifters

Loss is unavoidable in integrated optical circuits, and the insertion of optical elements such as phase shifters often causes additional losses. If the arm of the MZI that contains the variable phase shifter additionally contains a loss, the scattering matrix can be adjusted to be the following,

$$\begin{bmatrix} E_{O,1} \\ E_{O,2} \end{bmatrix} = \begin{bmatrix} t^2(\cos(\theta_L)e^{i\phi}+1)-1 & it\sqrt{1-t^2}\left(\cos(\theta_L)e^{i\phi}+1\right) \\ it\sqrt{1-t^2}\left(\cos(\theta_L)e^{i\phi}+1\right) & t^2+\cos(\theta_L)e^{i\phi}(t^2-1) \end{bmatrix} \begin{bmatrix} E_{I,1} \\ E_{I,2} \end{bmatrix}. \quad (3.14)$$

For the lossless MZI with two identical beam splitters, a given output path was guaranteed to enable either total extinction or total power transfer, no matter the value of t. For the MZI with a loss mismatch between the paths, this is no longer the case, even in the case of balanced beam splitters where $t^2 = 0.5$. Additionally, the diagonal terms will no longer yield the same efficiency for $t = x$ and $t = \sqrt{1-x^2}$. Furthermore, the beam splitter described by the scattering matrix is no longer symmetric, as the transformations induced by the diagonal terms are no longer identical for $t^2 \neq 0.5$. This effect can be offset by adding a similar loss L to the other arm of the interferometer, which enables better visibility at the cost of higher total loss in the circuit.

3.1.3 Unitary gates

As shown in 3.1.1, a lossless MZI consisting of two identical 50/50 beam splitters and a variable phase shifter can obtain an arbitrary rotation of light between the two output ports, which corresponds to being able to perform an arbitrary rotation between the

$|0\rangle$ and $|1\rangle$ states. If an additional programmable lossless phase shifter is added before or after the MZI, this allows for complete control of the photon state, as mentioned in section 2.3.1 [103]. This circuit can thus implement any 2×2 unitary matrix, i.e. any transformation in U(2) [104]. It has been shown that this can be generalized for a system with N input states and N output states, where a reconfigurable unitary $N \times N$ matrix able to perform an arbitrary linear transformation between the input and output states can be created by cascading $N(N-1)/2$ universal 2×2 unitary gates, as seen in Fig. 3.2 [105]. However, as shown in the previous section, existence of imperfections in the form of losses and imbalanced beam splitters will lead to limited visibility of the individual MZIs, lowering the fidelity of the circuit. Furthermore, as different wavelengths will couple differently to the directional coupler beam splitter, they will experience different splitting ratios in the same beam splitter. If it is desired to be able to utilize a quantum optics setup at multiple wavelengths, precautions can be taken to ensure maximal configurability. One possibility is to replace the static beam splitters with configurable beam splitters, either in the form of programmable directional couplers, or MZIs with embedded controllable phase shifters [106], although the latter approach comes with the risk of introducing additional losses. Another solution is the addition of an extra layer of MZIs at the end of the circuit, although this method becomes drastically less effective the larger the circuit [107]. No matter the chosen approach, the design and fabrication of high-quality and low-loss waveguides, beam splitters, and phase shifters is a priority towards the development of integrated photonics for quantum processing.

3.2 Modulation strategies

A phase shift can be induced in an integrated waveguide by changing the effective refractive index in a section of the waveguide, which will change the accumulated phase in that section of the waveguide. A configurable beam splitter can be designed similarly by enabling the control of the effective index in an integrated directional coupler, which changes the coupling between the two waveguides. A multitude of material effects enabling control over the effective refractive index of a guided mode exists, with a few of the most commonly utilized being introduced here.

3.2.1 Thermo-optic modulation

The material refractive index is a property that depends on the crystal structure of the material. Materials undergoing changes in temperature tend to shrink or expand, and the resulting change in the crystal structure will again induce a change in the material refractive index. Thermo-optic phase shifters are well-developed on silicon platforms and can be fabricated with almost zero insertion loss [57], but are prone to thermal crosstalk. Depending on the design and heater type, heating and cooling times tend to be in the order of $10-40\,\mu s$ for silicon-on-insulator platforms, and $100-700\,\mu s$ for undercut silicon platforms [108]. Thermo-optic phase shifters are typically long, with lengths upwards of 1 mm not unheard of, although shorter designs with lengths $< 10\,\mu m$ have been designed [109]. Furthermore, as keeping the waveguide at the

desired temperature requires a constant energy supply, heat from the waveguide will dissipate to the surroundings. To compensate for this, designs can be made to isolate the phase shifter from the surroundings, such as by utilizing suspended devices, or by designing devices with spiral or curved waveguides where heat dissipated from one part of the waveguide is absorbed by the other waveguides [110, 111]. However, waste heat is still undesirable in quantum photonics applications, where the GaAs quantum dots require a low temperature $T < 10\,\mathrm{K}$ to freeze out phonons. Even if a perfectly thermally isolated design was made, thermo-optic phase shifters on cryogenic GaAs remain unviable. Two terms dominate the temperature-dependent refractive index change, namely the term proportional to the thermal expansion coefficient, and the term proportional to the temperature dependence of the bandgap,

$$\left(\frac{\mathrm{d}n}{\mathrm{d}T}\right)_{\text{expand}} \propto \alpha, \qquad \left(\frac{\mathrm{d}n}{\mathrm{d}T}_{\text{bandgap}}\right) \propto \frac{1}{E_g}\frac{\mathrm{d}E_g}{\mathrm{d}T}. \tag{3.15}$$

Here n is the refractive index, α is the thermal expansion coefficient, T the temperature, and E_g the excitonic bandgap [112]. For GaAs, the bandgap energy is

$$E_{g,\,\mathrm{GaAs}}(\mathrm{T}) = 1.514\,\mathrm{eV} - \frac{5.405\cdot 10^{-4}\mathrm{T}^2}{\mathrm{T}+204}, \tag{3.16}$$

leading to

$$\frac{\mathrm{d}E_{g,\,\mathrm{GaAs}}}{\mathrm{d}T} = -\frac{(5.405T^2+2205T)\cdot 10^{-4}}{(T+204)^2}, \tag{3.17}$$

where T is the temperature in Kelvin [88]. The value of $\frac{\mathrm{d}E_g}{\mathrm{d}T}$ thus reaches a minimum at $T = 0$. Similarly, the thermal expansion coefficient of GaAs has also been found to approach zero at cryogenic temperatures [113]. The thermo-optic coefficient in GaAs at $T \sim 10\,\mathrm{K}$ is thus orders of magnitude lower than at room temperatures, leaving this strategy impractical.

3.2.2 Electro-optic modulation

Another strategy for routing in integrated photonics is to change the material refractive index by applying an electric field. The mechanism most commonly utilized for this is the Pockels effect, which is an effect where the refractive index changes linearly with the applied electric field [114]. Out of 32 crystal point groups, this effect is present in the 21 groups lacking inversion symmetry. By sheer coincidence (or not, as nothing is truly coincidental when it comes to the behavior of materials), this is also the same geometry required for piezoelectric materials, and thus any material that shows the Pockels effect is also piezoelectric.

Electro-optic switches can be extremely fast, with the Pockel's effect having responses down to femto-second times [114]. However, the small index change requires lengths in the order of several hundred microns on electro-optic switches [115]. Values of $V_\pi L = 0.1\,\mathrm{V}\cdot\mathrm{cm}$ have been achieved on GaAs [115], while values as low as $V_\pi L = 0.047\,\mathrm{V}\cdot\mathrm{cm}$ have been obtained on a hybrid InGaAsP metal-on-semiconductor

(MOS) interface [116]. Additionally, applying an electric field to a semiconductor induces a multitude of phenomena in addition to the Pockels effect. One is the aforementioned piezoelectric effect, which could produce undesirable warping of membranes in directions perpendicular to the direction of the applied electric field.

A phenomenon which limits the application of electro-optic Pockels effect switches on GaAs with quantum dots emitting at wavelengths $\lambda \sim 930$nm, which is the focus of this thesis, is Franz-Keldysh electro-absorption [26]. Under normal conditions, transmission of light in a lossless semiconductor waveguide will have an abrupt cutoff when the wavelength of the light falls below the absorption wavelength corresponding to the absorption edge. All light with energies below the bandgap should be transmitted, and all light with energies above the bandgap should be absorbed. However, in the presence of a strong electric field, the wavefunctions are distorted, effectively smearing out the absorption edge and giving it an exponential tail into the bandgap [117]. In comparison to a bandgap shift, which can be induced by effects such as strain [118], which would shift the absorption edge while keeping the sharp nature of the transition, the Franz-Keldysh effect induces a gradual loss close to the band edge.

While this can be ignored in some materials, such as Lithium Niobate where the room temperature band gap is $E_{g,\mathrm{LiN}} = 3.77\,\mathrm{eV}$, corresponding to a wavelength of 328 nm, which is safely far away from typical wavelengths used in quantum photonics ($900 - 1550\,\mathrm{nm}$), this is a critical issue for the chosen GaAs platform. The GaAs bandgap at 10 K is $1.52\,\mathrm{eV}\,(816\,\mathrm{nm})$, which is sufficiently close to the utilized wavelengths at $920 - 940\,\mathrm{nm}$ that large losses will be induced in the device. Electro-optic switching is thus infeasible for the GaAs platform at a 930 nm wavelength.

3.2.3 Phase change materials

Modulation using phase change materials (PCMs) utilizes the difference in optical properties between two states of matter of a material, typically a stable crystalline and an amorphous phase [119]. These two states have different material refractive indices, changing the propagation of light through waveguides. The actuation method of a phase change material can be either through electrothermal, electrical, or optical means, all of which induce a temperature change, inducing a phase transition in the PCM [120]. PCMs are typically non-volatile, with static power consumption close to zero. While commercial PCMs used in storage discs such as CDs are stable for years, PCMs used for integrated photonics can have stable optical responses over tens of days [121].

The low-loss PCM Sb_2Se_3, which has a material refractive index $n_a = 3.285\,(n_c = 4.05)$ in the amorphous (crystalline) state, is a promising PCM for integrated photonics due to its wide bandgap and large refractive index contrast [122]. It has been demonstrated in micro-ring resonators, where a 6 µm long phase shifter placed in a micro-resonator ring had a low insertion loss of $-0.33\,\mathrm{dB}$ while providing a $V_\pi L = 0.496\,\mathrm{V}\cdot\mathrm{cm}$ [123].

One disadvantage to phase change materials is the added complexity of fabrication, as they require the deposition of an additional material. Another challenge is present due to the limited durability of the phase change materials. Switching a phase

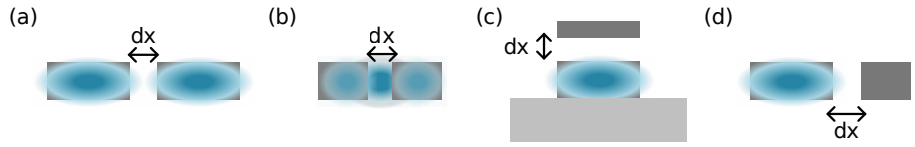

Figure 3.3: Different types of design utilizing NOEMS, along with sketches of electric field distribution. a: Directional Coupler b-d: Phase shifters. b: Slot waveguide phase shifter. c: Phase shifter using flat perturbing cantilever with vertical displacement. d: Phase shifter using narrow perturbing cantilever with horizontal displacement.

change material between the amorphous and crystalline states, or vice versa, involves high temperatures ($T_m > 600°$C to transition to the amorphous state of Sb_2Se_3) [121].

Additionally, many devices produced using phase change materials are binary devices, meaning that the phase-shift itself is not tunable. While this is satisfactory for some cases, such as tuning a ring resonator in and out of resonance, or switching a mode between two outputs, many optical applications require complete reconfigurability, where any given phase in the interval $0 < \phi < 2\pi$ is obtainable. Multi-level devices, such as long waveguides covered in short PCM pixels, each of which can be in either the amorphous or crystalline state, could allow a wider freedom of modulation [124]. Modulation of the phase shift by controlling the length of electro-thermal pulses to obtain partial amorphization has also been demonstrated [121].

3.2.4 Mechanical actuation - NOEMS

Electro-optic, thermo-optic and PCM tuning all induce a change in the material refractive index. However, the effective index of a guided mode depends not only upon the material effective index, but also the geometry of the waveguide and its surroundings. By displacing nano-cantilevers using mechanisms such as electrostatic or piezoelectric forces, the effective refractive index in a guided mode can be perturbed or modulated [125]. This property lays the foundation for tuning with nano-opto-electro-mechanical-systems (NOEMS) [99].

Beam splitters have been realized using NOEMS, where they can be used to displace the two waveguides [27], as can be seen in Fig. 3.3(a). NOEMS phase shifters have been realized using single slot waveguides [31], as can be seen in Fig. 3.3(b) or double [32] slot waveguides, where the actuation is carried out by exploiting the gap dependence of the effective refractive index of the guided mode. Additionally, designs where the mode in a wider bus waveguide is perturbed by the presence of nearby narrower movable cantilevers have been demonstrated. This is the case both for slab waveguides fabricated on substrates with a perturbing cantilever suspended above as shown in Fig. 3.3(c) [30], and for suspended waveguides with the actuated cantilever moving in-plane as seen in Fig. 3.3(d) [29]. The maximally attainable frequency of these devices is their lowest eigenfrequency, which typically lies in the 100s of kHz range [29]. NOEMS are compatible with suspended GaAs waveguides with light at 930 nm at 10 K, and have been chosen as the method of modulation in this thesis.

However, elastic properties of materials are temperature-dependent, which can lead to different behavior at cryogenic temperatures. NOEMS typically consist of

layers of different materials with different thermal expansion coefficients, which can lead to warping and deformation when the devices are cooled down [126]. Another drawback to the NOEMS method is the fragility of MEMS devices. The narrow cantilevers are prone to breakage or collapse during fabrication. If two cantilevers come into physical contact with each other, they can fuse together due to short-range van-der-Waals forces and not come apart again. Furthermore, the suspended devices are typically sufficiently fragile that if allowed to air-dry after fabrication, the surface tension of the liquid, such as 2-propanol (IPA) or water, can cause collapse due to stiction. This can be avoided by using a critical point dryer (CPD) [127].

Care must be taken not to destroy the fragile NOEMS devices during operation. Fast, sudden changes in temperature can collapse the devices as they buckle and bend to compensate for thermal stresses, and when cooling down, the temperature change should be kept below $8\,\mathrm{K/min}$. Before use, the device should be theoretically characterized to derive any potential pull-in voltages, meaning the voltage where the cantilevers of the actuation mechanism snap together.

NOEMS are additionally sensitive to electrostatic discharges (ESD) and electric overstress (EOS), both of which can cause failure in MEMS devices [128]. ESD events are sudden, short-lived discharges of electricity, which can cause severe thermal damage to integrated circuits. Furthermore, the short-lived, strong bursts of electricity can cause large displacements of NOEMS cantilevers, breaking them or causing them to collapse together. Whereas ESD is a singular, short-lived event, EOS damage happens over time for a device driven too harshly. When a device is subjected to a too high current or voltage, resistive heating can cause degradation of parts which accumulate over time. Protection against ESD events involves proper grounding and wearing antistatic wristbands when mounting the device in the cryostat and carrying out electrical operations to prevent discharges induced by static electricity [129]. Furthermore, to prevent unwanted transients from the function generator, the NOEMS devices should be driven with continuous waveforms (e.g. sinusoidal or triangular), and the amplitude of the waveforms should be ramped up and down slowly ($< 1\,\mathrm{V/s}$) in steps of a few hundred mV.

3.2.5 Summary and comparison

Of the three most common strategies for routing photons in integrated circuits (thermo-optic, Pockels electro-optic, and mechanical tuning), mechanical tuning is the only method that is compatible with GaAs at 930 nm. While devices utilizing mechanical tuning are fragile and must be carefully handled to avoid failure induced by electric stresses and discharges, they offer a compact, fast, and low-power-consumption strategy for routing photons in integrated quantum photonic circuits.

	Thermo-optic	Electro-optic	NOEMS
Speed	$\sim 10\,\mu s$	$< 10\,ns$	$< 10\,\mu s$
Length	$> 100\,\mu m$	$> 100\,\mu m$	$< 100\,\mu m$
Yield	High	High	Low
GaAs 930 nm compatible?	Yes	No	Yes
10 K compatible?	No	Yes	Yes
Notes	Large power use		Fragile

Table 3.1: Comparison of typical figures of merit for common techniques for continuous modulation of phase shift in integrated photonic circuits. Values obtained from extended data table in [29].

3.3 Active components in integrated quantum photonics

Having identified mechanical actuation as the ideal routing strategy for integrated quantum photonics on a GaAs platform, a strategy can be developed for how to carry out the application. Doing so requires a thorough understanding of the behavior of integrated circuits. In this section, a derivation of the properties of integrated photonic components is carried out, starting with waveguides, and continuing with beam splitters and phase shifters.

3.3.1 Integrated waveguides

Integrated waveguides are typically described with wave optics, due to having dimensions similar to the wavelengths of the guided light. While simplified cases exist where analytical but transcendental equations describing the behavior of guided modes can be found, theoretical analysis of the behavior of light propagating in waveguides is typically carried out using numerical software such as Lumerical or COMSOL.

Derivation of guided modes

By considering an infinite slab waveguide made of a material with thickness d and refractive index n_{wg}, sandwiched between surroundings with refractive index n_{s}, equations describing the propagation of modes in the waveguide can be derived [52]. The slab waveguide, a sketch of which can be seen in Fig. 3.4, has the slabs located in the zy-plane, with the wave propagating along the z-axis. Starting with the wave equation obtained from Maxwell's equations:

$$\nabla^2\mathbf{E}(\mathbf{r},t) - \mu_0\varepsilon_0 n^2(\mathbf{r})\frac{\partial^2}{\partial t^2}\mathbf{E}(\mathbf{r},t) = 0. \tag{3.18}$$

By assuming that the wave possesses a radial frequency ω, the Helmholtz equation can be derived,

$$\mathbf{E}(\mathbf{r},t) = \mathrm{Re}\left[\mathbf{E}(\mathbf{r})e^{i\omega t}\right] \Leftrightarrow \nabla^2\mathbf{E}(\mathbf{r}) + k^2 n^2(\mathbf{r})\mathbf{E}(\mathbf{r}) = 0. \tag{3.19}$$

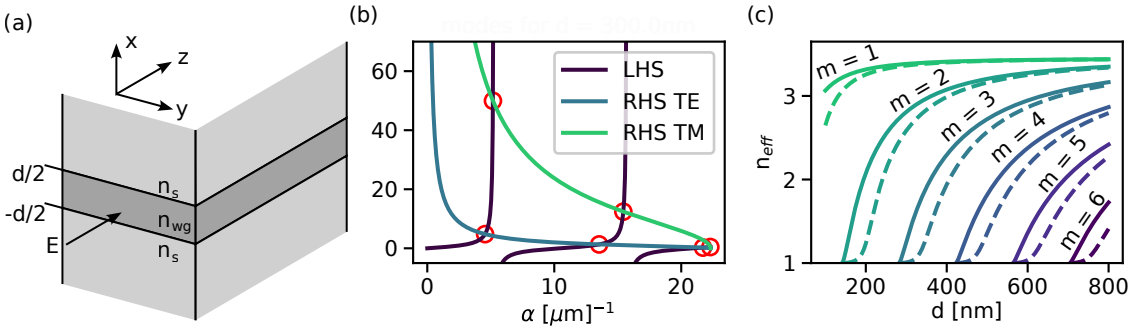

Figure 3.4: Modes in an infinite slab waveguide. a: Sketch of an infinite slab waveguide. b: Characteristic transcendental equations for a slab waveguide with $d = 300\,\text{nm}$, $\lambda = 930\,\text{nm}$, $n_{\text{wg}} = 3.45$ and $n_s = 1$. LHS marks the left-hand-side of Eq. (3.22), with RHS TE and TM marking the right hand sides of respectively Eqs. (3.22) and (3.23). Red circles marks the values of α which are solutions for the equation LHS = RHS. c: Thickness-dependence of guided modes in a slab waveguide with $\lambda = 930\,\text{nm}$, $n_{\text{wg}} = 3.45$ and $n_{\text{s}} = 1$. Solid lines mark TE modes and dashed lines mark TM modes, with the same color corresponding to the same mode.

By decomposing the equation into $\mathbf{E}(\mathbf{r},t) = \mathbf{E}(x,y)e^{-i\beta z}$, and assuming that the wave does not vary in the y-direction, $\frac{\partial}{\partial y} = 0$, the equations for the three different domains can be derived,

$$\begin{cases} \frac{\partial^2}{\partial x^2}E(x) + \left(k^2 n_{\text{s}}^2 - \beta^2\right)E(x) = 0 & x > d/2, \\ \frac{\partial^2}{\partial x^2}E(x) + \left(k^2 n_{\text{wg}}^2 - \beta^2\right)E(x) = 0 & -d/2 < x < d/2, \\ \frac{\partial^2}{\partial x^2}E(x) + \left(k^2 n_{\text{s}}^2 - \beta^2\right)E(x) = 0 & x < -d/2. \end{cases} \tag{3.20}$$

Guided modes require $kn_{\text{wg}} > \beta > kn_{\text{s}}$. If $\beta < kn_{\text{s}}$, the mode is leaky. Geometrically, this corresponds to the light hitting the inner wall of the waveguide at an angle too small to undergo total internal reflection. $\beta > kn_{\text{wg}}$ is an unphysical case where the diverging fields would exhibit exponential behavior everywhere. Making the following redefinitions, $\beta^2 + \alpha^2 = n_{\text{wg}}^2 k^2$ and $\beta^2 - \kappa^2 = n_{\text{s}}^2 k^2$, a general solution for the field can be written up as follows:

$$\text{E}(x) \begin{cases} A\exp(-\kappa(x - d/2)) & x > d/2, \\ B\cos(\alpha x) + C\sin(\alpha x) & -d/2 < x < d/2, \\ D\exp(\kappa(x + d/2)) & x < -d/2. \end{cases} \tag{3.21}$$

Two main polarization modes are possible in waveguides. In the transverse electric (TE) mode, the E-field is entirely parallel to the propagation direction, while in the transverse magnetic (TM) mode, the H-field is entirely parallel to the propagation direction. In the TE mode, boundary conditions can be derived from Maxwell's equations, where it can be found that at both interfaces ($x = \pm d/2$) the electric field $E_y(x)$ and the magnetic field $B_z(x) = \frac{1}{\omega}\frac{\partial}{\partial x}E_y(x)$ are continuous. This gives four equations ($E_y(x)$ and $B_z(x)$ at each of the two boundaries), which allows eliminating the four

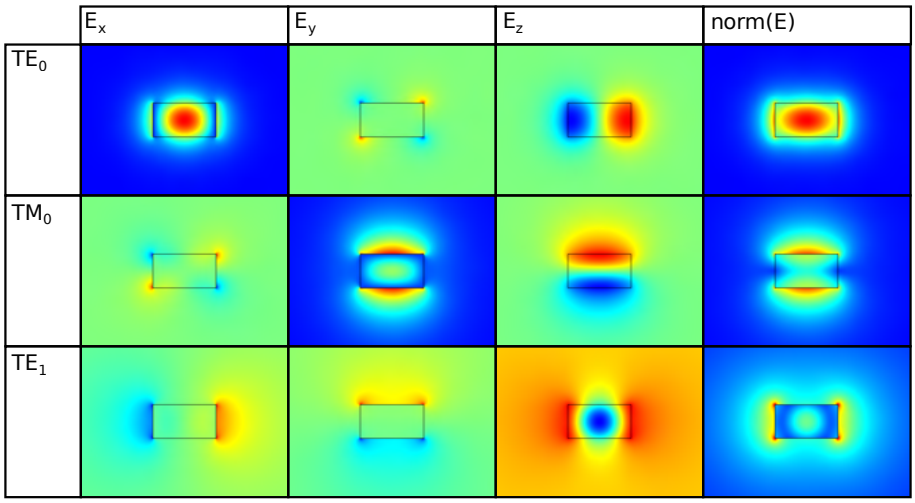

Figure 3.5: Electric field distribution of the guided modes with wavelength $\lambda = 930\,\text{nm}$ in a waveguide made of GaAs ($n = 3.45$) surrounded by air ($n = 1$) with a width of $d = 300\,\text{nm}$ and a height of $h = 160\,\text{nm}$. Three guided modes are present in the waveguide, namely TE_0 ($n_{\text{eff,TE}_0} = 2.37$), TM_0 ($n_{\text{eff,TM}_0} = 1.46$) and TE_1 ($n_{\text{eff,TE}_0} = 1.05 - 1.96 \cdot 10^{-5} i$) modes.

constants (A, B, C, D), while leading to the following condition

$$\tan(\alpha d) = \frac{2\alpha\kappa}{\alpha^2 - \kappa^2}. \tag{3.22}$$

This transcendental equation solves for the allowed values of β for light with frequency ω in a waveguide with width d and effective refractive index n_{wg}, and effective refractive index of the surroundings n_{s}. A similar derivation can be carried out for the TM mode, where the characteristic transcendental equation can be shown to be

$$\tan(\alpha d) = \frac{2m_{12}\kappa\alpha}{\alpha^2 - (m_{12}\kappa)^2}, \quad m_{12} = \left(\frac{n_1}{n_2}\right)^2. \tag{3.23}$$

From here, the modes can be found graphically by plotting the left-hand side (LHS) and right-hand side (RHS) together, and identifying their intersecting points. The LHS and RHS of the transcendental equation describing a slab waveguide made of GaAs ($n = 3.45$) surrounded by air ($n = 1$) with wavelength $\lambda = 930\,\text{nm}$ can be seen in Fig. 3.4(b) for a thickness of $d = 300\,\text{nm}$. By identifying the intersections of the LHS and RHS sides, the values of α that lead to guided modes can be found, and the effective refractive indices can be calculated. Fig. 3.4(c) the calculated effective refractive index when sweeping over the thickness. Due to the infinite width of the slab, the solution for the infinite slab waveguide will contain modes that are not present in an integrated waveguide with finite width. In Fig. 3.5, an illustration of the electric field distributions of the modes found in a simulation created in COMSOL's wave optics module, using the same parameters as in the simulation shown in Fig. 3.4. Three modes are identified for wavelength $\lambda = 930\,\text{nm}$, namely TE_0 ($n_{\text{eff,TE}_0} = 2.37$), TM_0 ($n_{\text{eff,TM}_0} = 1.46$) and TE_1 ($n_{\text{eff,TE}_0} = 1.05 - 1.96 \cdot 10^{-5} i$).

3.3.2 Directional coupler beam splitters

An essential component of an integrated MZI is the directional coupler beam splitter. Consisting of two narrow parallel waveguides located close to each other, the overlap between the evanescent tail of the mode in one waveguide with the other waveguide causes a coupling between the waveguides, allowing the light to oscillate back and forth between the two waveguides with a beat length determined by the coupling strength.

Defining two lossless, single-mode waveguides lying in the yz-plane oriented along the z-axis and with the light polarized in the y-direction (TE mode), the individual electric fields can be written as.

$$E_{y,\,1/2}(x,y,z) = E_{y,\,1/2}(x,y)\mathrm{e}^{-i\beta_{1/2}z}. \tag{3.24}$$

Assuming that the total electric field is a linear superposition of the individual electric fields

$$E_{y,\,\mathrm{tot}}(x,y,z) = a_1(z)E_{y,\,1}(x,y)\mathrm{e}^{-i\beta_1 z} + a_2(z)E_{y,\,2}(x,y)\mathrm{e}^{-i\beta_2 z}, \tag{3.25}$$

For infinite distances between the cantilevers, there will be no coupling between the two waveguides, and thus a_1 and a_2 will be constant. As the two waveguides are moved closer and closer to each other, the evanescent tail of the mode in one waveguide will begin to overlap with the next waveguide. By using the theory of coupled modes, the following expressions for z-dependence of the waveguide amplitudes can be derived [52].

$$\frac{\partial}{\partial z}a_1(z) = -ig_{21}a_2(z)\mathrm{e}^{-i\Delta\beta z}, \tag{3.26}$$

$$\frac{\partial}{\partial z}a_2(z) = ig_{12}a_1(z)\mathrm{e}^{i\Delta\beta z}. \tag{3.27}$$

Here $\Delta\beta = \beta_2 - \beta_1$ is the phase mismatch between the waveguides, and $g_{12/21}$ the overlap integrals between the waves, which function as the coupling constants.

$$g_{12/21} = \frac{\omega\varepsilon_0}{4p_0}\int_{\mathrm{wg},\,1/2}\left[n_{1/2}^2(y) - n^2\right]E_1(y)E_2(y)\,\mathrm{d}y, \tag{3.28}$$

where p_0 is a normalization constant. This is an approximation that holds in the limit of weak coupling. It takes the overlap of each evanescent tail with the opposing waveguide into account, while neglecting the second-order term. from the overlap between the two evanescent tails.

If the waveguides are entirely symmetric, their coupling constants will also be identical, $g_{12} = g_{21} = g$. Defining $A_{1/2} = a_{1/2}\mathrm{e}^{-i\beta_{1/2}z}$, the coupled mode equations can be rewritten in matrix form

$$\frac{d}{dz}\begin{bmatrix}A_1(z)\\A_2(z)\end{bmatrix} = -i\begin{bmatrix}\beta_1 & g\\ g & \beta_2\end{bmatrix}\begin{bmatrix}A_1(z)\\A_2(z)\end{bmatrix}. \tag{3.29}$$

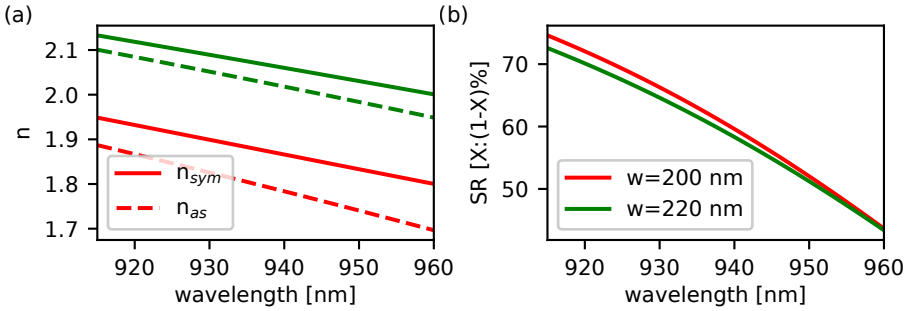

Figure 3.6: Wavelength-dependence of splitting ratio in directional coupler. a: Effective index of symmetric (line) and antisymmetric (dashed) modes in GaAs (n = 3.45) directional coupler with gap $g = 120\,\text{nm}$ and cantilever width $w = 200\,\text{nm}$ (red) and $w = 220\,\text{nm}$ (green). b: Wavelength dependence of splitting ratio (SR) of two directional coupler. The two devices have different Δn. As the desired SR is $\sim 50:50$ at $\lambda = 950\,\text{nm}$ and, the lengths of the two beam splitters are different, with $L = 2.5\,\mu\text{m}$ for $w = 200\,\text{nm}$ and $L = 5\,\mu\text{m}$ for $w = 220\,\text{nm}$

By diagonalizing this matrix, the eigenmodes and eigenstates of this system can be found,

$$\beta_{\text{s/as}} = -i\left(\beta \pm g\right), V = \begin{bmatrix} \pm 1 \\ 1 \end{bmatrix}. \tag{3.30}$$

The equation on matrix form can thus be diagonalized into the following expression,

$$\frac{d}{dz}\begin{bmatrix} A_{\text{s}}(z) \\ A_{\text{as}}(z) \end{bmatrix} = -i\begin{bmatrix} \beta + g & 0 \\ 0 & \beta - g \end{bmatrix}\begin{bmatrix} A_{\text{s}}(z) \\ A_{\text{as}}(z) \end{bmatrix}. \tag{3.31}$$

Solving this yields equations for the amplitudes of the normal modes

$$a_{\text{s}} e^{-i\beta_{\text{s}} z} = a_1(z)e^{-i\beta z} + a_2(z)e^{-i\beta z}, \tag{3.32}$$

$$a_{\text{as}} e^{-i\beta_{\text{as}} z} = a_1(z)e^{-i\beta z} - a_2(z)e^{-i\beta z}. \tag{3.33}$$

From beginning with two modes $a_1(z)$ and $a_2(z)$, each depicting the mode intensity in one waveguide, the eigenmodes have been found to be a symmetric mode, and an anti-symmetric mode. Both of these modes have the same amplitude of the electric field, but the symmetric mode has the same sign in each of the two cantilevers, while the fields in the anti-symmetric mode have opposite signs in the two cantilevers.

As these modes have different propagation constants, β_{s} and β_{as} with a difference of twice the coupling constant, $\beta_{\text{s}} - \beta_{\text{as}} = 2g$, this means that the light will couple between the modes, and the light will have transferred entirely between the cantilevers upon reaching the beat length

$$L_{\text{beat}} = \frac{\pi}{2g} = \frac{\pi}{\beta_s - \beta_{\text{as}}}. \tag{3.34}$$

The solution for the spatial dependence of the coefficients to the electric fields, as-

suming initial conditions $a_1(0) = a_0$ and $a_2(0) = 0$, is thus

$$a_1(z) = a_0\cos(gz) = a_0\cos\left(\frac{n_s - n_{as}}{\lambda}z\right), \tag{3.35}$$

$$a_2(z) = -ia_0\sin(gz) = -ia_0\sin\left(\frac{n_s - n_{as}}{\lambda}z\right). \tag{3.36}$$

If a 50/50 splitting ratio is desired, the length L of the waveguide must be fine-tuned to fulfill the following condition,

$$\frac{n_s - n_{as}}{\lambda}L = \frac{\pi}{4}. \tag{3.37}$$

Two narrow waveguides placed close to each other thus function as a passive, albeit strongly frequency-dependent, beam splitter. Fig. 3.6 shows the wavelength dependency of a passive directional coupler made on GaAs. However, where programmable and reconfigurable circuits are desired, the beam splitter can be made variable utilizing the strategies described in section 3.2. Strategies for doing this can be by locally changing the material refractive index or actuating the distance between the waveguides, both of which will change the coupling strength g. In the case of entirely symmetric waveguides, complete power transfer between the two waveguides is possible. This is not, however, the case when the waveguides are not identical. The coupled mode equations are optical analogies to the classical theory of coupled pendulums or the quantum mechanical theory of Rabi oscillations, both of which also only allow complete power transfer in case of resonance [130].

Asymmetric directional couplers

The derivation of the behavior of asymmetric beam splitters is significantly more complex than the similar derivation for symmetric beam splitters, and is outside of the scope of this thesis. The following derivations lean strongly upon the results obtained in [131]. This added complexity lies in the fact that as the two waveguides are not identical anymore, and as a result, their modes are not orthogonal, introducing a residual field

$$\mathbf{E}_{tot}(x,y,z) = a_1(z)\mathbf{E}_{y,1}(x,y,z) + a_2(z)\mathbf{E}_{y,2}(x,y,z) + \mathbf{E}_r(x,y,z). \tag{3.38}$$

Nonetheless, assuming two parallel lossless waveguides with initial amplitudes $a_1(0) = 0$ and $a_2(0) = a_0$, the following expression for the z-dependence of the power in the waveguides can be found.

$$a_1(z) = a_0\frac{ig_{12}}{\psi}\sin(\psi z)e^{i\phi z}, \tag{3.39}$$

$$a_2(z) = a_0\left[\cos(\psi z) + \frac{i\Delta}{\psi}\sin(\psi z)\right]e^{i\phi z}. \tag{3.40}$$

Here

$$\phi = [\gamma^{(1)} + \gamma^{(2)}]/2, \quad \Delta = [\gamma^{(2)} - \gamma^{(1)}]/2, \quad \psi = \sqrt{\Delta^2 + g_{12}g_{21}}, \tag{3.41}$$

where $\gamma^{(1/2)}$ are the propagation constants $\gamma^{(1/2)} = \beta^{1/2} + \theta_{1/2}$ with $\theta_{1/2}$ as an intricate perturbation to the propagation constant, which is different for the two waveguides,

$$\theta_p = \frac{\tilde{g}_{pp} - C_{pq}\tilde{g}_{qp} + C_{pq}C_{qp}\left(\beta_p - \beta_q\right)}{1 - C_{pq}C_{pq}}, \quad \text{where } p,g = 1,2,\ p \neq q. \tag{3.42}$$

The coefficients C_{12} and C_{21} are the overlap integrals between the two modes, carried out in all space and normalized so that $C_{11} = C_{22} = 1$. When considering only TE modes,

$$C_{pq} = \frac{2\beta}{\omega\mu_0}\int_{-\infty}^{\infty} E_{y,p}E_{y,q}\mathrm{d}y, \quad \text{where } p,g = 1,2. \tag{3.43}$$

The propagation constant corrections $\tilde{g}_{11/22}$ and coupling constant corrections $\tilde{g}_{12/21}$ are, still in the case of TE modes only,

$$\tilde{g}_{pq} = \omega\varepsilon_0(n_2^1 - n_1^2)\int_{wg\,\text{not}\,p} [E_{y,q}E_{y,p}]\,\mathrm{d}y. \tag{3.44}$$

$\tilde{g}_{pq}$ can thus be understood as the product of the y-components of E_p and E_q, integrated over the area of the waveguide *that is not p*. As two waveguides of varying widths will have different electric fields inside the waveguides, as well as different boundaries to integrate over, the inequalities $\tilde{g}_{12} \neq \tilde{g}_{21}$ and $\tilde{g}_{11} \neq \tilde{g}_{22}$ cause the complex behavior of asymmetric directional couplers. The coupling constants between the two waveguides are then, finally,

$$g_{pq} = \frac{\tilde{g}_{pq} + C_{qp}\left[\beta_p - \beta_q - \tilde{g}_{qq}\right]}{1 - C_{pq}C_{qp}}, \quad \text{where } p,g = 1,2,\ p \neq q. \tag{3.45}$$

For a lossless waveguide guiding a single TE mode, the time-averaged power flow in the z-direction is given by

$$\begin{aligned} P_t =& \frac{1}{4}\left[|a_1(z)|^2 + |a_2(z)|^2 + (C_{12} + C_{21})\mathrm{Re}(a_1(z)a_2(z)^*)\right] \\ &+ \frac{1}{2}\hat{z}\int\int_{-\infty}^{\infty} \mathrm{Re}(\mathbf{E}_r \times \mathbf{H}_r^*)\,\mathrm{dx}\,\mathrm{dy}. \end{aligned} \tag{3.46}$$

Inserting the expressions for a_1 and a_2 obtained in equation (3.40) into equation (3.46), while defining the last term of equation (3.40) to be $P_r(z)$, the following expression for the power can be found,

$$P(z) = \frac{1}{4}|V_0|^2\left[1 + \frac{g_{12}}{\psi^2}\sin^2(\psi z)\Big(g_{12} - g_{21} + \Delta(C_{12} + C_{21})\Big)\right] + P_r(z). \tag{3.47}$$

This equation demonstrates several properties of a set of asymmetric coupled waveguides. First, as a lossless waveguide requires that the power, $P(z)$, is constant, it is required to have a proportion of the power located in the residual fields, the exact proportion of which has a sinusoidal component in order to offset the sinusoidal z-dependence of the second term. With both Δ and $g_{12} - g_{21}$ increasing as the waveguides become more asymmetric, a larger proportion of the power will be in the oscillating residual field the more asymmetric the waveguide.

For an identical set of waveguides, $g_{12} = g_{21}$ and $\Delta = 0$, leading to

$$P(z) = \frac{1}{4}|V_0|^2 + P_r(z), \tag{3.48}$$

from which it can be inferred that $P_r(z)$ for a set of identical waveguides is constant, and can be considered a background electric field. In the case of two identical waveguides, the following will hold: $\beta_1 = \beta_2 = \beta$, $C_{12} = C_{21} = C$, $\tilde{g}_{22} = \tilde{g}_{11} = \tilde{g}_{\text{wg}}$ and $\tilde{g}_{12} = \tilde{g}_{21} = \tilde{g}_c$, leading to the following simplifications:

$$g = \frac{\tilde{g}_c + C\tilde{g}_{\text{wg}}}{1 - C^2}, \quad \theta = \frac{\tilde{g}_{\text{wg}} - C\tilde{g}_c}{1 - C^2}. \tag{3.49}$$

The other shorthand notation will simplify to

$$\phi = \gamma, \quad \Delta = 0 \rightarrow \psi = g. \tag{3.50}$$

Leaving the expression for the z-dependence of the power in the waveguides to be

$$a_1(z) = a_0 i \sin(\gamma z) e^{i(\beta+\theta)z}, \tag{3.51}$$

$$a_2(z) = a_0 \cos(\gamma z) e^{i(\beta+\theta)z}. \tag{3.52}$$

This recovers the results obtained in equation (3.36), albeit with a phase factor due to different choices when defining the initial field.

3.3.3 Slot waveguide phase shifters

In this section, the working mechanisms of a phase shifter used to operate the MZI are laid out. For a waveguide section with length L, the accumulated phase ϕ_0 of a mode with wavelength λ and effective refractive index n_{eff} is

$$\phi_0 = \frac{2\pi n_{\text{eff}} L}{\lambda}. \tag{3.53}$$

Here ϕ_0 is the accumulated phase over the length of the waveguide, n_{eff} is the effective index of the guided mode which here is assumed to be constant over the length of the waveguide, L is the length of the waveguide and λ is the wavelength. If a waveguide can be designed so that the effective mode index can be modulated, a modified accumulated phase can be described

$$\phi_m = \int_{z=0}^{z=L} \frac{2\pi n(z)}{\lambda} dz. \tag{3.54}$$

This gives a phase shift of

$$\Delta\phi = \phi_m - \phi_0. \tag{3.55}$$

Standard waveguide theory teaches that guided modes are located in materials with a higher effective refractive index than the surroundings. Slot waveguides, however, consist of two narrow high-index beams with the majority of the electric field of the

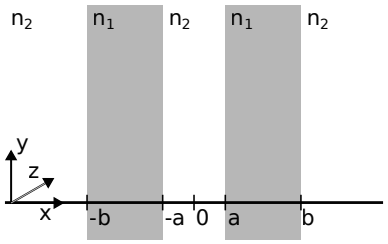

Figure 3.7: Illustration of an infinite slab slot waveguide

guided mode located in the narrow low-index gap between them [54]. Starting with the Helmholtz equation for the field in the x-direction,

$$\frac{\partial^2 E_x}{\partial x^2} + \left[k_0^2 n^2(x) - \beta^2\right] E_x = 0,$$

where $\beta = k_0 n_{\text{eff}}$ and $k_0 = \frac{2\pi}{\lambda}$, a system is defined that consists of two identical high index slabs lying in the x-plane with material refractive index n_1, each with width $w = b - a$, placed at a distance $d = 2a$ and surrounded by material with effective refractive index n_2, as can be seen in Fig. 3.7. This gives the following distribution of the refractive indices [132],

$$n(x) = \begin{cases} n_2, & |x| < a, \\ n_1, & a < |x| < b, \\ n_2, & |x| > b. \end{cases}$$

Writing out the Helmholtz equation for the three segments and defining $\gamma_2^2 = \beta^2 - k_0^2 n_2^2$ and $\gamma_1^2 = k_0^2 n_1^2 - \beta^2$, the following generalized field can be found for the fundamental TM mode:

$$E(x) = \begin{cases} A_1 e^{-\gamma_2 a} \cosh(\gamma_2 x) & |x| < a, \\ A_2 \cos(\gamma_1 |x|) + B_1 \sin(\gamma_1 |x|) & a < |x| < b, \\ A_3 \mathrm{e}^{-\gamma_2 (|x| - b)}, & |x| > b. \end{cases}$$

The boundary conditions of the fundamental TM mode are

$$n_2^2 E_{x,2} = n_1^2 E_{x,1}, \quad \frac{\partial E}{\partial x} \text{ is continuous.} \tag{3.56}$$

The four continuity equations can be found by evaluating the electric fields and their derivatives across the boundaries at $x = a$ and $x = b$. By eliminating A_1, A_2, B_1 and A_3 in the four equations, the transcendental equation for the allowed values for β can be found,

$$\tan\left(\gamma_1 (b-a)\right) = \frac{\frac{\gamma_1 n_2^2}{\gamma_2 n_1^2}\left(\coth\left(\gamma_2 a\right) + 1\right)}{\coth\left(\gamma_2 a\right) \frac{n_2^4 \gamma_1^2}{n_1^4 \gamma_2^2} - 1}. \tag{3.57}$$

This complex transcendental equation can be solved for the values of γ_1 and γ_2 that fulfill the requirements, from which the effective refractive indices of guided modes

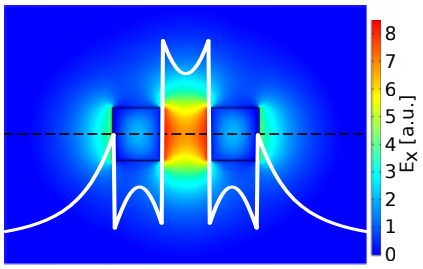

Figure 3.8: Electric field distribution of x-component of the pseudo-TE field in a slot waveguide. White line shows value of x-component of field along the black dashed line.

can be found. Fig. 3.8 shows the mode of a slot waveguide made of GaAs ($n = 3.45$) surrounded by air ($n = 1$), with a height $h = 160\,\text{nm}$, a cantilever width $w = 150\,\text{nm}$, and a slot width $g = 150\,\text{nm}$. Due to the discontinuity of the electric field of the TM mode in the cantilever, a large part of the electric field is stored between the two cantilevers in a quasi-TE mode. The effective refractive index is highly dependent on the width of the slot gap, thus making it an optimal platform for mechanically actuated phase shifters.

3.4 Summary and connection

The purpose of this chapter was to introduce the concept of programmable integrated photonics by discussing commonly used reconfigurable elements in integrated photonics and common strategies for programmable photonics.

Due to its compatibility with photons at 930 nm on the GaAs platform at cryogenic temperatures, mechanical actuation was identified as the ideal modulation strategy, compared to thermo-optic modulation, which suffers from low index changes at cryogenic conditions, and electro-optics (Pockels) modulation, which induces a large electroabsorption due to the Franz-Keldysh effect. Furthermore, NOEMS enables the development of compact devices, improving scalability.

While many reconfigurable photonic elements exist, the programmable phase shifter constitutes an essential element. Combined with passive beam splitters, complete control over the photon state can be obtained with phase shifters as the only active element. By combining two programmable phase shifters and two passive beam splitters, a unitary gate offering complete control over a single photon state can be realized. Suspended slot waveguides guide a mode contained in the gap between two narrow cantilevers. As the accumulated phase depends linearly on the effective refractive index (n_{eff}) of a guided mode, the strong gap dependence of the (n_{eff}) of a beam splitter can be exploited to make very compact phase shifters controllable via electromechanical actuation. The next chapter will cover the design of such a phase shifter, with the phase shifter parameters being guided by finite element simulations carried out in COMSOL .

Chapter 4

Design of a Slot Mode Phaseshifter

4.1 Introduction

In chapter 2, integrated photonics was introduced as a promising platform for photonic quantum computing. In chapter 3, an in-depth presentation of various strategies for on-chip actuating and controlling light in waveguides was presented. To achieve compatibility with the utilized gallium arsenide (GaAs) platform containing high-performance solid-state quantum emitters based on indium arsenide (InAs), a nano-opto-electro-mechanical system (NOEMS) phase shifter utilizing a slot waveguide was adopted. In this chapter, the optical and electromechanical properties of such phase shifters are thoroughly analyzed and described, supported by simulations performed using COMSOL. Components such as the slot waveguides and metal actuation electrodes are presented, and design considerations are described.

4.2 The slot waveguide device

As mentioned in chapter 3, the effective refractive index of a slot waveguide is strongly dependent on the gap between the slot waveguide cantilevers. An early realization of silicon slot waveguide phase shifters obtained a $2/9\pi$ phase shift for a cascaded structure consisting of three 5.8 µm long suspended slot waveguides at an applied voltage of 13 V [133]. Other implementations have been carried out on platforms such as silicon nitride, where a 210 µm long slot waveguide device observed a phase shift of π at an applied potential of 4.5 V, with a phase shift as high as 13.3π at 17 V [31].

The design of NOEMS devices is a complicated procedure that demands careful consideration. It is evident that the concept of scalability calls for devices to be as small as possible to enable tighter packing. However, this demand for scalability must be balanced with opposing requirements such as fabrication tolerance, sturdiness of devices, and the ability to achieve adiabatic and lossless coupling between modes. For many applications, the actuation speed of a device serves as an important figure of merit. The lower limit of the switching time is determined by the first mechanical resonance frequency f [134], which for a long, thin beam with mechanical spring constant k and mass m is

$$f = \frac{1}{2\pi}\sqrt{\frac{k}{m}}, \tag{4.1}$$

where the mechanical spring constant of a thin rectangular beam with a square cross-section ($w = h$) is given by

$$k = \frac{3EI}{L^3} = \frac{Ew^4}{4L^3}, \tag{4.2}$$

where E is the elastic modulus of the material, L is the length of the beam, and $I = \frac{w^4}{12}$ is the second moment of area of a filled square centered around the axis of interest [135]. Inserting the mass $m = \rho L w^2$ and Eq. 4.2 into Eq. 4.1 yields

$$f = \frac{1}{2\pi}\sqrt{\frac{Ew^2}{4L^4\rho}} = \frac{1}{4\pi}\frac{w}{L^2}\sqrt{\frac{E}{\rho}}. \tag{4.3}$$

Eq. 4.3 indicates that when optimizing for actuation speed, short thick devices are ideal, while the resonance frequency of a beam with a set shape is inversely proportional to the scaling factor when its size is scaled up and down. Optimally, the material platform is stiff and lightweight. While only considering one material platform, both scalability and response speed favor making devices as small as possible. Other aspects, however, favor larger devices. Since the phase shift is proportional to the length of the device, $\Delta\phi \propto \Delta n L$, a longer device offers a larger phase shift for the same Δn. Additionally, since p-i-n membranes are prone to break down at higher voltages, flexible devices that easily deform in response to applied electric fields allow for larger phase shifts without risking breakdowns. However, longer, more flexible devices are also prone to fabrication failure, such as the collapse of the two cantilevers of the slot waveguide after release. Short, stiff devices with large gaps have higher yields, but lower induced phase shift. Narrow devices are more vulnerable to scattering loss induced by the surface roughness introduced during fabrication.

The design of a NOEMS device thus involves balancing the different requirements to achieve optimal performance. Understanding these aspects requires a comprehensive understanding of the optical, electrical, and mechanical properties of the device.

4.2.1 Optical displacement simulations

This section covers the COMSOL simulations of the gap-dependence of the effective refractive index and how this is influenced by the wavelength of light. The gap dependence of the slot waveguide mode is simulated and a function approximating the behavior of the effective mode is introduced. Utilizing this function, additional simulations are carried out while varying parameters such as the wavelength of the light, and the gap and width of the slot waveguide cantilevers. From these simulations, the displacement needed to obtain a desired phase shift from a given slot waveguide geometry is derived, which in turn is used to guide the design of the slot waveguide device.

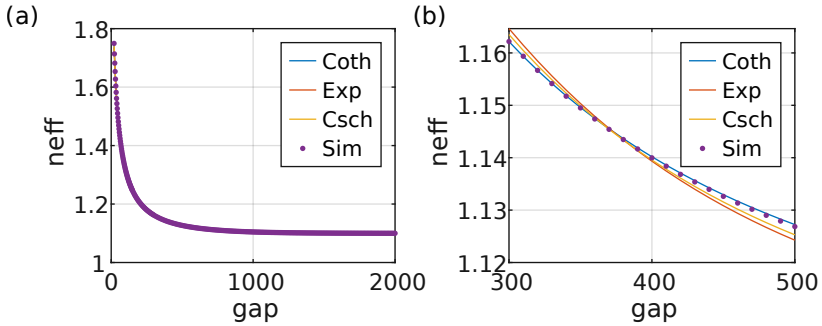

Figure 4.1: a: Gap-dependent effective refractive index of mode in a $n = 3.45$, $\lambda = 940\,\text{nm}$, $w = 150\,\text{nm}$, $h = 160\,\text{nm}$, compared to different fit models. b: Close up showing behavior of the different fits

Gap-dependent behavior of the slot waveguide mode

Precisely modeling the dependence of the phase shift on the applied voltage requires an understanding of the gap dependence of the effective mode in a slot waveguide, which here is obtained with a heuristic approach. A single simulation using a finely meshed slot waveguide ($n = 3.45$, $\lambda = 940\,\text{nm}$, $w = 150\,\text{nm}$, $h = 160\,\text{nm}$) was carried out in COMSOL 5.5 for a wide range of gap values. The results were fit to three models - a double exponential, a hyperbolic cotangent and a hyperbolic cosecant - respectively given by

$$\begin{aligned} n_{\text{exp}}(g) &= a_{\text{exp}} \cdot \exp(-b_{\text{exp}} \cdot g) + c_{\text{exp}} \cdot \exp(-d_{exp} \cdot g) + e_{exp}, \\ n_{\text{coth}}(g) &= a_{\text{coth}} \cdot \coth(b_{\text{coth}} \cdot g + c_{\text{coth}}) + d_{\text{coth}}, \\ n_{\text{csch}}(g) &= a_{\text{csch}} \cdot \operatorname{csch}(b_{\text{csch}} \cdot g + c_{\text{csch}}) + d_{\text{csch}}. \end{aligned} \tag{4.4}$$

These functions were chosen from a phenomenological approach, as the function describing the electric field distribution in a slot waveguide exhibits both double exponential and hyperbolic geometrical components [132]. Furthermore, the behavior of the gap dependence of the effective mode in a slot waveguide was visually identified as resembling the behavior of a decaying double exponential, a hyperbolic cotangent and a hyperbolic cosecant.

The following fits were obtained:

$$\begin{aligned} n_{\text{exp}}(g) &= 0.654 \cdot \exp(-0.0284\,\text{nm}^{-1} \cdot g) + 0.292 \cdot \exp(-5.13 \cdot 10^{-3}\,\text{nm}^{-1} \cdot g) + 1.102, \\ n_{\text{coth}}(g) &= 0.0476 \cdot \coth(1.40 \cdot 10^{-3}\,\text{nm}^{-1} \cdot g + 0.0408) + 1.0516, \\ n_{\text{csch}}(g) &= 0.126 \cdot \operatorname{csch}(4.50 \cdot 10^{-3}\,\text{nm}^{-1} \cdot g + 0.1022) + 1.101. \end{aligned} \tag{4.5}$$

The RMSE (root-mean-square error) for the three models was found to be respectively $\text{rmse}_{\text{exp}} = 2.4 \cdot 10^{-3}$, $\text{rmse}_{\text{coth}} = 5.75 \cdot 10^{-4}$, $\text{rmse}_{\text{csch}} = 1.4 \cdot 10^{-3}$, where the hyperbolic cotangent (coth) model has the lowest value by a factor of 4. The choice of the hyperbolic cotangent can be further justified by visually inspecting 4.1(b), where the coth fit follows the data much more precisely than the other two models.

A further demonstration can be done by comparing the value the model reaches as the gap approaches infinity, related to the effective refractive index of the actual

	Single beam	Double exp.	Hyperbolic cosecant	Hyperbolic cotangent
n_{eff}	1.100	1.1018	1.1011	1.0992

Table 4.1: Comparison of effective refractive indices for the mode in respectively a single cantilever with $n = 3.45$, $\lambda = 940\,\text{nm}$, $w = 150\,\text{nm}$, $h = 160\,\text{nm}$, and the three models using parameters in Eq. 4.5 for $g \to \infty$.

mode in a single cantilever. Since a single 150 nm wide cantilever still guides the mode, although very weakly, the effective refractive index obtained in the model as $g \to \infty$ should be equal to n_{eff} of the mode in a single cantilever waveguide. Table 4.1 shows a comparison of the effective mode at infinite gap for the three different models, alongside the effective mode of a single cantilever waveguide. As the model utilizing the hyperbolic cotangent yields the result closest to the single cantilever, it is further verified to be the optimal model of the three.

Gap-dependent phase shift in a slot waveguide

With the hyperbolic cotangent being identified as the optimal model, the simulations of the gap dependence of effective refractive index in the slot waveguides can be initialized. A simulation is built in COMSOL (version 5.5) using the Wave Optics Module. Two rectangles, with height $h = 160\,\text{nm}$, refractive index $n = 3.45$, and varying width w were centered in the 2D simulation geometry. Simulations were carried out for cantilevers with equal width as well as configurations where one cantilever has width w and the other $w + dw$. In order to prevent reflections of the electric field, a set of Perfectly Matched Layers (PML) was utilized at the boundaries. Fig. 4.2 shows the wavelength and gap dependence of the effective refractive index, n_{eff}, of the slot waveguide with different cantilever widths. While intuition might suggest that a narrower cantilever might be optimal, as a narrow cantilever leads to a larger part of the mode being located in the slot between the cantilevers, the results in Fig. 4.2 show that it is not necessarily the case, at least not for the investigated gaps. However, the results in Fig. 4.2 show that it is not necessarily the case, at least not for the investigated gaps. With widths equal to $w = 150\,\text{nm}$ and $w = 170\,\text{nm}$ identified as having the largest variation of the effective refractive index, an investigation into the phase shift can be carried out next.

Fig. 4.3 shows the wavelength- and displacement-dependence on the phase shift taking place in a 10 µm-long slot waveguide with an initial gap $g = 150\,\text{nm}$, assuming a uniform displacement over the whole waveguide. Negative values for the displacement mean the cantilevers are moved closer to each other, while a positive displacement signifies them being moved apart. As expected, the accumulated phase shift does not respond symmetrically to the same negative and positive displacements. Specifically, for a given wavelength, a larger positive displacement is required to achieve the same phase shift as with a negative displacement indicated by the white contour lines in Figs. 4.3 and 4.4. It can be seen that while the effective refractive index is highly wavelength-dependent, as seen in Fig. 4.2, the accumulated phase is less so. This discrepancy is due to the accumulated phase having an explicit wavelength-dependency,

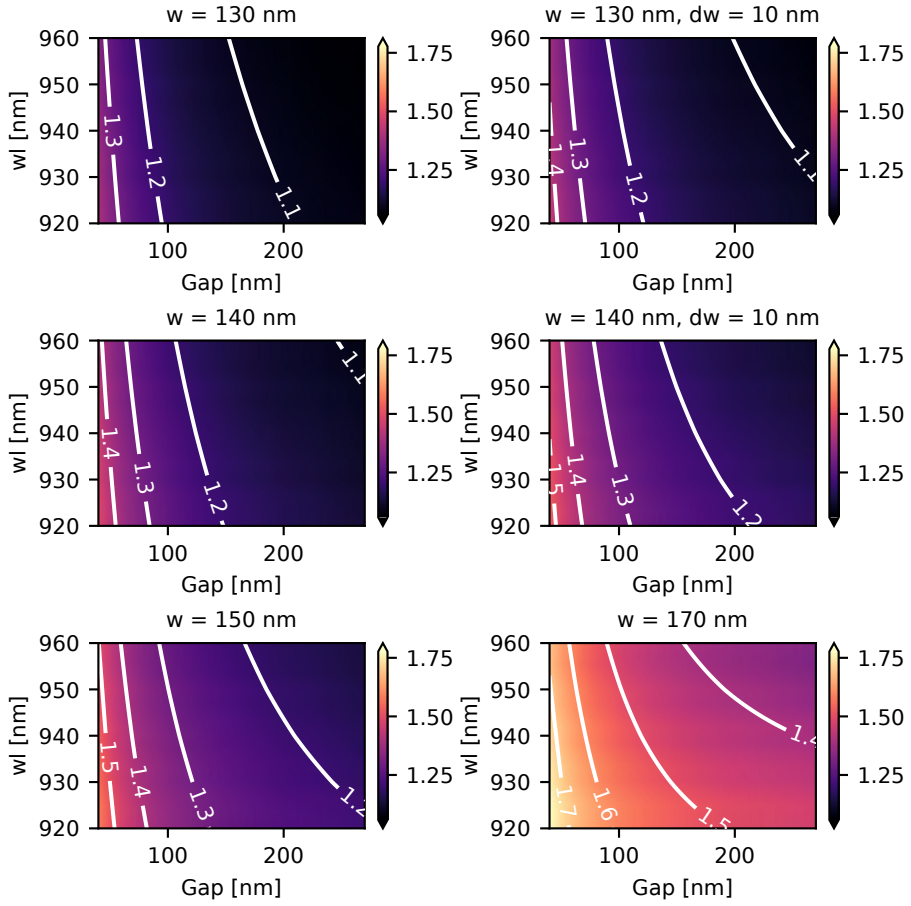

Figure 4.2: Wavelength- and gap-dependent effective refractive index of a GaAs slot waveguide. The white contours represent the wavelength and gap corresponding to a particular n_{eff}. For the waveguides with uneven width (dw $\neq$ 0), one cantilever had width w, and one has w + dw.

$\phi(wl) \sim \frac{1}{\lambda}$.

Fig. 4.4 shows the phase shift as a function of the initial gap and corresponding displacements, for the fixed wavelength of $\lambda = 940\,\text{nm}$. The shift in accumulated phase exhibits a strong dependency on the initial gap due to the very strong nonlinearity of the gap dependence of the n_{eff} over the examined gap values. The smaller the initial gap, the larger the phase shift. However, note that a large initial gap leads to decreased fabrication complexity and higher yield.

Assuming an initial width of w = 150 nm, as can be seen to be optimal in Fig. 4.3, and a wavelength of 940 nm, the negative displacements necessary to obtain benchmark phase shifts can be calculated, as seen in Table 4.2. Under optimal conditions, a phase shift of π is required to move the interference of an MZI from one extremum to the other. However, since the phase difference between the two arms of the MZI depends on the wavelength, a phase shift of 2π is needed to ensure that both extrema are reachable for a broadband wavelength interval. If it is desired to carry out a full 2π actuation from minimum to minimum, the actuator must be able to carry out a phase

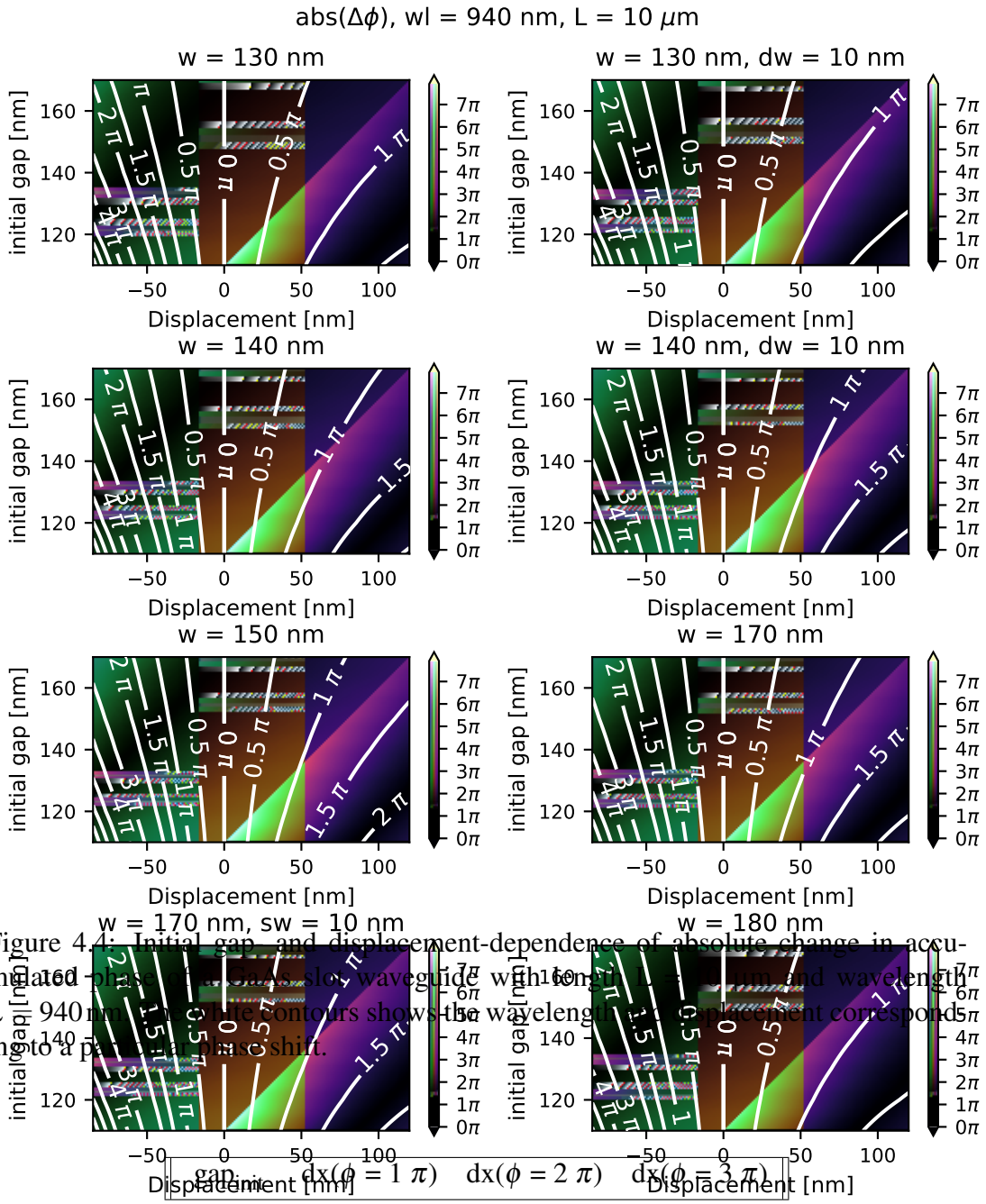

Figure 4.4: Initial gap- and displacement-dependence of absolute change in accumulated phase of a GaAs slot waveguide with length $L = 10\,\mu m$ and wavelength $\lambda = 940\,nm$. Isophase contours shows the wavelength-displacement corresponding to a particular phase shift.

gap	$dx(\phi = 1\,\pi)$	$dx(\phi = 2\,\pi)$	$dx(\phi = 3\,\pi)$
110 nm	-23 nm	-39 nm	-52 nm
120 nm	-26 nm	-44 nm	-58 nm
130 nm	-29 nm	-49 nm	-64 nm
140 nm	-32 nm	-55 nm	-71 nm
150 nm	-36 nm	-60 nm	-77 nm
160 nm	-40 nm	-66 nm	-84 nm
170 nm	-44 nm	-71 nm	-85 nm

Table 4.2: Displacements needed to obtain benchmark phase shifts for slot waveguides with a series of initial gaps, for a GaAs ($n = 3.45$) slot waveguide in air ($n = 1$), with a width $w = 150\,nm$, height $h = 160\,nm$, length $L = 10\,\mu m$ and wavelength $\lambda = 940\,nm$.

shift of 3π.

Owing to the nonlinearity of $n_{\text{eff}}(g)$, $\mathrm{d}x_{3\pi}$ is significantly smaller than $3\mathrm{d}x_{\pi}$. In addition, whereas the displacement needed to obtain π phase shift is 1.91 times larger with an initial gap $g_0 = 170\,\text{nm}$ than with an initial gap $g_0 = 110\,\text{nm}$,

$$\mathrm{d}x_{\pi}(\mathrm{g}_0 = 170) = 1.91\mathrm{d}x_{\pi}(\mathrm{g}_0 = 110), \tag{4.6}$$

the displacement needed to obtain 3π phase shift is only 1.63 times larger for an initial gap $g_0 = 170\,\text{nm}$ than with an initial gap $g_0 = 110\,\text{nm}$,

$$\mathrm{d}x_{3\pi}(\mathrm{g}_0 = 170) = 1.63\mathrm{d}x_{3\pi}(\mathrm{g}_0 = 110). \tag{4.7}$$

For the investigated parameters, the dependence of the initial gap on the displacement needed to reach a 3π phase shift is weaker than the dependence required for π phase shift. In order to finalize the design, a simulation of the forces necessary to induce a certain positive or negative displacement of the slot waveguide is thus needed.

4.2.2 Actuation mechanism

Nano-opto-electro-mechanical Systems (NOEMS) are an extension of micro-electro-mechanical systems (MEMS). In NOEMS and MEMS, electrostatic or electrodynamic fields induce displacement of moving parts. These micro- and nano-scale moving parts are fragile and prone to failure. Due to the small sizes and extreme aspect ratios involved, care must be taken when designing, fabricating, and actuating the device.

NOEMS devices are particularly sensitive to both electrostatic discharges (ESD) and electric overstress (EOS). Furthermore, if two cantilevers with opposing charges come into physical contact with each other, the devices can permanently fuse due to the van der Waals forces, destroying the device. Therefore, an investigation of the actuation range for different designs is needed.

The simplest configuration for displacement of a MEMS cantilever consists of two simple metallic cantilevers placed close to each other with an initial distance x_0, one, called the stator, fixed in position and the other one, called the motor, placed on a

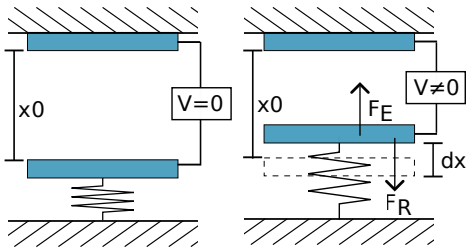

Figure 4.5: Left: A parallel plate capacitor where one plate (the stator) is fixed, while the other (the motor) is attached to a spring. The initial distance between the plates is x_0, and no electric field is applied initially. (V=0). Right: When a voltage is applied, an electric field is created between the plates, which exerts a force (F_E) on the motor, casing it to shift dx.

spring with spring constant k. When an electrostatic potential V is applied across them, the Coulomb force will induce a displacement dx pulling them towards each other, as can be seen in Fig. 4.5. Typically, these are approximated as parallel plate capacitors with an area A. The total potential energy in the system can be written as

$$E = \frac{1}{2}\frac{\varepsilon A}{x_0 - dx}V^2 + \frac{1}{2}k\,dx^2, \tag{4.8}$$

where the first term is the electrostatic potential and the second term is the spring energy [136].

At equilibrium, the electrostatic force F_E and the restoring mechanical force F_r will cancel out, giving

$$\begin{aligned} F = -\frac{\partial E}{\partial (dx)} = \frac{1}{2}\frac{\varepsilon A}{(x_0 - dx_{\mathrm{eq}})^2}V^2 - k dx_{\mathrm{eq}} = 0, \\ \rightarrow \frac{1}{2}\frac{\varepsilon A}{(x_0 - dx_{\mathrm{eq}})^2}V^2 = k dx_{\mathrm{eq}}. \end{aligned} \tag{4.9}$$

This is an unstable system as the restoring force scales linearly with the distance, but the displacing force scales faster than linear. It can be shown that there is a given pull-in voltage, V_p for which there is no stable solution, and the plates will be pulled into each other. While V_p depends on the exact configuration such as the spring constant and initial distance, it can be shown that the pull-in distance $\mathrm{d}x_p$ is always $x_0/3$ in the case of an idealized parallel plate capacitor. Any MEMS systems, with a linear restoring force and a displacing force that scales as an inverse power law,

$$F \propto \frac{1}{(x_0 - \mathrm{d}x)^n}, \tag{4.10}$$

are similarly unstable, and will collapse for displacements above $x_0/(n+1)$. In previous works done by this group, typical widths of the metal beam are $\sim 100\,\mathrm{nm}$, while typical heights are $\sim 160\,\mathrm{nm}$. In the opposite limiting case, where the cantilever is much wider than tall, the pull-in distance has been found to be $\mathrm{d}x_p = x_0/2.23$ [137].

To enable a large displacement, a comb drive was used. A comb drive is a commonly utilized electrostatic actuator in MEMS systems, where the linear capacitance-displacement relationship enables a large displacement [137]. They consist of two interwoven finger structures, one fixed (stator) and one movable (motor). As the actuation is mainly influenced by the fringing fields surrounding the fingers, the displacement of a comb drive can be much greater than the displacement of an actuator consisting of two planar beams.

4.2.3 Electromechanical simulations

Actuation of the phase shifter was carried out using electromechanical displacement. The design used can be seen in Fig. 4.6. To investigate the electro-mechanical displacement induced by the slot waveguide, electromechanical simulations were carried out in COMSOL using the MEMS package. The geometry for the COMSOL simulations is built by saving the relevant selection of the circuit as a DXF file, allowing the

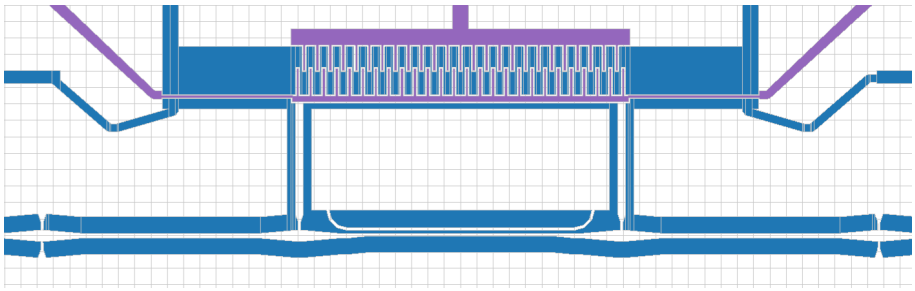

Figure 4.6: CAD design of the actuator, utilizing a design with a negative displacement and a comb drive, with a 10 µm long slot waveguide with 3.2 µm long couplers. White is GaAs substrate, purple is metal and dark blue is deep etched areas. One square equals one micron.

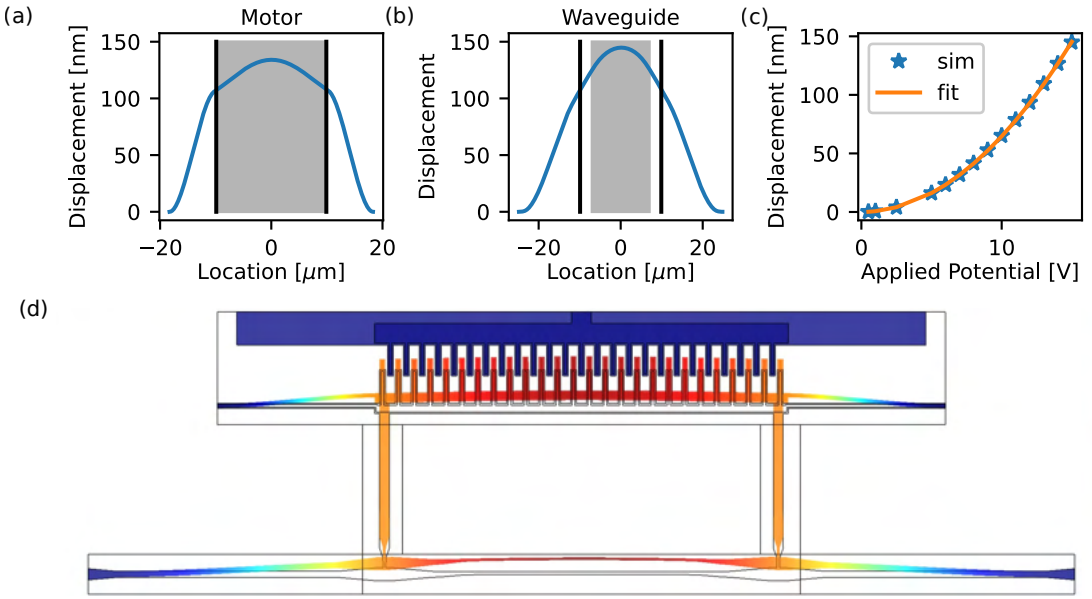

Figure 4.7: Simulation in COMSOL. a: Displacement at 15 V for the motor. b: Displacement at 15 V for the slot waveguide. c: Applied potential vs displacement. d: COMSOL plot of the displacement at 15 V (exaggerated). To minimize computational load, the inner cantilever of the slot waveguide is not included in the simulation.

geometry to be imported into COMSOL. Defining a deforming air domain around the device allows for the simulation of electrostatically induced displacement. By running an auxiliary sweep over the applied potential, the relationship between applied potential and induced displacement is investigated. The simulation of electromechanical displacement in the device utilizing the comb drive is shown on Fig. 4.7. Fig. 4.7(d) shows the distribution of the displacement. Fig. 4.7(a) shows the displacement of the motor, with the black lines showing the locations of the tethers connected to the slot waveguide cantilever, and the shaded area showing the location of the comb. Fig. 4.7(b) shows the displacement of the waveguide, with the black lines showing the locations of the tethers connecting the slot waveguide cantilever to the comb, and the

shaded area showing the location of the slot waveguide cantilever and the coupler. In Fig. 4.7(c), the displacement as a function of the applied voltage is plotted and fitted to the following function,

$$\mathrm{d}x = b \cdot V^2. \tag{4.11}$$

The b-parameter is found to be $b_{\mathrm{comb}} = 0.65\,\mathrm{nm/V^2}$. As the actuation in this design is carried out utilizing a comb drive, the limiting factor for displacement is not the MEMS pull-in effect, but the initial gap between the cantilevers. Once the cantilever has been displaced too close, the two cantilevers will fuse due to the Van-der-Waals effect, and may not be separable once the voltage is lowered again. Given an initial gap of 150 nm, this will happen once the applied potential is

$$V_{\mathrm{collapse}} = \sqrt{\frac{150\,\mathrm{nm}}{0.65\mathrm{nm/V^2}}} = 15.19\,\mathrm{V}. \tag{4.12}$$

In section 4.2.1, the displacement needed to obtain 3π phase shift for light with a wavelength $\lambda = 940\,\mathrm{nm}$ on a negative displacement slot waveguide phase shifter with a length $L = 10\,\mu\mathrm{m}$ and a cantilever width $w = 150\,\mathrm{nm}$ was found to be approximately in the range of $70 - 85\,\mathrm{nm}$. Aiming for a desired displacement in the 80-100 nm range to compensate for unforeseen fabrication imperfections, the necessary electric potential can be determined as

$$V_{80\,\mathrm{nm}} = \sqrt{\frac{80\,\mathrm{nm}}{0.65\mathrm{nm/V^2}}} = 11.1\,\mathrm{V}, \quad V_{100\,\mathrm{nm}} = \sqrt{\frac{100\,\mathrm{nm}}{0.65\mathrm{nm/V^2}}} = 12.4\,\mathrm{V}, \tag{4.13}$$

which is safely below the voltage at which the two slot waveguide cantilevers will come into contact.

4.3 Conclusion and outlook

Mechanically actuatable slot waveguides provide a promising platform for phase shifting of light in integrated photonics. Assuming an initial gap and cantilever widths both of 150 nm, a 10 µm long slot waveguide on a device utilizing a negative (inwards) displacement can obtain a phase shift of 3π with an applied potential of 11.1 V. The following chapter will cover the nanofabrication of a slot waveguide phase shifter.

Chapter 5

Nanofabrication of integrated Photonics on a GaAs platform

In this chapter, a detailed overview of the fabrication of integrated photonics on a suspended GaAs platform is given. First, the GaAs platform is introduced. Next, the nanofabrication is analyzed, the relevant steps described, and the procedure for fabricating the chip given. Following that, a description of design considerations is laid out, including minimum feature sizes and averting possible failure modes during fabrication.

5.1 Nanofabrication

When the first programmable, electronic, all-purpose general computer, the ENIAC, was built in 1945 it marked a revolution. Before the invention of digital computers, complex calculations would be carried out by human computers[i]. Whereas it would take a skilled human computer 20 hours to solve a ballistic trajectory with a mechanical calculator, or 15 minutes if also armed with a differential analyzer, the ENIAC could do it in only 30 seconds [139]. However, early computers consisted of thousands of vacuum tubes, leaving them large and cumbersome, and making troubleshooting complicated. While the components themselves became smaller and more reliable as technology advanced, the components were joined by interconnects which remained prone to failure. Furthermore, as components became smaller and more densely packed, maintenance work became more and more complex. The arrival of the electronic integrated circuit (EIC) in the late 1950s marked another revolution. By seamlessly integrating many components on one semiconductor chip, the need for unreliable interconnects was minimized. As improvements in first micro-, and then nanofabrication lowered the minimum commercially available MOSFET channel length from 20 µm in 1968 to 7 nm in 2020 [140], denser and denser packing of components was possible.

[i]Computing was considered menial labor and many human computers were women, with degrees in mathematics or physics hired in one of the few positions in technology available to them [138].

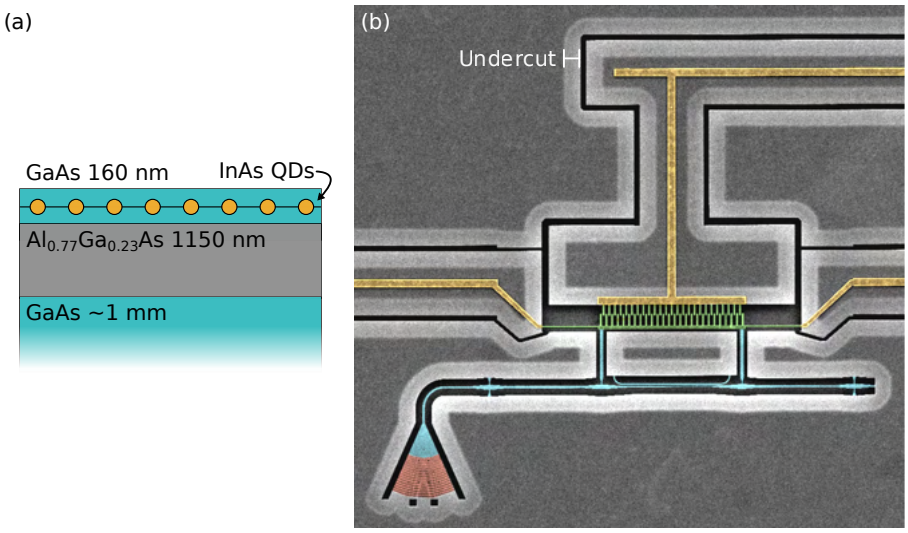

Figure 5.1: Wafer layer stack and example of device. a: Layer stack. b: SEM showing suspended device fabricated on GaAs. Highlighted components are metallical wires (gold), suspended comb drive (green), suspended nanophotonical structure (blue) and shallow-etched gratings (red).

5.1.1 The GaAs platform

The platform utilized for all measurements described in this thesis consists of the same wafer stack illustrated in Fig. 5.1. The material used is GaAs in the zincblende configuration, grown in the [001] direction. Initially, a ~ 1 mm thick substrate layer of GaAs is grown. On top of that, an 1150 nm sacrificial layer of $Al_{0.77}Ga_{0.23}As$ is grown using Molecular Beam Epitaxy (MBE). This layer, whose height is optimized to ensure optimal coupling for shallow etch gratings (SEGs) [141], can be isotropically removed by an HF etch [142], allowing for the fabrication of suspended devices. Finally, 160-nm thick GaAs membranes are defined. Embedded in the middle of these membranes are InAs quantum dots (QDs) grown by Stranski-Krastanov growth. The emission wavelength of these quantum dots is approximately $920 - 945$ nm at cryogenic temperature.

5.1.2 Fabrication procedure

The fabrication procedure utilized in this thesis consists of between three and five steps. While the exact recipe differed between different experiments, and even different versions of the same device, a general outline of the fabrication flow can be provided:

(i) Definition of metal wires, markers, electrodes and bonding paths.

(ii) Definition of shallow etched gratings for chip-to-fiber coupling.

(iii) Definition of suspended nanostructures such as waveguides, cantilevers, photonic crystals, and combs as well as isolation trenches.

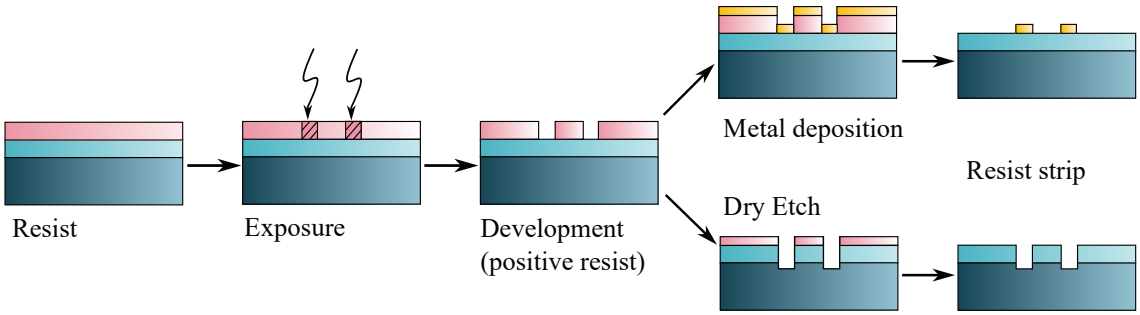

Figure 5.2: General workflow of a single EBL step. Resist is spin-coated on the sample, which is exposed and then developed.

(iv) Patterning of epoxy inverted tapers, for the devices showcased in chapter 6.

(v) Wet etch undercut and critical point drying.

Several samples utilizing the same series of procedures can be placed together on the same mask. When designing the sample, consideration is paid to the geometry of the sample holder used during fabrication. Especially if multiple wirebonds are to be carried out in a small area, the layout of the bonding pads must be placed to ensure the maximum possibility of successful bonding. The sample is designed using the Python Package SampleMaker, which is developed by the Quantum Photonics group at the University of Copenhagen.

5.1.3 Lithography

Lithography is the foundational procedure of micro- and nanofabrication, as it is the process in which a pattern is defined on the chip [143]. Initially, a thin film containing a polymer is spin-coated on the chip. This polymer, called a resist, will undergo a reaction when exposed to either UV-light, in the case of photoresist, or energetic electron beams, in the case of electron beam resist. This reaction will make the exposed area more (less) soluble in the case of a positive (negative) resist. Several mechanisms for resists exist, with examples being crosslinking of polymers, or photochemical reactions such as changes in the pH value. The resists used in the fabrication for this thesis are all polymers that, when the resist is exposed, will remove crosslinks (crosslink further) in the case of a positive (negative) resist [144]. After exposure, the sample is immersed in a liquid developer, which will remove the polymers starting with the highest-soluble areas, which are the exposed (unexposed) areas for a positive (negative) resist.

UV-lithography is widely used in the semiconductor fabrication industry. A reusable hard mask, with the desired pattern (but taking diffraction into account) is placed over the resist and aligned to the sample, after which the whole assembly is exposed at once [145]. This can create extremely precise patterns, with resolutions as low as 5 nm in the case of extreme ultraviolet lithography using wavelengths at 13.5 nm [146]. Additionally, the production speed is high as the entire mask is exposed at once. However, the need for fabricated hard masks makes this approach impractical

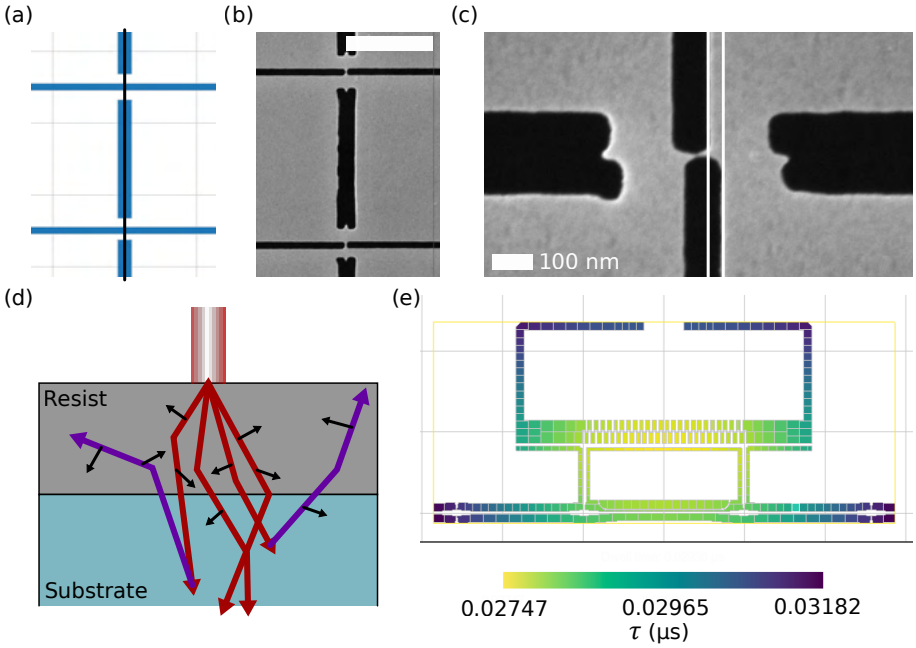

Figure 5.3: Stitching errors and proximity correction. a: Pattern used to test write field stitching error. Write field border follows the middle black line. Grid spacing is 1 μm. b: Result for pattern shown in subfigure a. White beam is 1 μm. c: Rotated version of pattern in subfigure a, showing a 31 nm displacement between two vertically separated write fields. d: Scattering of the electrons in EBL. Forward scattering (red) is relatively contained, while back-scattering (purple) leads to significant electron spreading. e: Dwell time (μs) after proximity effect correction. Calculated dwell time is 0.014 μs. Grid size is 10 μm.

for research purposes, where the exact same mask is rarely fabricated more than a few times [147]. Electron beam lithography (EBL) enables patterning of features with a resolution down to a few nanometers [148]. Direct-write EBL enables the writing of nanoscale structures without the use of a physical mask. A tightly focused electron beam is used to intricately pattern the surface of the resist. The beam, which is steered by magnetic fields in the EBL, exposes the material one "pixel" at a time, gradually scanning a pre-programmed pattern over a small area called the write field. Once the whole pattern is written on the write field, which typically is 300×300 μm or 500×500 μm, the machine will translate the sample stage, and the exposure will continue on the next writing field. As the uncertainty of the micropositioners moving the stage can be much larger than the resolution of the EBL, this can lead to stitching errors on the edges between write fields [149].

Fig. 5.3 (a-c) shows a test used to characterize the stitching error of the EBL machine. In Fig. 5.3(a), the pattern used to test is shown, with the middle of the vertical blue line placed exactly on the edge between write fields. The grid size is 1 μm. Fig. 5.3(b) shows an SEM of the resulting pattern. Fig. 5.3(c) shows the same pattern, but oriented along a horizontal write field border. The distance between the two white lines, corresponding to the horizontal displacement of the two write fields,

is 31 nm. As even small imperfections in a finalized waveguide can lead to significant scattering, it is important that fine, important features should not cross the write fields. Compared to UV lithography, EBL is optimal for research purposes. While the one-pixel-exposed-at-a-time procedure leads to low throughput, the ability to carry out mask-less fabrication is ideal for exploratory approaches. The type of lithography utilized in this thesis is EBL using positive resist, with an exception for the epoxy used for inverted taper couplers, for which a negative EpoCore resist is used. The tool employed is an Elionix ELS-F_{125}, which has an acceleration voltage $V_{acc} = 125\,\text{keV}$, a $500 \times 500\,\mu\text{m}$ write field and a 2 nm beam diameter [150].

A main limitation to the resolution of electron beam lithography is the scattering of electrons, caused by interactions with the resist (forwards scattering) or the substrate (back-scattering), as illustrated on Fig. 5.3. Furthermore, interactions between the resist and the electron beam cause energy dissipation in the form of slow secondary electrons. While forward scattering and secondary electrons typically lead to a short-range broadening of the beam, the back-scattering effect leads to long-range dissipation of the electrons. This effect, the proximity effect, is commonly modeled with a double Gaussian distribution,

$$f(r) = \frac{1}{1+\eta}\left(\frac{1}{\pi\alpha^2}\exp\left(\frac{-r^2}{\alpha^2}\right) + \frac{\eta}{\pi\beta^2}\exp\left(\frac{-r^2}{\beta^2}\right)\right), \tag{5.1}$$

where α represents the forward scattering range, β the back-scattering range, and η the relative strength between the forward scattering and back-scattering [151]. Extra precision can be obtained by adding a single exponential decay,

$$f(r) = \frac{1}{1+\eta+\nu}\left(\frac{1}{\pi\alpha^2}\exp\left(\frac{-r^2}{\alpha^2}\right) + \frac{\eta}{\pi\beta^2}\exp\left(\frac{-r^2}{\beta^2}\right) + \frac{\nu}{2\gamma}\exp\left(\frac{-r}{\gamma}\right)\right). \tag{5.2}$$

As the proximity effect scatters the energy, this means that the actual required dose for a given area of the resist is larger than the actual clearing dose, as seen in Fig. 5.3(e). The discrepancy is significantly larger for smaller, isolated features than for large, continuous features such as metal bonding pads. Furthermore, as the deep etch procedure has proven itself prone to overetching compared to the design, the mask for the deep etched design is resized with $-20\,\text{nm}$ in all directions simultaneously with running the proximity effect correction.

5.1.4 Metal deposition

Many nanofabrication recipes require depositing metal features directly on the membrane. While this can be done by depositing a layer of metal on the entire chip and etching away unwanted parts after patterning a resist mask, it is often desirable to lay out the pattern directly on the sample. This can be done using a technique called lift-off, where a uniform layer of metal is deposited on a resist mask with the desired pattern. When removing the resist, the metal deposited on top of the resist will be removed as well, leaving only the metal pattern. In this thesis, metal patterns are used

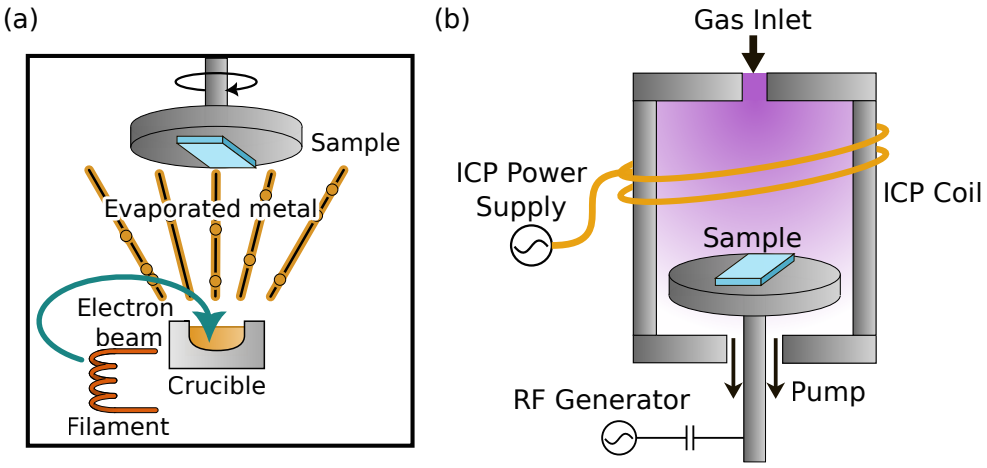

Figure 5.4: a: Schematic of metal deposition taking place in a EBPVD system. b: Schematic of ICP-RIE system.

for bonding pads, wires, and electrodes, alignment marks, and for stiffness engineering by utilizing the intrinsic stress mismatch between the GaAs substrate and the metal layer.

While there are several methods with which thin films of metal and other materials can be deposited, all nanofabrication in this thesis was carried out using electron beam physical vapor deposition (EBPVD), a schematic of which can be seen in Fig. 5.4(a). In EBPVD, which is a type of physical vapor deposition (PVD), the chip is mounted on a substrate holder, which is then placed in a chamber containing a deep vacuum. An electron gun emits a stream of electrons, which is steered into a crucible containing the desired metal [152]. As the energetic electrons evaporate the top layers of the metal, the chamber will fill up with vaporized metal gas, which will deposit on all surfaces, including the chip, which is rotated to ensure an even coat. As a machine contains several crucibles, this technique can also be used to apply several subsequent layers of metal without breaking vacuum.

In this thesis, two separate recipes are used. For bonding pads, alignment marks and electrical wires, a dual metal layer consisting of 10 nm Cr for adhesion and 160 nm Au is utilized. For stiffness engineering purposes, as well as alignment marks in the samples testing stiffness engineering, a triple layer consisting of 10 nm Cr for adhesion, 160 nm Ni chosen due to its thermal expansion coefficient mismatch compared to GaAs and 10 nm Au to prevent corrosion is deposited. Both are fabricated using a CSAR13 resist applied with spincoating at approximately 2000 RPM for 60s, yielding a 550 nm thickness. Following a room temperature development in n-amylacetate for 60s, the sample is descummed using an O_2 plasma for 45 s, after which the metal is deposited using a Polyteknik Flextura system. After that, a liftoff procedure in 1'3'Dioxolane is carried out.

Care must be taken when removing the resist during liftoff. While gentle ultrasound sonication can help detach the resist from the chip surface, if the intensity is too high or the wrong frequency is used, the deposited metal can separate from the chip surface. Examples of incomplete liftoff can be seen in Fig. 5.5(a) and (c), whereas a

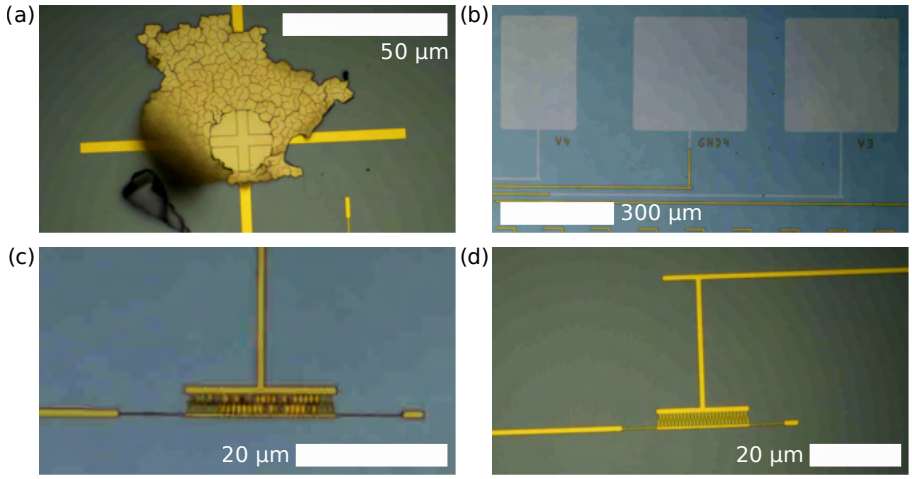

Figure 5.5: Optical micrographs of metal pads post-liftoff. a: Top layer failing to lift properly off after the second of two metal deposition steps. If metal sheet is not properly removed, it can fold into little pieces, as seen on the bottom left side of the cross marker, which can cause contamination on the chip surface. b: Large bonding pads ripped cleanly off the chip after too-vigorous sonication. c: Metal comb with incomplete liftoff in between teeth. d: Clean, high-quality lift-off, with good definition of comb drive teeth.

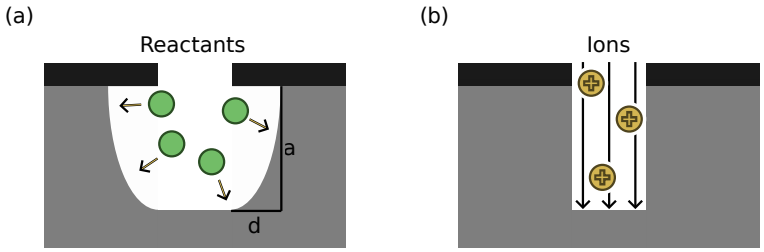

Figure 5.6: Types of etching. a: Wet etching creating an undercut with an etch anisotropy depending on the ratio of the etch depth to the undercut width. b: Dry, ion-based etching creating straight sidewalls with high anisotropy but little selectivity between the mask and substrate.

case of large bonding pads being ripped off the surface due to overly strong sonication can be seen in Fig. 5.5(b). In Fig. 5.5(d), an example of a successful liftoff is seen, with well-defined comb drive teeth, clean and even edges of wires, and no areas failing to liftoff or with undesired removal of the metal.

5.1.5 Etching

In addition to patterning metal using lift-off technologies, the fabrication of integrated nanophotonic devices requires the patterning of features such as gratings, waveguides and tethers into the substrate. Etching covers a family of techniques allowing for the controlled removal of material through processes that can be either chemical, physical or a combination of the two [152].

Dry etching

To define features such as gratings, waveguides, and tethers on the GaAs membrane, dry etching is utilized [142]. Dry etching is an etching technique involving a combination of physical and chemical processes that allows for precise control of the anisotropy and the sidewall profile [153]. By placing the chip in a vacuum chamber capable of generating a plasma, an etchant gas of choice is broken into chemically reactive species such as electrons, ions, and radicals. In physical etching, particles, typically ions, are accelerated in a strong magnetic field to a high kinetic energy. When the sample is bombarded with these highly energetic particles, the atoms lying at the top of the sample are knocked off, which gradually removes the top layer of the sample. This etching technique is highly anisotropic and can create high aspect ratio features, although care must be taken to avoid tilting the chip, which would cause the etching to be carried out at an angle. Furthermore, this process typically has low selectivity, removing resist and substrate at similar rates. Chemical etching uses chemical reactions between the gas etchant and the substrate and is mostly isotropic. As different materials react differently to the etchant, this also allows for a higher selectivity between resist and substrate.

In Reactive Ion Etching (RIE), a combination of physical and chemical processes is used. Two parallel plates are positioned at the top and the bottom of the chamber, with the top plate connected to an RF power supply used to generate the plasma, and the bottom plate grounded. The chip is placed on the bottom plate, which has a large potential difference compared to the top of the chamber, causing the charged particles dissociated by the plasma to accelerate down to the surface. While this allows for highly anisotropic processes, the same source of power is used for both plasma diffusion and ion acceleration, leading to a trade-off between the two processes.

By utilizing an inductively coupled plasma-RIE (ICP-RIE) system, this tradeoff can largely be avoided [154]. ICP-RIE utilizes a coil placed around the plasma chamber to produce the plasma, as seen in Fig. 5.4, while a second power source applies an RF bias to the sample holder, allowing for separate control of the ion acceleration. This enables greater control of selectivity, etch rate, and anisotropy, allowing for the fabrication of devices with straight sidewalls and deeply etched features. All dry etching in this thesis is carried out using an Oxford Plasmalab 100 system. A window placed on top of the ICP allows inspection of the sample with a camera microscope. In addition to white light for visual inspection during processing, the camera also measures the reflection from a laser which is shone on a sample.

Gratings in and out of the device are defined in the second design step. The utilized resist is CSAR9, with a resist thickness of approximately 220 nm following 4000 RPM spincoat for 60 s. The sample is cold developed in n-amyl-acetate at -5°C for 40 s. After this, the sample is etched using an RIE etch with BCl_3/Ar at a (5:10) ratio. Etch depth is controlled using end point detection, where the laser is focused on a square with side length 300 µm, defined during EBL. By monitoring the progression of the reflectivity, the procedure can be canceled once the desired etch depth of 90-100 nm is reached.

In the third step, where waveguides, trenches and comb fingers are patterned, a

high aspect ratio is needed. During this step, an AR 300-80 promoter is applied before the resist for better resist adhesion. After being spincoated using an arbitrary recipe and baked at 115C for 1 minute, the chip is cleaned in 1,3-dioxolane for 1 minute. Following this, ZEP520 is spun at 1750 RPM for 60 seconds and baked at 185 °C for 5 minutes. Following exposure, the chip is being cold developed at -5 °C for 60 s. Patterns are then imprinted using ICP-RIE in a $BCl_3/Cl_2/Ar$ (3:4:25) chemistry, with an etch depth of ~ 300 nm, reaching into the AlGaAs layer. The termination of the etch is determined using end point detection on the resist. Resist strip is carried out in hot (70°C) NMP for 10 min, after which exposed AlGaAs is removed with a wet etch, undercutting the features.

5.1.6 Wet etching

Wet etching, where the sample is immersed in a liquid containing etchants, is typically highly selective, meaning that it will etch away different materials with different speeds. It is typically also highly isotropic, meaning that the etchant will etch almost equally in all directions, as seen in Fig. 5.6(a). This isotropy will leave an undercut where the etchant eats away the material below the mask. While this allows for suspension of free-standing cantilevers and features as utilized in MEMS, it is undesirable for the definition of devices where vertical sidewalls are needed. Due to factors limiting the free flow of the etchant, a supposedly isotropic etch can still exhibit behavior where the vertical and horizontal etch ratios are different, as depicted by a and d in Fig. 5.6(a). The anisotropy of an etch is given by the formula

$$A = 1 - \frac{d}{a}, \tag{5.3}$$

where a perfectly anisotropic (isotropic) process has $A = 1$ ($A = 0$) [152]. Some chemical etches have different etch ratios for different crystal planes, leading to preferential etching in those directions. For example, KOH etching of silicon has a selectivity for the $[100]$ direction over the $[111]$ direction as high as 600:1, leading to a diagonal etch profile with etch planes running in the 110 direction [152].

Following the definition of features such as waveguides and comb drives by deep ICE-RIE etch, they must be suspended by removal of the sacrificial $Al_{0.77}Ga_{0.23}As$ layer underneath the GaAs layer. This is done using a 5% HF wet etch, which is highly selective to AlGaAs over GaAs, for 50 s. To remove polymer residues, which are often present after HF etching, a cleaning procedure using H_2O_2 and H_3PO_4:H_2O (5:50) for 1 minute each is carried out, with the device being cleaned in milli-Q (MQ) water between each step.

MEMS devices require highly fragile suspended parts. At nano-scale, the influence of the surface tension of the immersed liquid becomes significant, and can cause cantilevers to collapse together if air dried. Two nanobeams that come into contact will fuse in a process known as stiction. If ignored, this can reduce both yield and performance to almost zero. To avoid this, following the last chemical cleaning procedure, the MQ water used to wash away the H_3PO_4:H_2O is gradually replaced with 2-propanol (IPA). The sample is then placed in a critical point dryer (CPD) which

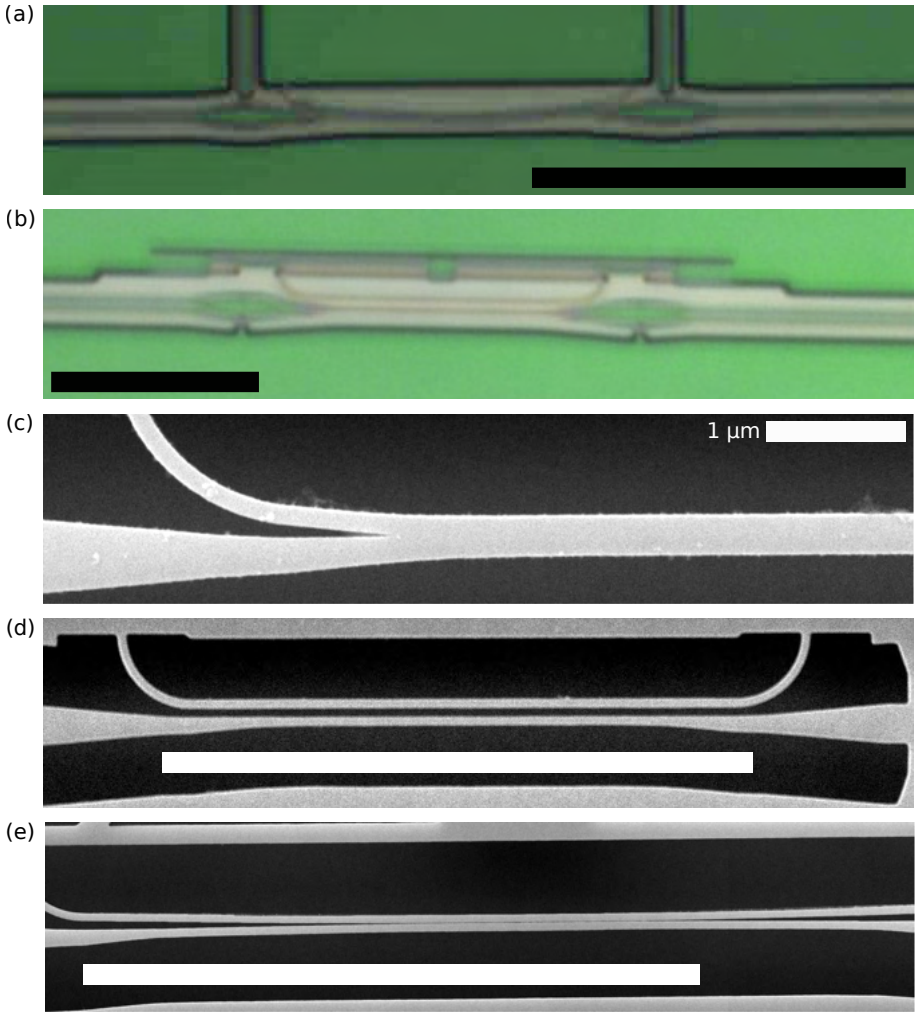

Figure 5.7: a: Post-development optical microscope image displaying resist beams that are collapsed together. b: Post-development optical microscope image displaying properly developed resist beams. c: Slot waveguide deep-etched with collapsed resist beams, giving the appearance of one continuous cantilever. d: Slot waveguide featuring properly separated cantilevers. e: Slot waveguide with cantilevers collapsed together, likely during or just after wet etching

again will gradually replace the IPA with liquid CO_2. The machine will then control the pressure and temperature such that the phase transition between the liquid and gaseous phase of CO_2 moves around the critical point rather than through a discrete phase transition [155].

5.1.7 Fabrication limitations and design considerations

The scaling-down of integrated circuits requires the fabrication of features with decreasing widths and increasingly extreme aspect ratios. Successfully fabricating these nano-scale devices requires an understanding of the limitations of every step of the fabrication process. The resist beams utilized for the slot waveguides are narrow

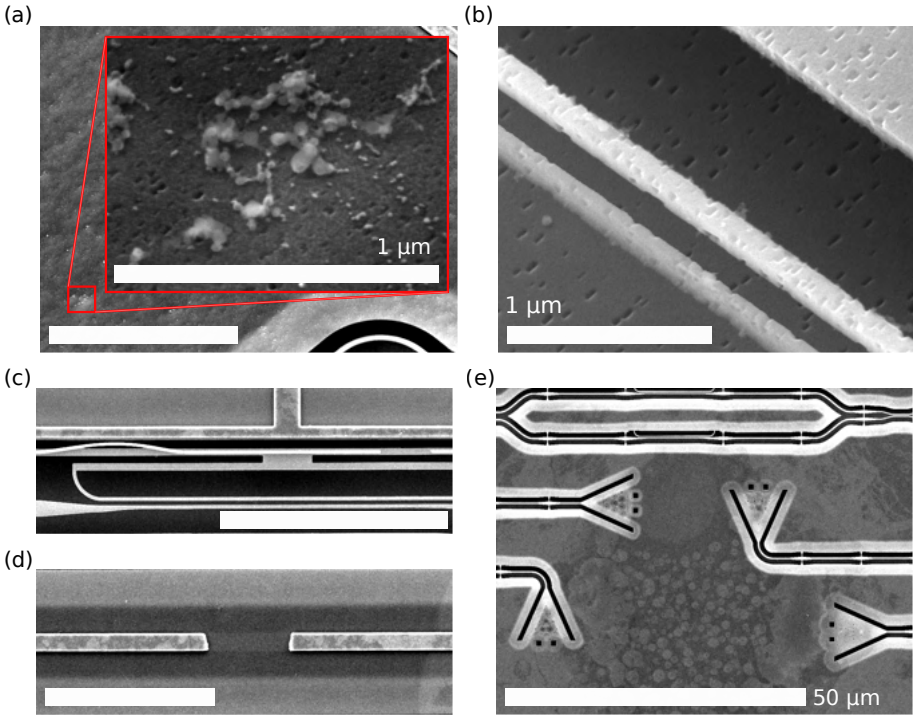

Figure 5.8: Post-fabrication SEMs of samples featuring fabrication flaws. All scale bars are 10 µm unless otherwise noted. a: Resist residue not properly removed during cleaning procedure. b: Severe damage to surface of GaAs. c: Narrow (100 nm wide) wire with warped and broken sections. d: Wide (1 µm wide) wire with broken section. e: Surface stained by unidentified residue, and SEGs failing to fully undercut.

(∼150 nm), and exhibit a ∼4:1 aspect ratio due to the 550 nm resist thickness. Additionally, the beams are placed at a very short distance, only separated by 150 nm. This leaves them fragile and prone to breakage before deep etching is carried out. In particular, this tends to happen right after development, where the chip is air-dried after the developer is removed in an IPA bath. Despite IPA having a relatively low surface tension (2.18 Pa) [156], compared to water's surface tension (7.28 Pa), the nanoscale sizes and large aspect ratios can cause the resist beams to collapse onto each other. This is seen in Fig. 5.7(a) and (c), where the two individual cantilevers of the slot waveguide have fused into one cantilever. This critical failure can be prevented by generously flushing the sample with N_2 in the direction of the cantilevers of the waveguides for 45-60 s right after development rather than letting it air-dry. Examples of well-developed resist beams and a functional slot waveguide can be seen in Fig. 5.7(b) and (d). Note that this failure mode is different from having the slot waveguides collapse due to stiction after the wet etch, as seen in Fig. 5.7(e). Visual inspection allows discernment of the two failure modes as cantilevers collapsed during or after the wet etch will visibly be two separate cantilevers touching each other.

Chip 1	Short		Chip 2	Short
Yield	21/34		Yield	33/34
Yield [%]	61%		Yield [%]	97 %

Table 5.1: Yield of devices.

5.2 Fabrication results

Fig. 5.8 shows a selection of SEM micrographs illustrating common fabrication errors when fabricating integrated photonic circuits. Resilient residues, as can be seen in Fig. 5.8(a) have been found on the chip surface after etching. Furthermore, an extreme incidence of surface roughness, as in Fig. 5.8(b), is commonly present on the chip. While such damage could be attributed to the dry etch, the occurrence of the roughness on the GaAs substrate layer points towards the roughness being created either during the wafer growth procedure or during the wet etch and cleaning step. The origin of the directionality of the cuts is unexplained. Note also the unusual thinness of the left cantilever of the slot waveguide. The two cantilevers are supposed to have equal width $w = 150\,\text{nm}$, with the left beam clearly obtaining a thickness much less than that. Figures 5.8(c) and (d) show a common source of flawed devices, namely discontinuity of the electrical wires. Fig. 5.8(e) shows the presence of an unknown residue $\sim 75\,\mu\text{m}$ in diameter. This residue seemingly prevents full undercut of the SEGs, as can be seen by the dark shadows on the central part of the gratings.

5.2.1 Device uniformity and reproducibility

The latest version of the sample was made in two copies. Fabrication was run concurrently, until the deep etching step. As the development and subsequent drying of the resist during the deep etch step had been identified as a critical step with a high failure rate due to resist collapse, the chip was cleaved to separate the two copies of the mask, and further fabrication carried out separately from there. Following fabrication, undercut and CPD, the two copies of the sample were characterized in an SEM and the yield characterized for each sample. Table 5.1 contains the yield for the two chips. Typical reasons for failed devices were collapsed or fused slot waveguides, broken wires, and non-undercut gratings. Fig. 5.9 shows images from the final sample. On Fig. 5.9(a), a successful slot waveguide device actuated by a comb drive can be seen. To characterize the response of the slot waveguide, MZIs with passive 50/50 beamsplitters are fabricated, as seen in Fig. 5.9(b). An example of a fully-undercut SEG containing square nano-holes with sidelength $l_h = 150\,\text{nm}$ can be seen in Fig. 5.9(c).

5.3 Conclusion and outlook

This chapter laid out the necessary nano-fabrication techniques for fabricating devices for integrated quantum photonics on a GaAs suspended platform. Common fabrication challenges for nano-scale suspended cantilevers have been laid out, and a

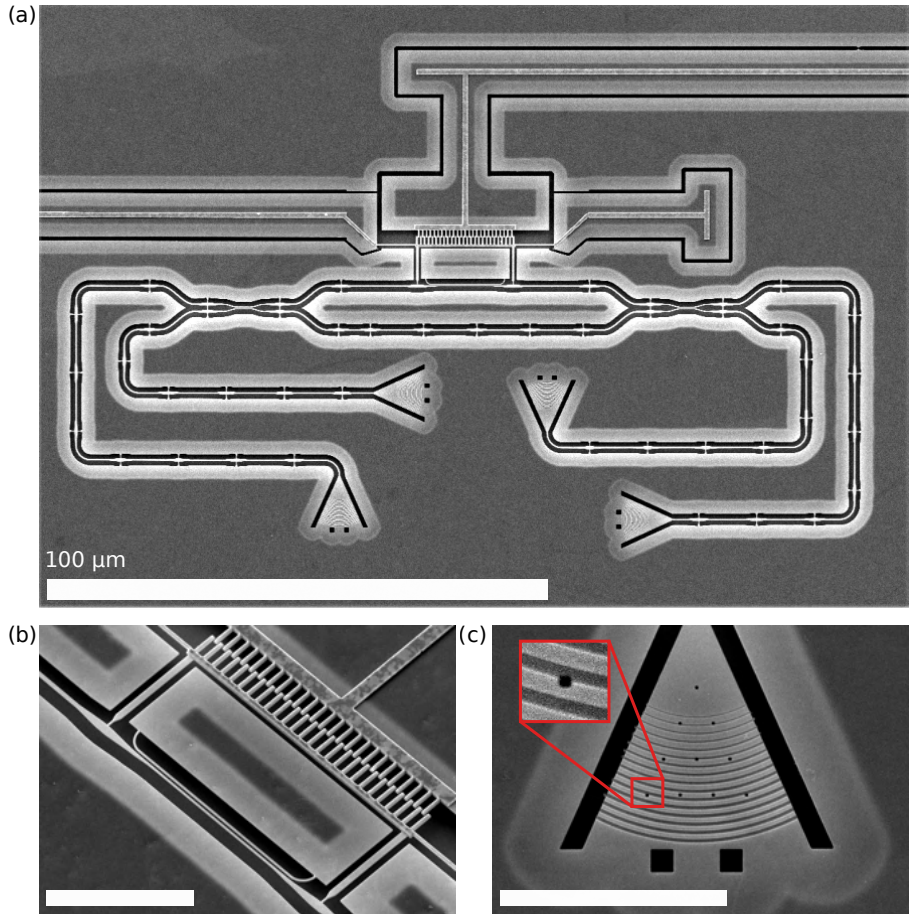

Figure 5.9: Post-fabrication SEMs of final sample. All scale bars are 10 µm unless otherwise noted. a: Full MZI device utilizing a comb drive NOEMS. The light parts are suspended or undercut, while the part parts are GaAs with an intact AlGaAs layer underneath. b: Final slot waveguide device. c: Shallow etch gratings (SEG). Insert: nanoscale holes ensure a full undercut.

technique to avoid pre-etch collapse of resist beams with high aspect ratios has been presented. The finalized device has been fabricated which, on successful fabrication runs, yields $> 60\%$, and in some cases almost 100%. The following chapter will contain a brief intermezzo from the main story of the integrated phase shifter, covering the application of intrinsic strain mismatch for purposes such as stabilizing large devices and the bending of cantilevers into vertical positions to act as chip-to-fiber couplers. Following that, the characterization of the phase shifter at both cryogenic and ambient conditions will be carried out in the subsequent chapters.

Chapter 6

Engineering of Strain in Thin Films

Strain, the deformation of a material in response to internal or external forces, is an inevitable property of samples consisting of multilayered thin films [157]. Although it can be undesired, it is also exploited in many applications, such as the Stranski-Krastanov growth of quantum dots. Additionally, it can be manipulated by exploiting the intrinsic bilayer stress between two thin films, which will be expanded on in section 6.2. This chapter will introduce elementary solid mechanics, such as linear and nonlinear strain geometries, as well as linear elastic deformation theory. The Pikus-Bir Hamiltonian describing the strain-induced bandgap changes of a direct bandgap semiconductor is also introduced.

The behavior of MEMS is complex and often depends on finicky properties such as the intrinsic strain of the material membranes, which is known to differ depending on the inevitably fluctuating conditions under which fabrication is carried out. This chapter covers the investigation into bilayer devices with different materials containing different thermal expansion coefficients, leading to temperature-dependent buckling. An introduction is given to strain engineering, where the intrinsic stress mismatch between two materials in a bilayer structure is exploited to stiffen or bend cantilevers. A theoretical investigation of the use of strain mismatch between materials to stiffen structures is presented. Furthermore, an application of strain-mismatched bilayer materials in the form of cantilever bending waveguides in a vertical orientation for use as chip-to-fiber couplers is described.

6.1 Solid mechanics

In traditional Newtonian mechanics, objects considered are typically either point masses or ideal rigid bodies incapable of deformation or fracture. In contrast, solid mechanics offers a mathematical framework to describe objects that deform, bend, or twist in response to internal or external forces, and conversely the internal forces that originate from deformation. The engineering strain tensor, which holds true in the case of small strains and infinitesimal rigid body rotations, is

$$e_{ij} = \frac{1}{2}\left(\frac{\partial u_i}{\partial X_j} + \frac{\partial u_j}{\partial X_i}\right). \tag{6.1}$$

Here $\mathbf{X}$ is the original position of the deformed particle. This is also known as a material coordinate system, as a given particle keeps its coordinate no matter the deformation, and $\mathbf{u}(\mathbf{X})$ is the displacement vector describing the difference between the original and deformed configuration for every point $\mathbf{X}$. In the case of small deformations, the above strain tensor is sufficient. However, in the case of large deformations, discrepancies begin to show. As the geometrically linear strain tensor does not take rotations into account, an object that has undergone a rotation without deformation will have a non-zero value of the linear strain tensor. Instead, the geometrically nonlinear strain tensor, also called the Green-Lagrange strain tensor, is utilized [158]

$$\varepsilon_{ij} = \frac{1}{2}\left(\frac{\partial u_i}{\partial X_j} + \frac{\partial u_j}{\partial X_i} + \frac{\partial u_k}{\partial X_j}\frac{\partial u_k}{\partial X_j}\right). \tag{6.2}$$

A rule of thumb commonly utilized in the finite element analysis (FEA) community is that, the case of modeling the deformation of a thin beam, the geometric nonlinear strain should be considered whenever the tip deflection is larger than half of the beam thickness [159]. For both linear and nonlinear strains, diagonal terms describe hydrostatic strains, which correspond to an equal expansion or compression in all directions, or bi-axial and uniaxial strains, where all angles in the object are conserved while the proportions are deformed. Off-diagonal terms, on the other hand, describe shear strains, meaning strains that twist or bend objects. All strain tensors are by definition symmetric, as can be seen from Eqs. 6.1 and 6.2. Stress is a second order tensor with units of force per area describing the internal and external forces upon a material undergoing a deformation,

$$\overline{\overline{\sigma}} = \begin{bmatrix} \sigma_{xx} & \sigma_{xy} & \sigma_{xz} \\ \sigma_{yx} & \sigma_{yy} & \sigma_{yz} \\ \sigma_{zx} & \sigma_{zy} & \sigma_{zz} \end{bmatrix}, \tag{6.3}$$

where $\sigma_{ij} = \sigma_{ji}$ for any object at rest due to the conservation of angular momentum.

Elastic deformation theory is a generalization of Hooke's law, which states that the restoring force on a displaced spring is proportional to the displacement distance,

$$F = kx. \tag{6.4}$$

Whereas Hooke's law describes a 1D system, where the restoring force in one direction depends upon a deformation in that same direction, elastic strain theory describes multi-directional forces and displacements, as well as as shear forces and displacements. Elastic deformation theory, which describes all displacements as reversible without hysteresis, can be used for small deformations, after which highly complex and material-dependent models can be used to describe yield stresses, plastic (non-reversible) deformations, and fractures. In elastic deformation theory, the relationship between stress and strain is linear. Writing up the stress and strain tensors in Voigt

notation,

$$\overline{\overline{\sigma}} = \begin{bmatrix} \sigma_{xx} & \sigma_{xy} & \sigma_{xz} \\ \sigma_{yx} & \sigma_{yy} & \sigma_{yz} \\ \sigma_{zx} & \sigma_{zy} & \sigma_{zz} \end{bmatrix} \Rightarrow \overline{\sigma} = \begin{bmatrix} \sigma_{xx} \\ \sigma_{yy} \\ \sigma_{zz} \\ \sigma_{xy} \\ \sigma_{yz} \\ \sigma_{zx} \end{bmatrix}, \quad \overline{\overline{\varepsilon}} = \begin{bmatrix} \varepsilon_{xx} & \varepsilon_{xy} & \varepsilon_{xz} \\ \varepsilon_{yx} & \varepsilon_{yy} & \varepsilon_{yz} \\ \varepsilon_{zx} & \varepsilon_{zy} & \varepsilon_{zz} \end{bmatrix} \Rightarrow \overline{\varepsilon} = \begin{bmatrix} \varepsilon_{xx} \\ \varepsilon_{yy} \\ \varepsilon_{zz} \\ \varepsilon_{xy} \\ \varepsilon_{yz} \\ \varepsilon_{zx} \end{bmatrix}, \quad (6.5)$$

the relationship between stress and strain can be described using the compliance matrix, $\overline{\overline{S}}$ and the stiffness matrix $\overline{\overline{C}}$,

$$\overline{\sigma} = \overline{\overline{C}}\overline{\varepsilon}, \quad \overline{\varepsilon} = \overline{\overline{S}}\overline{\sigma}. \quad (6.6)$$

For isotropic materials, such as cubic zincblende crystals like GaAs, the stiffness and complicance tensors take the following form [160]

$$\overline{\overline{C}} = \begin{bmatrix} C_{11} & C_{12} & C_{12} & 0 & 0 & 0 \\ C_{12} & C_{11} & C_{12} & 0 & 0 & 0 \\ C_{12} & C_{12} & C_{11} & 0 & 0 & 0 \\ 0 & 0 & 0 & C_{44} & 0 & 0 \\ 0 & 0 & 0 & 0 & C_{44} & 0 \\ 0 & 0 & 0 & 0 & 0 & C_{44} \end{bmatrix}, \quad \overline{\overline{S}} = \begin{bmatrix} S_{11} & S_{12} & S_{12} & 0 & 0 & 0 \\ S_{12} & S_{11} & S_{12} & 0 & 0 & 0 \\ S_{12} & S_{12} & S_{11} & 0 & 0 & 0 \\ 0 & 0 & 0 & S_{44} & 0 & 0 \\ 0 & 0 & 0 & 0 & S_{44} & 0 \\ 0 & 0 & 0 & 0 & 0 & S_{44} \end{bmatrix}, \quad (6.7)$$

where

$$C_{11} = \frac{E(1-\nu)}{(1+\nu)(1-2\nu)}, \quad C_{12} = \frac{E\nu}{(1+\nu)(1-2\nu)}, \quad C_{44} = \frac{E(1-2\nu)}{(1+\nu)(1-2\nu)}, \quad (6.8)$$

and

$$S_{11} = \frac{1}{E}, \quad S_{12} = \frac{-\nu}{E}, \quad S_{44} = \frac{1+\nu}{E}. \quad (6.9)$$

Here is E the Young Modulus, defined as the ratio between stress and strain, and which quantifies the the stiffness of a material, and ν Poisson's ratio, which quantifies the tendency of a material to contract (expand) in directions perpendicular to a tensile (compressive) force.

Care must be taken when defining these quantities, as common engineering notation replaces the shear strain components $\varepsilon_{ij}, i \neq j$ with the engineering shear strain, $\gamma_{ij} = 2\varepsilon_{ij}$, when using the Voigt notation which in turn respectively multiplies (divides) S_{ij} (C_{ij}) by 2 [161].

6.1.1 Strain-induced bandgap change

Macroscopic and microscopic material properties are fundamentally interconnected. The atomic structure of a crystal governs its macroscopic thermal, mechanical, or electrical properties. On the other hand, the application of mechanical or electrical forces on a macroscopic scale can alter or distort the crystal structure, thereby modifying the material's properties. This is both for passive properties (e.g. that metals

are ductile and malleable, have a metallic shine and are good thermal and electrical conductors), but also active properties, meaning that inducing a stress upon a material might induce emergent phenomena. An example of this is strain-induced bandgap shifts where the application of a strain can shift, split, and hybridize the valence band states of a direct-bandgap semiconductor. As the bandgap of a semiconductor depends upon the crystal structure, any deformation of that structure will in return cause a change in the bands. For direct-bandgap semiconductors like GaAs and InAs, there are 3 main bands in the valence band, namely the heavy hole (HH) band, the light hole (LH) band, and the split-off (SO) band [160]. While the HH and the LH bands are degenerate at the zone center, the split-off band has a significantly changed energy ($\Delta_{\text{SO, GaAs}} = 0.34\,\text{eV}$) due to the spin-orbit coupling. Hydrostatic strain will evenly scale the bands, causing larger bandgaps for compressive strain and smaller bandgaps for tensile strain. Biaxial strain will additionally split the light hole (LH) and heavy hole (HH) valence bands, while uniaxial or shear strain will also cause hybridization of the LH and HH valence bands. Neglecting the influence from the split-off band, the strain-induced perturbation to the energies of the HH and LH valence bands can be found using the 4×4 Pikus-Bir Hamiltonian,

$$H_{4x4} = \begin{bmatrix} -P_\varepsilon - Q_\varepsilon & S_\varepsilon & -R_\varepsilon & 0 \\ S_\varepsilon & -P_\varepsilon + Q_\varepsilon & 0 & -R_\varepsilon \\ -R_\varepsilon & 0 & -P_\varepsilon + Q_\varepsilon & -S_\varepsilon \\ 0 & -R_\varepsilon & -S_\varepsilon & -P_\varepsilon - Q_\varepsilon \end{bmatrix}. \tag{6.10}$$

Here

$$P_\varepsilon = a_v(\varepsilon_{xx} + \varepsilon_{yy} + \varepsilon_{zz}), \quad Q_\varepsilon = -\frac{b}{2}(\varepsilon_{xx} + \varepsilon_{yy} - 2\varepsilon_{zz}), \tag{6.11}$$

$$S_\varepsilon = -d(\varepsilon_{xz} - i\varepsilon_{yz}), \qquad R_\varepsilon = \frac{\sqrt{3}}{2} b(\varepsilon_{xx} - \varepsilon_{yy}) - id\varepsilon_{xy}, \tag{6.12}$$

where a_v is the Pikus-Bir hydrostatic deformation potential for the valence band edge, and b and d are the Pikus-Bir shear deformation potentials [160]. The values for GaAs are $a_v = -1.16\,\text{eV}$, $b = -2.0\,\text{eV}$ and $d = -4.8\,\text{eV}$. It can here clearly be seen how P_ε, which describes the hydrostatic component of the term, shifts all valence bands uniformly. Q_ε, which contains the biaxial components, splits the energy of the HH and LH bands, while R_ε and S_ε, which contain the uniaxial and shear strain components, will additionally hybridize the HH and LH bands. Diagonalizing the Hamiltonian yields the valence band energy shifts,

$$\Delta E_v = -P_\varepsilon \pm \sqrt{|Q_\varepsilon|^2 + |S_\varepsilon|^2 + |R_\varepsilon|^2}. \tag{6.13}$$

Meanwhile, for the conduction band, the energy shift is

$$\Delta E_c = a_c(\varepsilon_{xx} + \varepsilon_{yy} + \varepsilon_{zz}), \tag{6.14}$$

where a_c is the conduction band deformation potential, $a_c = -7.17\,\text{eV}$. This leads to a total energy change of the band gap

$$\Delta E_g = \Delta E_c - \Delta E_v = \Delta E_c + P_\varepsilon \pm \sqrt{|Q_\varepsilon|^2 + |S_\varepsilon|^2 + |R_\varepsilon|^2}. \tag{6.15}$$

6.2 Bilayer strain

In this section, the intrinsic stress mismatch between two thin films will be described. The use of thin bilayer cantilevers with an intrinsic strain mismatch to obtain vertical bending for use as chip-to-fiber couplers is discussed. A narrow bilayer suspended cantilever with an intrinsic stress mismatch will, upon release from the underlying substrate, curl up with a diameter described by the equation

$$\frac{1}{r} = \frac{6\varepsilon(1+m)^2}{d\left[3(1+m)^2+(1+mn)(m^2+(mn)^{-1})\right]}. \tag{6.16}$$

Here r is the radius of curvature, ε the intrinsic strain mismatch $(l_2-l_1)/l_0$ where l_0 is the strained length and $l_{1/2}$ is the unstrained length of the upper (lower) layer, $d = d_1+d_2$ is the combined thickness, $n = E_1/E_2$ the ratio of the elastic modulus of the two layers, and $m = d_1/d_2$ the thickness ratio of the two layers [162]. For bilayer cantilevers with uniform thickness $d_1 = d_2 = d_0$, this reduces to

$$\frac{1}{r} = \frac{12\varepsilon}{d_0\left[12+(1+n)(1+n^{-1})\right]}. \tag{6.17}$$

The bilayer strain mismatch has two main origins. First is the intrinsic strain mismatch, which is present at growth. The second contribution to the strain stems from different thermal expansion coefficients of the two materials, which therefore is present whenever the temperature is different than during the growth. While the second contribution can be calculated precisely, as long as the temperature in the growth chamber and the respective thermal expansion coefficients are known, the first contribution depends on the exact conditions and procedures in the growth chamber.

6.2.1 Thermal expansion simulations

Suspended devices are subject to many forces. For instance, thermal expansion or contraction can cause deformation of devices, particularly in the case of multilayer devices consisting of materials with different thermal expansion coefficients. When calculating the displacement-dependent effective refractive index of a slot waveguide mode, it is crucial to account for the precise vertical positioning of the slot waveguide. As suspended devices are prone to vertical displacement in the form of drooping or strutting, an investigation into the vertical position of the slot waveguides is necessary. This subsection contains a numerical investigation of the temperature-dependent vertical displacement slot waveguides on different designs. COMSOL simulations are carried out, and the difference between linear and nonlinear geometries in solid mechanics is exemplified.

The desired geometry is first designed in a CAD program, saved as a DXF file, and lastly imported into COMSOL. A significant portion of temperature-dependent buckling arises due to differing thermal expansion coefficients of the materials in the layered structures [162]. As a result, the materials are modeled with both a constant initial strain and a temperature-dependent strain. Fig. 6.1 shows the devices over which simulations were carried out. Both the devices consist of suspended GaAs

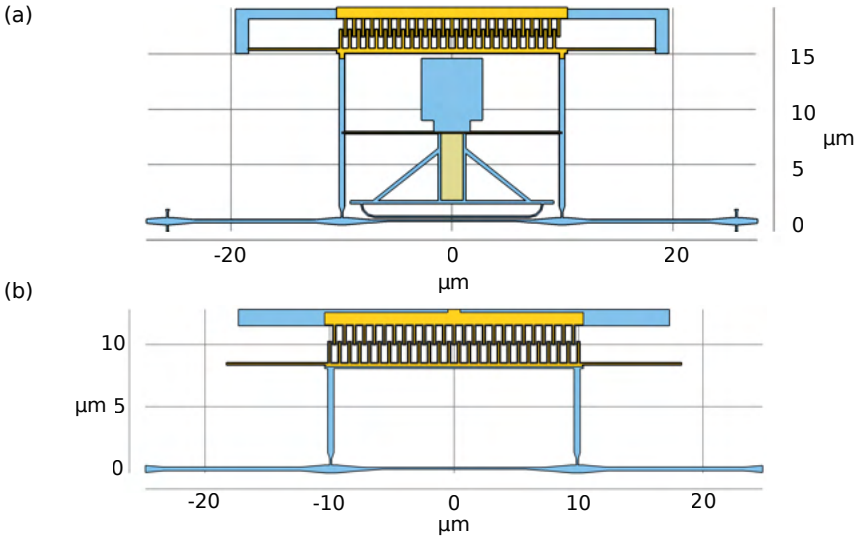

Figure 6.1: Slot waveguide phase shifter designs over which thermal displacement simulations were carried out. (a) Design with unfixed stator. (b) Design with shorter cantilever between the comb and the motor cantilever, and a fixed stator. The inner area of the design contains an island of GaAs, to which the stator is connected.

(blue) along with an Au comb drive (gold), with the design shown in Fig. 6.1(a) additionally containing a stiffening layer of Ni (light green).

While the GaAs is assumed to be stress-free under initial conditions, initial stresses are applied to the Ni and Au layers, with values of 890 MPa [163] (40 MPa [164]) for the Ni (Au) layer. A temperature-dependent strain is applied in the ε_{xx} and ε_{yy}-directions on all three materials to simulate the thermal expansion of the materials.

The strain on the GaAs is, which is derived by integrating the thermal expansion coefficient obtained from [165], is

$$\varepsilon_{\mathrm{GaAs}}(T) = -3\cdot 10^{-6}\cdot T + \frac{6.267\cdot 10^{-8}}{2}\cdot T^2 - \frac{1.104\cdot 10^{-10}}{3}\cdot T^3 - 9.6\cdot 10^{-4}, \quad (6.18)$$

while the strain on the nickel and gold, which is derived from the thermal expansion coefficients found in [166], is

$$\varepsilon_{\mathrm{met}}(T) = -5.57\cdot 10^{-7}\cdot T + \frac{8.3\cdot 10^{-8}}{2}\cdot T^2 - \frac{-1.23\cdot 10^{-10}}{2}\cdot T^3 - 2.5\cdot 10^{-3}. \quad (6.19)$$

Results of the simulation can be seen in Fig. 6.2. Subfigures (a-c) use a linear geometry, while subfigures (d-f) utilize a nonlinear geometry. The linear model shows large strutting displacement for both motor and stator arm across the temperature range, with the displacement of the motor being greater than the displacement of the stator across the investigated temperature range. Both the displacement and the difference in displacement become more pronounced the colder the temperature. The nonlinear model shows that the displacement of the stator is similar to that of the linear model.

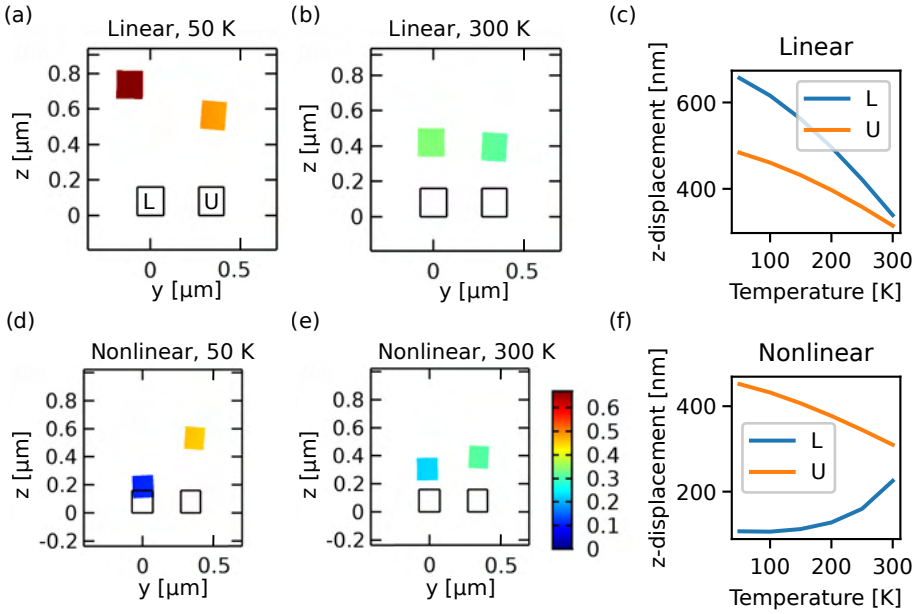

Figure 6.2: Temperature-dependent displacement of slot waveguide cantilevers in COMSOL simulations with both linear and nonlinear strain, using the design seen in Fig. 6.1(a). Subfigures a-b and d-e share the same colormap, as shown in the colorbar to the right of subfigure e. The unfilled square in each subfigure represents the initial position, and the filled squares indicates the displacement. a: Displacement at 50 K with linear geometric strain. b: Displacement at 300 K with linear geometric strain. c: Temperature-dependence of z-displacement of the motor (L) and stator (U) arm, utilizing linear geometric strain. d: Displacement at 50 K with nonlinear geometric strain. e: Displacement at 300 K utilizing nonlinear geometric strain. c: Temperature-dependence of z-displacement of the motor (L) and stator (U) arm, utilizing nonlinear geometric strain.

However, the behavior of the motor is completely different. No matter the temperature, the displacement of the motor is smaller than the displacement of the stator. In addition, unlike the stator, the displacement of the motor increases as the temperature rises. This result emphasizes the necessity of utilizing the more complex geometric nonlinearity, as the differences yield results that are not only more accurate but also fundamentally different. In the design used for this simulation, the stator arm is connected to a non-undercut area via a bilayer cantilever enabling a vertical displacement. By removing the strained nickel structure and making a shorter design, as can be seen in Fig. 6.1(b), the stator can be effectively fixed in place. Figs. 6.3(a) and (b) show the temperature displacement of the motor cantilever at, respectively, 50 K and 300 K, using a nonlinear geometry. Compared to the previous design, which had displacements of 100s of nm, the displacement of the motor cantilever of this design goes from practically nonexistent at ambient temperatures to ~ 60 nm at cryogenic conditions. This design is chosen as the device design moving forward.

In addition to the slot waveguide, a displacement is also induced in the comb drive by the temperature-dependent strain. Fig. 6.4 shows the vertical displacement of

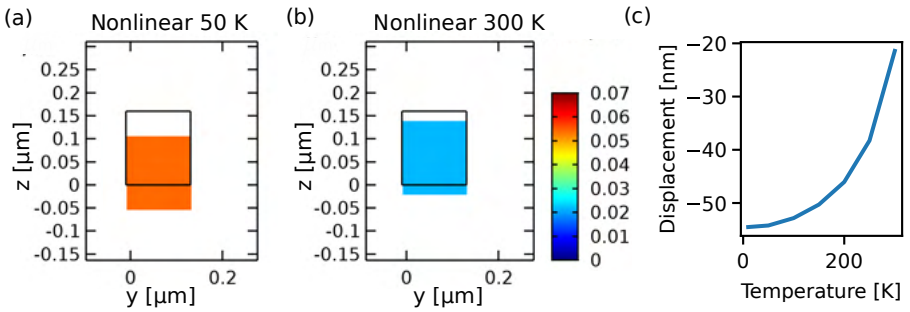

Figure 6.3: COMSOL simulation of the temperature-dependent displacement of the motor cantilever in the design seen in 6.1(b). utilizing a nonlinear geometrical strain. Subfigures a-b share the same color bar. The unfilled square in each subfigure represents the initial position, and the filled squares indicates the displacement. a: Displacement at 50 K with nonlinear geometric strain. b: Displacement at 300 K with nonlinear geometric strain. c: Temperature-dependence of z-displacement of the motor arm, utilizing nonlinear geometric strain.

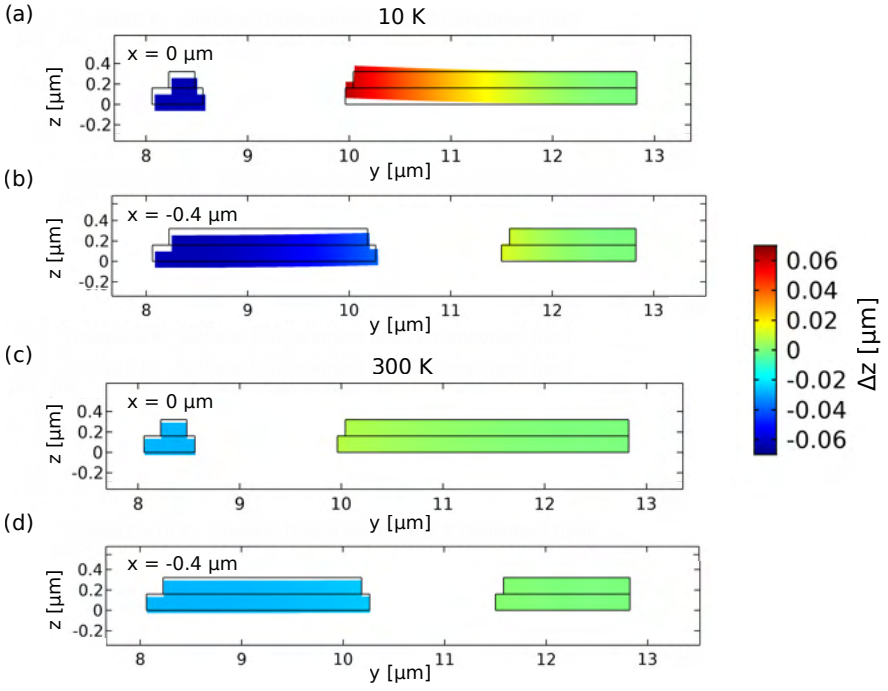

Figure 6.4: Simulated vertical displacement of the comb drives, at room and cryogenic temperatures. For each temperature, top plot is for x = 0 µm, corresponding to the x-position of the central finger of the stator comb, and bottom plot is for x = -0.4 µm, corresponding to the x-position of the central finger of the motor comb.

respectively the central stator and motor fingers of the comb drive at room and cryogenic temperatures, using the design seen in Fig. 6.1(b) and a nonlinear geometry. Fig. 6.4(a) shows, to the right, the thermal strain-induced displacement of the central stator finger at 10 K, while Fig. 6.4(b) shows, to the left, the thermal strain-induced displacement of the central finger of the motor comb. The device exhibits a moderate vertical displacement, with the tip of the stator finger being displaced 60 nm, and the tips of the motor comb being displaced ~ -40 nm. Fig. 6.4(c) and (d) show the displacement of the fingers at room temperature, where the displacement is significantly less pronounced, with the stator finger having insignificant displacement, and the motor finger having a displacement of ~ -20 nm.

6.2.2 Bent waveguide couplers

This research on cantilever bending waveguides utilized as couplers has previously been published in Optics Express [167], and much of this section is reproduced from the manuscript with minor changes.

Quantum information processing on photonic integrated circuits requires low-loss strategies for chip-to-fiber coupling. In-plane coupling, also called edge coupling, features fibers placed next to the chip. At the chip edges, an inverted taper is placed, which adiabatically converts the light mode in the fiber into a waveguide mode. These coupling strategies using inverted tapers have low loss, are broadband and polarization independent, but require a cryostat with side access, necessitate precise chip cleaving, and limit device placement to chip edges [56].

In out-of-plane coupling, the light is incident on the top surface, typically at a vertical or near-vertical angle. They typically utilize diffractive gratings which introduce destructive interference that scatters the light into the waveguide. These couplers can be placed anywhere on the sample surface, allowing a larger number of samples and easing the design requirements of the device. However, grating couplers are typically lossy, polarization dependent, and commonly limited to a bandwidth $\ll 50$ nm due to the Bragg condition [141].

Three-dimensional chip-to-fiber couplers have been created by ion implantation [168]. Furthermore, the usage of unfixed bimorph cantilevers as beam scanners whose deflection angle can be actively controlled with electrothermomechanical [169] or piezoelectric [170] actuation has been demonstrated. This section features a novel three-dimensional device consisting of a bent waveguide terminated with an inverted taper. By locking its position at 90 °, it can retain the polarization independence and bandwidth of an edge coupler while retaining the flexible placement of a grating coupler.

The device consists of a waveguide terminated with an inverted taper coupler, defined using a negative epoxy resist, connected to two bilayer cantilevers containing a high intrinsic strain mismatch. Upon release from the sacrificial layer, the cantilevers will curl up, reaching a radius of curvature that minimizes the potential energy of the structure. The locking of the coupler in vertical orientation is obtained by placing two opposing bilayer cantilever waveguides facing each other, their distance fine-tuned so that their tips are positioned next to each other when at a 90° bending angle. When

the couplers reach vertical orientation, the locks on the two cantilevers will touch each other, effectively fusing due to powerful van der Waals forces. While this does negate some of the influence on the bending radius, it is still necessary to tune the length of the cantilevers, as a too large length compared to the bending radius means the strain will be far from relaxed when the locks are in contact, which can tear the device apart, and a too small length compared to the bending radius will make the devices too short to reach each other. Thus, a theoretical analysis is required before design and fabrication.

Finite element simulations and calculations

As cantilevers are made along the [110] direction, the biaxial modulus $E' = E/(1-\nu)$, where ν is Young's modulus, should be employed, but this cancels out each other in this case as $\nu_{\mathrm{GaAs}} = \nu_{\mathrm{Ni}} = 0.31$. Assuming an intrinsic biaxial stress, the strain can be found as

$$\varepsilon = \sigma_{\mathrm{Ni}}(S_{11,\mathrm{Ni}} + S_{12,\mathrm{Ni}}) = \sigma_{\mathrm{Ni}} \frac{1-\nu_{\mathrm{Ni}}}{E_{\mathrm{Ni}}}. \tag{6.20}$$

The following values for the thicknesses and material parameters are used: $E_{\mathrm{GaAs},300\,\mathrm{K}} = 85.5\,\mathrm{GPa}$, $d_{\mathrm{GaAs}} = d_{\mathrm{Ni}} = 160\,\mathrm{nm}$, $E_{\mathrm{Ni},300\,\mathrm{K}} = 210\,\mathrm{GPa}$. Assuming an unstressed GaAs membrane, two values found in the literature measuring the intrinsic stress of Ni on GaAs deposited via PVD with a deposition rate of 2 Å/s are used, with those being $\sigma_{\mathrm{Ni}_1} = 890\,\mathrm{MPa}$ [163] and $\sigma_{\mathrm{Ni}_2} = 820\,\mathrm{MPa}$ [164]. Using equation 6.17, this leads to bending radii of, respectively,

$$r_1 = 83.5\,\mu\mathrm{m}, \quad r_2 = 76.9\,\mu\mathrm{m}. \tag{6.21}$$

To corroborate this, a FEM simulation is built in COMSOL. A 120 µm long, flat waveguide is built, and tethered to a bilayer cantilever on each side. Sweeping over a biaxial stress on the top Ni layer, a vertical orientation of the tip can be found for $\sigma_{\mathrm{Ni,\,sim}} = 925\,\mathrm{MPa}$, corresponding to a radius of curvature $r = 74.1\,\mu\mathrm{m}$. The curvature of the waveguide and the strain distribution of $\varepsilon_s = \varepsilon_{xx} + \varepsilon_{yy}$ can be seen in Fig. 6.5(a), with the simulated nonzero strain components on the top and bottom of the waveguide shown in Figs. 6.5(b) and (c).

Results

The simulated and calculated radii of curvatures are tested experimentally by creating sets of bilayer cantilevers with various lengths, as can be seen in Fig. 6.6(a). The deflection of the tip is measured using the image processing tool ImageJ, and the bending angle is derived from that. From there, the bending angle in degrees is fit to the length using the formula

$$r = \frac{180L}{\theta}, \tag{6.22}$$

where L is the length of the cantilever, r the radius of the circular arc and θ the angle of the circle section spanned by the cantilever. By fitting the measured bending angles, as can be seen in Fig. 6.6, the radius of curvature was found to be $r = 82 \pm 1\,\mu\mathrm{m}$, in

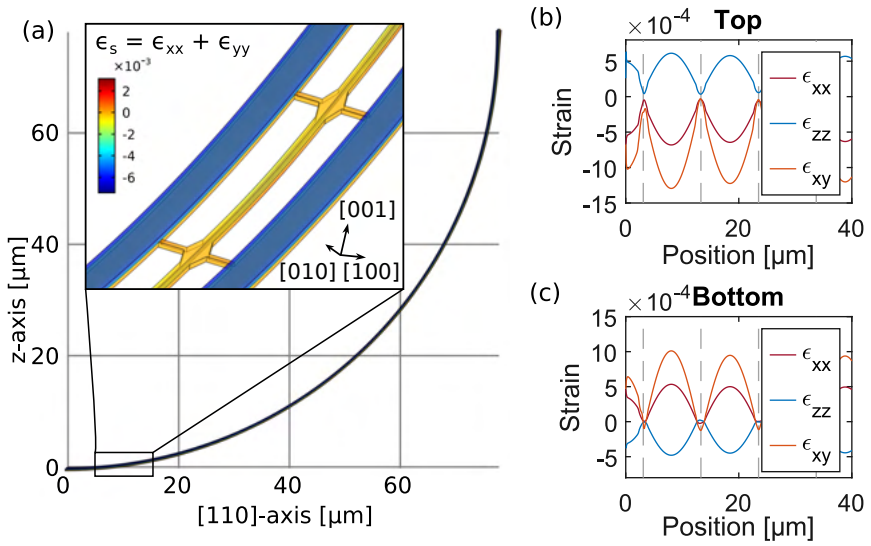

Figure 6.5: COMSOL simulation of bent cantilever waveguide coupler. a: Simulation of deformation from flat upon application of $\sigma_{\mathrm{Ni,sim}} = 925\,\mathrm{MPa}$ biaxial stress. b: Strain components ($\varepsilon_{xx} = \varepsilon_{yy}$, ε_{zz} and ε_{xy}) at the top of the waveguide. c: Strain components ($\varepsilon_{xx} = \varepsilon_{yy}$, ε_{zz} and ε_{xy}) at the bottom of the waveguide. Figure from [167]

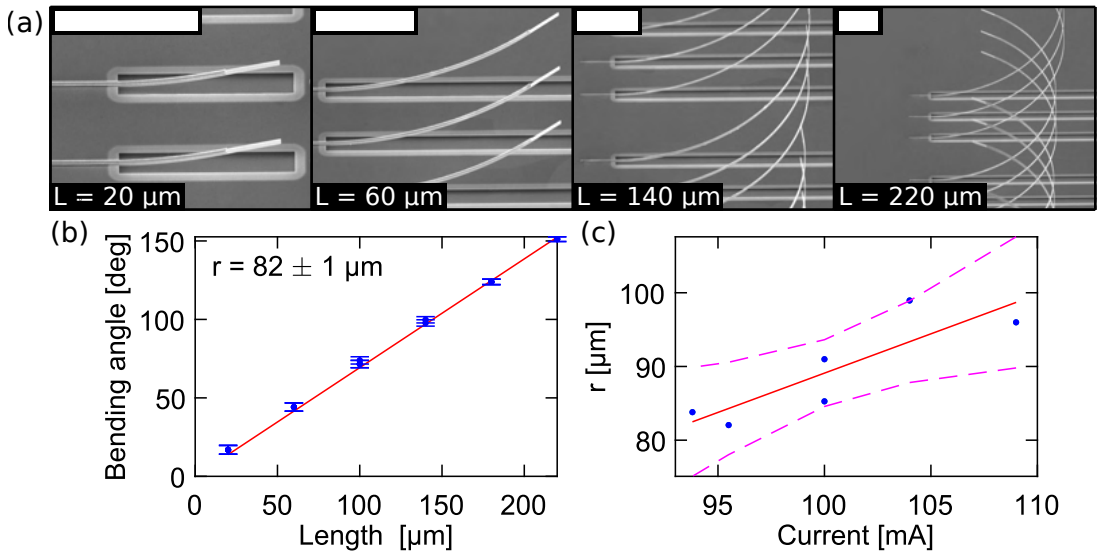

Figure 6.6: a: SEM of bilayer cantilevers of varying length. In all images, the white bar corresponds to a length of 25 μm. b: Bending angle measured with an image inspection tool, with a fit to the radius of curvature. c: Radius of curvature as a function of e-beam evaporation current with deposition rate kept constant at 2 Å/s. Figure from [167]

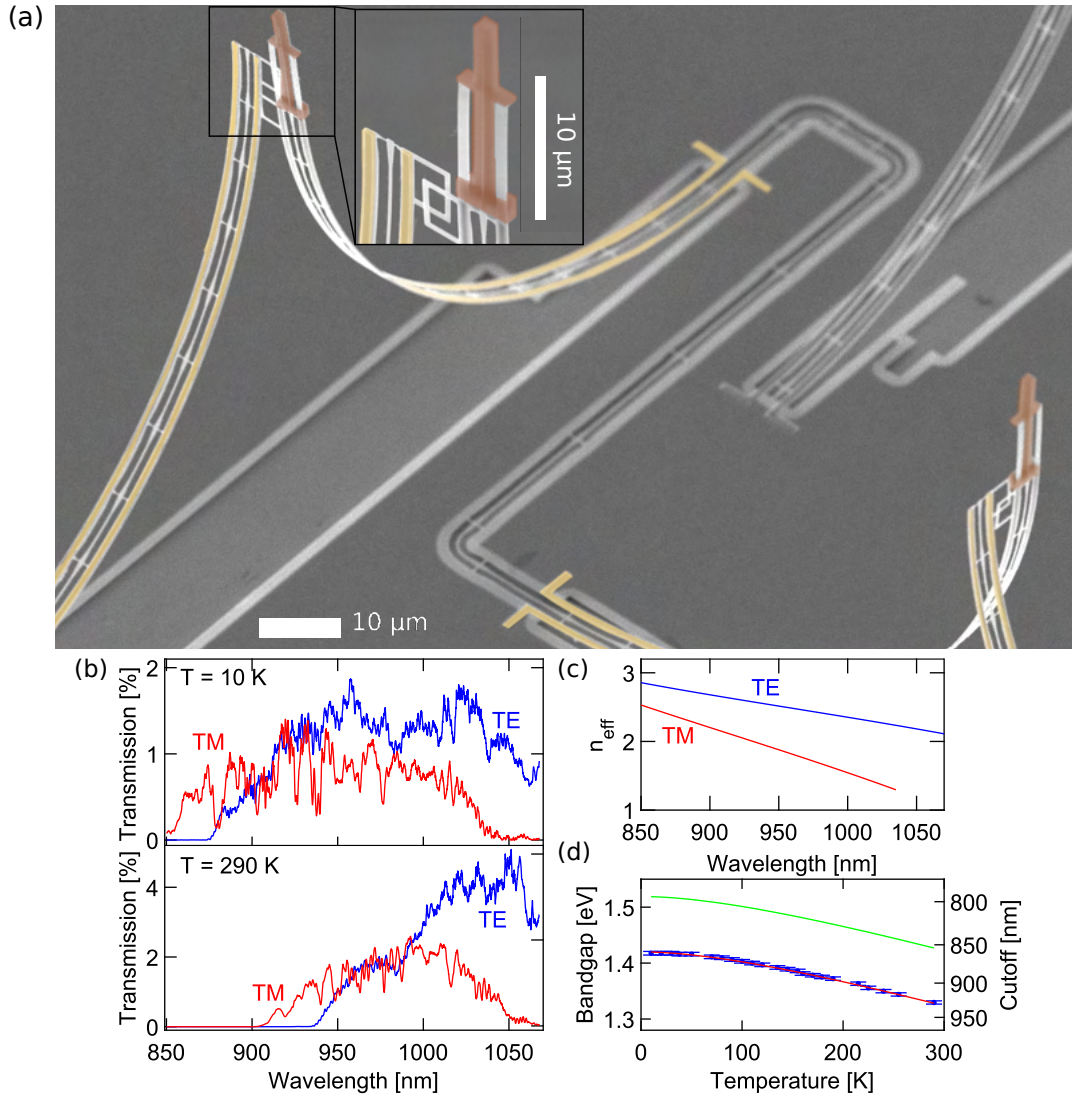

Figure 6.7: a: SEM of finished coupler. Insert: Close-up of coupler. b: End-to-end transmission of the TE and TM modes at respectively cryogenic (top) and ambient (bottom) conditions. c: Simulated wavelength-dependence of the effective refractive index of a waveguide using the same parameters as in the device. d: Temperature-dependent cutoff wavelength for the TE mode (blue), fitted to a function describing the GaAs bandgap but with a constant 0.1 eV redshift (red), compared to the unstrained GaAs bandgap (green). Figure adapted from [167].

acceptable agreement with the values found theoretically. Another interesting observation is shown in Fig. 6.6(c). The current in the e-beam evaporator is influenced by complex factors which naturally vary from evaporation to evaporation. By fabricating several sets of cantilevers in different fabrication runs, a weak positive correlation between the e-beam current and the radius of curvature was found, indicating that the current and intrinsic strain are inversely correlated, meaning that a higher current leads to a lower intrinsic strain in the Ni layer.

In Fig. 6.7, the fabricated device can be seen. A 120 µm long suspended cantilever

Efficiencies	TE	TM
10 K	$T_{\mathrm{TE,\,10\,K}} = 16 \pm 2\%$ for $900\,\mathrm{nm} \leq \mathrm{wl} \leq 1050\,\mathrm{nm}$	$T_{\mathrm{TM,\,10\,K}} = 13 \pm 2\%$ for $875\,\mathrm{nm} \leq \mathrm{wl} \leq 975\,\mathrm{nm}$
290 K	$T_{\mathrm{TE,\,290\,K}} = 26 \pm 4\%$ for $975\,\mathrm{nm} \leq \mathrm{wl} \leq 1050\,\mathrm{nm}$	$T_{\mathrm{TM,\,290\,K}} = 20 \pm 2\%$ for $950\,\mathrm{nm} \leq \mathrm{wl} \leq 1025\,\mathrm{nm}$

Table 6.1: Efficiencies for a single coupler at respectively cryogenic and room temperatures, for respectively the TE and TM modes. Note the different interval for each combination of mode and temperature.

waveguide is bilaterally tethered to a bilayer GaAs / Ni cantilever with high intrinsic tensile biaxial stress in the Ni layer. Upon release from the underlying sacrificial layer, the Ni layer seeks to contract, curling up the whole cantilever until the potential energy is minimized. Vertical stabilization is obtained by utilizing a hook mechanism, which locks two opposing cantilever waveguides against each other. One of the waveguides is terminated with an inverted taper with an epoxy spot size converter [171]. Two of these devices are connected and placed at an angle of 90° to ensure cross-polarization of the outputs.

The finalized device is placed inside a He4 flow cryostat, and the transmission is characterized using a NKT Photonics SuperK Extreme supercontinuum laser both at ambient and cryogenic temperatures. The transverse electric (TE) and transverse magnetic (TM) modes are identified by utilizing a set of shallow etched gratings (SEGs), which transmit TE modes but not TM modes, fabricated on another chip bonded to the same PCB.

In Fig. 6.7(c), the simulated effective refractive index (n_{eff}) in a standard single-mode GaAs waveguide is shown. Although the TE mode remains strongly confined with $n_{\mathrm{eff,\,TE}} > 2$ throughout the experimental range, the TM mode is only weakly confined for $\lambda > 1000\,\mathrm{nm}$, with $n_{\mathrm{eff,\,TM}} \to 1$ for $\lambda > 1050\,\mathrm{nm}$. To obtain the coupler efficiency, a calibration reference spectrum I_{ref} is obtained by focusing the excitation and collection paths on a homogeneous area of unpatterned GaAs. Using $R_{\mathrm{GaAs}} \approx 0.31$, which assumes a constant refractive index of 3.5, the transmittance through the total circuit can be calculated $T_{\mathrm{tot}} = I_{\mathrm{tot}}/I_{\mathrm{ref}} R_{\mathrm{GaAs}}$, which is shown in 6.7(b).

Previously, suspended cantilever waveguides with the same specifications have been found to have a loss of $\alpha_{\mathrm{TE}} = -7.7 \pm 1\,\mathrm{dB/mm}$ at 930 nm [172]. With a total waveguide length of 0.435 mm, expected propagation losses are $-3.3 \pm 0.4\,\mathrm{dB}$. Assuming two identical couplers, this gives a coupler transmittivity

$$T_{\mathrm{coup}} = \sqrt{\frac{T_{\mathrm{tot}}}{T_{\mathrm{wg}}}}. \tag{6.23}$$

The device exhibits broadband transmission for TE-polarized light, with a full-width half-maximum (FWHM) that extends over 150 nm at 10 K. As the measured spectrum exhibits strong fluctuations, the coupler efficiency is best described as the average over a given interval.

Assuming two identical couplers, the mean efficiency of a single coupler can be seen in Table 6.1 with the standard deviation of the efficiencies over the interval being

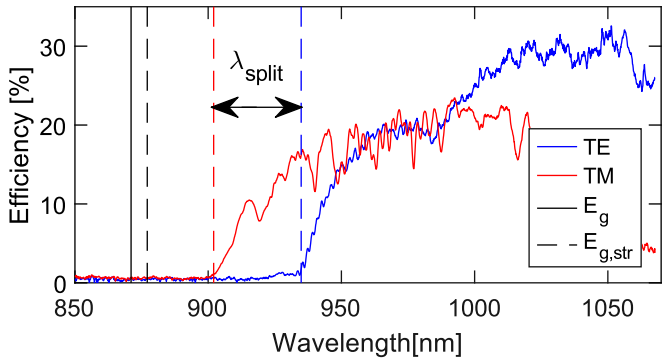

Figure 6.8: Wavelength-dependent efficiency of a single TE and TM coupler at room temperature. λ_{split} between the cutoff of the TE and TM modes is shown, compared to the energy of the unstrained bandgap (E_g). $E_{g,\text{str}}$ is the bandgap of the energy band with the largest change, calculated using the strain values obtained in the simulation.

used as uncertainty. At 930 nm, which is a common wavelength for single photons emitted by InAs quantum dots, the efficiency of the TE mode at 10 K is estimated at $(15 \pm 2\%)$, with the error originating from the uncertainty on the waveguide loss.

A remarkable feature of the bent cantilever couplers is the sharp wavelength- and polarization-dependent cutoff. This cutoff was observed in several devices, both with and without epoxy spot size converters, which can be seen in Appendix A. Furthermore, this cutoff does not vary with optical power, which rules out thermal effects as well as electrooptic responses such as the Pockels and Kerr effects. To fully characterize this behavior, a series of TE transmission measurement series was taken while gradually cooling down, and the cutoff, defined at the wavelength at which the intensity reaches 0.5% of the maximum, was identified at each temperature. On Fig. 6.7(d), the measured results (blue) are compared to the theoretical GaAs bandgap(green), which can be described with the formula [88]

$$E(T) = 1.519\,\text{eV} - \frac{5.408 \cdot 10^{-4}\,\text{eV/K} \cdot T^2}{T + 204\,\text{K}}. \tag{6.24}$$

By fitting to the same formula with two parameters,

$$E_{\text{meas}}(T) = \alpha - \frac{\beta \cdot T^2}{T + 204\,\text{K}}, \tag{6.25}$$

the parameters $\alpha = 1.42\,\text{eV}$, $\beta = 5.87 \cdot 10^{-4}\,\text{eV/K}$ are found, from which an estimation for the measured bandgap (red) is calculated. This gives a close-to-constant 0.1 eV redshift of the bandgap. It is well known that the application of a strain can produce a significant bandgap shift, and even potentially flip the quantization axis of GaAs quantum dots [91]. From the simulation, the in-plane strain along the material coordinates is $\varepsilon_{xx} = \varepsilon_{yy} = -\varepsilon_{zz} = \pm\frac{1}{2}\varepsilon_{xy}$, where the plus sign is for waveguides fabricated along the $[110]$ axis, and the minus sign is for waveguides fabricated along the $[1\bar{1}0]$ axis.

The Pikus-Bir Hamiltonian describes strain-induced bandgap change in bulk semiconductors. The largest compressive (tensile) strain is found on the top (bottom) surface of the waveguide. For the purpose of this analysis, the tensile strain is relevant to analyze as tensile strain leads to a larger interatomic distance, lowering the bandgap energies. As seen in Fig. 6.5, the strain values at the top and bottom of the waveguide are almost exactly flipped in sign. At the middle of the waveguide, the strains cancel out almost completely. The magnitude of the strain in the middle, where the emitters are grown, is found by the simulations to be in the order of $\varepsilon_{xx} \approx 10^{-4}$. Using the Pikus-Bir Hamiltonian, the wavelength shift for a 930 nm InAs quantum emitter is < 1 nm. As this is a static shift rather than a continuously tunable value, this shift is insignificant compared to the variation induced by minor structural differences in the quantum dots, which is in the order of (930 ± 10) nm for a given wafer.

At 290 K, the measured wavelength cutoff shift compared to unstrained GaAs is 64 nm (31 nm) for the TE (TM) mode. By using the strain values shown in Fig. 6.5, and calculating the bandgap shifts for the maximum tensile strain using the Pikus-Bir matrix as presented in equation 6.10 leads to a bandgap shift of

$$\Delta E = \{4.8 \pm 5.1\} \cdot 10^{-3}\,\text{eV}, \tag{6.26}$$

where the $\pm$ indicates the energies of the two no longer degenerate valence bands, as in equation 6.15. Using the strain found in the simulation thus yields changes in the cut-off wavelength of $\Delta\lambda_{\text{up}} = 6.0\,\text{nm}$ and $\Delta\lambda_{\text{down}} = -0.21\,\text{nm}$. 6.8 shows the TE and TM modes at room temperature, with λ_{split} illustrating the energy split of the TE and TM modes. Neglecting to plot λ_{down}, as the minuscule change leaves the line indistinguishable from that of the absorption edge, the wavelengths corresponding to the unstrained bandgap E_g and the strained bandgap $E_{g,\text{str}}$ are plotted. It is clearly evident that both the shifting and the splitting of the bandgap energies are much larger than those calculated with the Pikus-Bir Hamiltonian. The exact determination of the bandgap shift from cut-off measurements and the consequent absorption strength is not trivial, as losses occur predominantly on the surface of the waveguide. Here, the combination of lattice disorder, mid-gap states, surface oxides, and stress produces Fermi-level pinning and piezoelectric-induced electric fields, which are likely to enhance absorption below the gap over several tens of meV, for example, due to electroabsorption [26]. Moreover, electroabsorption is highly polarization-dependent, which could also explain the difference in cut-off for the TE and TM modes, which couple differently to light- and heavy-hole valence bands. Furthermore, the strain in the waveguide could have an additional component induced by the stabilizing hook at the end of the cantilever waveguide, which could induce a torque from contact with the opposing cantilever. Discerning the individual contributions from all these effects is, however, beyond the scope of this thesis and requires further investigation.

The natural quantization axis for InAs quantum dots with stronger confinement in the z-direction compared to the x- and y-directions is along the z-axis. This causes the orientation of the HH holes to have vectorial components capable of coupling to both the TE mode and the TM mode, while the interaction dipole of the LH state only couples to the TM mode [91]. Biaxial strain splits the HH and LH states, with the LH states obtaining the larger bandgap shift than the HH states due to the smaller effective

mass of the electron in such states. This is inconsistent with the TE mode obtaining a much larger cutoff change than the TM mode, despite the fact that it, under normal conditions, will couple to the HH holes only, while the TM mode will couple to both the HH and LH modes. Previous research has shown that moderate uniaxial stress is capable of flipping the quantization axis of a quantum dot entirely [91]. It is plausible that the combination of the large shear strain component, which will hybridize the LH and HH states, and the absorption mainly taking place at the surface, interacts with and changes the interaction rules between the two bandgap states and the two guided modes, allowing for the TE mode to obtain a much larger change of the absorption edge than the TM mode.

6.3 Connection and outlook

Mismatches in thermal expansion coefficients can cause significant buckling and deformation of bilayer devices. This effect can cause unintended effects in cryogenic MEMS, such as by moving the cantilevers of a slot waveguide or fingers of a comb drive out of alignment with each other. However, it can also be exploited to create intricate three-dimensional structures, by lifting bilayer cantilevers out of plane upon release from the substrate. A broadband chip-to-fiber coupler that exhibits transmission of both TE and TM modes was designed, fabricated, and characterized. Using a cantilever waveguide bent at a 90-degree angle due to strain mismatch between the GaAs membrane and an evaporated Ni film, the broad bandwidth of an edge coupler could be combined with the flexible placement of a surface coupler. This device exhibits broadband coupling for both the TE and the TM modes, with the TE mode of a single coupler having an estimated lower bound of the efficiency of $16 \pm 2\%$ in a 150-nm wide interval at 10 K. Towards the development of robust and more efficient chip-to-fiber couplers, future work will involve encapsulating the structures to gain mechanical stability and use direct fiber coupling instead of confocal setups.

The significant shift in the absorption edge compared to unstrained GaAs and the large split between the TE and TM modes indicate the presence of interesting strain-induced phenomena. Developing a deeper understanding of these phenomena could enable additional control of the coupling between semiconductor bands and waveguide modes.

Chapter 7

A Suspended Platform Slot Mode Phaseshifter

7.1 Introduction

In chapter 4, the design and performance of a slot waveguide phase shifter on a suspended GaAs platform was thoroughly described. In chapter 5, nanofabrication methods and techniques for designing mechanically actuated photonic systems on a suspended GaAs platform were laid out. In this chapter, the coupling loss in the slab-to-slot waveguide couplers is thoroughly characterized both theoretically and experimentally. Additionally, the experimental characterization at both 293 K and 10 K of a slot waveguide phase shifter embedded in one arm of an MZI is presented.

7.2 Chip layout

The chip is designed with six columns, two of them containing slot waveguides actuated using comb drives, and four of them containing other devices. Two columns containing the same type of device share an electrical contact, as seen in Fig. 7.1. In order to simplify wirebonding and reduce the required number of bonds going chip-to-chip carrier, the mask is designed with a shared ground. This allows just a single chip-to-chip carrier bond for all of the grounding. After fabrication, the chip is inspected in a scanning electron microscope (SEM), and devices with fused slot waveguides, broken electrical wires, or other catastrophic failures are noted down. Following visual inspection, the chip is bonded to a chip carrier using silver paste and wirebonded with 25 μm gold wire before being placed in a cryostat.

7.3 Experimental setup

Characterizing integrated quantum photonic circuits requires finely tuned experimental setups. Cryostats are required to carry out experiments involving single photons emitted by quantum dots, as temperatures $< 10\,\mathrm{K}$ are needed to suppress phonon noise.

Figure 7.1: Layout of the fabricated chip. One box corresponds to 100 µm. Bonding pads are shown in brown, with wires shown in purple. Pads labeled "G" show the shared ground, while pads labeled "E1/2/3" show the three electrodes, each of which is connected to two colums of devices. Areas shaded in blue contain MZIs with slot waveguide phase shifters utilizing comb drives embedded in one arm, while areas shaded in blue with white cross hatches contain devices for characterizing the lifetime and intensity of quantum dots, which will be described in chapter 8. Areas in boxes labeled "T" contains test devices for characterizing the loss in the slab-to-slot waveguide couplers. The rest of the chip contains unrelated devices.

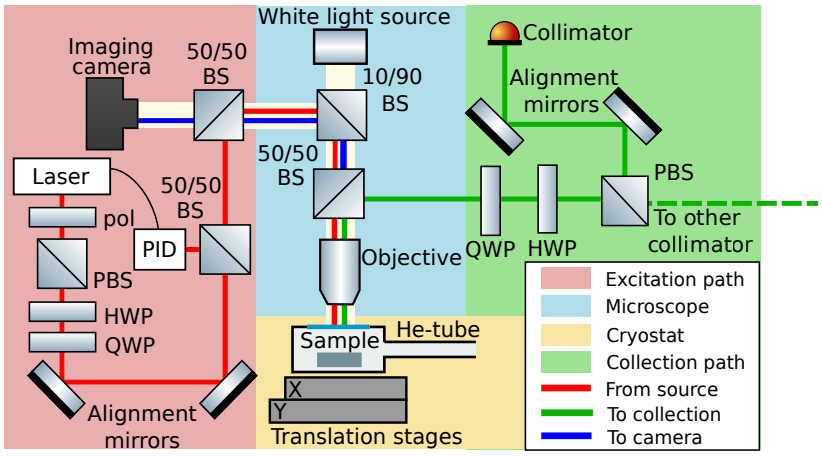

Figure 7.2: Setup utilized in the flow cryostat.

Fig. 7.2 shows the layout of the experimental setup connected to the flow cryostat. To ensure stability of the power in the setup, which is especially important whenever measuring losses and efficiencies of the slot waveguide couplers, the laser power is controlled using a proportional-integral-derivative (PID) controller with an in-house design. A polarizing beam splitter (PBS) polarizes the incoming light from the laser, while a set of waveplates consisting of a half wave plate (HWP) and a quarter wave plate (QWP) allows for precise polarization control. A set of alignment mirrors allows precise guiding of the laser beam. The light is guided into a microscope which focuses the light. A beam splitter in the microscope splits the outgoing light from the sample into two paths, one going towards the collection path and one towards the imaging camera, allowing visual inspection of the laser spots on the sample, as well as the sample surface when illuminated by a white light source located in the microscope. A fixed objective enables optical access to an area of roughly $80 \times 100\,\mu\text{m}$. Similarly to the excitation path, the collection path contains a set of waveplates allowing for precise polarization control. This path contains a polarizing beam splitter, allowing for separation of two different optical paths with orthogonal polarizations. Each path contains a single photon collimator and two alignment mirrors allowing control of the optical path. The collimators can be connected through the fiber to a spectrometer or avalanche photon detector (APD) to carry out measurements, or to a light source such as a laser, by which the path can be aligned from the collection site.

The sample is placed in a flow cryostat containing a set of 5 electrical connections. The cryostat head is placed on top of XY-nanopositioners allowing precise, ahysteretic positioning with a minimum step size of $0.1\,\mu\text{m}$. The nanopositioners are controlled using a graphical user interface (GUI) written in Python. Due to the PCB in the cryostat head being rotated compared to the X- and Y-directions of the translation stages, a consistent rotation of $\sim 11 - 13^\circ$ between the coordinate system of the nanopositioners and the fabricated chip has been noted. This is corrected for by embedding an option in the GUI to define an angle when moving the nanopositioners, enabling the quick scanning of several devices.

7.4 Loss of the slot waveguide coupler

Slot waveguides are intrinsically lossy due to the mode being confined outside the waveguide [54]. Particularly, the conversion from slab-to-slot modes is a common source of loss in slot waveguides, and therefore requires consideration during the design stage. Many integrated technologies require on-chip mode conversions. Examples include chip-to-fiber coupling, where a Gaussian free-space mode is converted into a waveguide mode, conversions between TE and TM modes, and mode conversions between active and inactive areas of the integrated circuit. Under optimal conditions, this coupling should be adiabatic, meaning that the change in effective refractive index should be continuous.

This adiabaticity, however, is often not obtainable in practice. The waveguides and other nano-features are fabricated using electron beam lithography and etching techniques, which cannot produce infinitely small features necessary to continuously

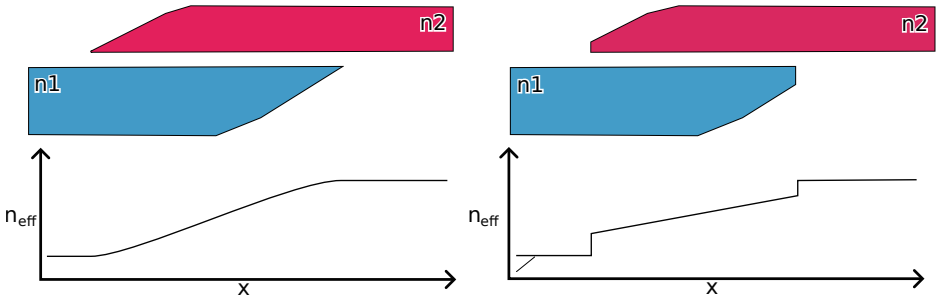

Figure 7.3: Sketch of effective refractive index of the mode over a waveguide coupler, with infinitely small minimum feature size (left) and a finite minimum feature size (right)

transfer the mode at the edge, as shown in Fig. 7.3 (left). As a result, the finite minimal feature size leads to discrete changes in the effective refractive index seen 7.3 (right). This abrupt change can lead to losses due to scattering. However, this issue can be partially mitigated by employing a gradient tapering design. In this subsection, preliminary simulations of the slab-to-slot waveguides couplers are carried out in COMSOL, using different coupler designs . Three different designs are fabricated, and their losses are characterized.

7.4.1 Theory and simulations

The simulations are built in COMSOL using the frequency domain study in the Radio Frequency module. As the slot waveguide is assumed symmetric across the horizontal plane, only one half of the setup is designed, and the Perfect Magnetic Conductor boundary conditions are used to mirror the geometry. To avoid back-reflection, a Perfectly Matched Layer (PML) with a thickness of 1 µm is placed on the boundaries of the simulation. At each end of the simulation, a port is placed. The simulation solves for the scattering parameter S_{ij}, which is the fraction of the light entering port j which exits through port i. That is, S_{11} is the fraction of the light being back-reflected, while S_{21} is the fraction of the light exiting the device through port 2 [173]. As $S_{11} + S_{21} \leq 1$, any remainder $L = 1 - S_{11} - S_{21}$ represents light attenuated or scattered out of the two investigated modes. Attenuation is typically calculated in decibels, where

$$S_{ij,dB} = 10 \cdot \log_{10}(S_{ij}). \tag{7.1}$$

Two different designs for respectively the top and bottom cantilever were considered. Here, "top" is the term used for the stator cantilever. "Bottom" is the motor cantilever, which tapers in from a slab waveguide to form one cantilever of the slot waveguide. For the bottom cantilever, which tapers from a waveguide to one of the cantilevers in the slot waveguide, a simple parametric taper was designed. In addition, a logarithmic design was made using a logarithmic function to taper in the bottom of the cantilever as it has been found that the optimal taper for a strip-to-slot waveguide converter is a logarithmic taper, as that allows for a linear power transfer from the ingoing waveguide to the slot mode [174]. On the top cantilever, a simple design using a circularly

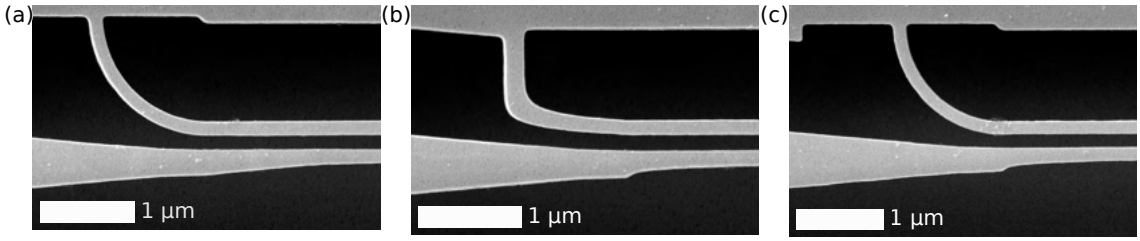

Figure 7.4: Types of couplers. (a) Simple design with a circular top cantilever and a parametric bottom cantilever. (b) Design utilizing a logarithmic coupler at both the top and bottom cantilever. (c) Design utilizing a logarithmic (circular) coupler at the bottom (top) cantilever.

shaped cantilever is made. In addition, a complex cantilever following a logarithmic function is also designed and optimized using a parametric sweep over the geometric parameters describing the shape of the cantilever. Characteristic parameters to consider in the simulation include L, which is the length of the coupling areas, and A_{bot} and A_{top}, which are characteristic parameters describing the coefficients in the logarithmic function used for respectively the top and bottom cantilever. The logarithmic parameter is described with the function

$$h(x) = w0 - A_{\text{bot}} \cdot \log_{10}(B \cdot x + 1), \tag{7.2}$$

where

$$B = \frac{10^{\frac{w0-w1}{A_{\text{bot}}}} - 1}{L}. \tag{7.3}$$

Here A is the characteristic parameter describing the bending strength of the logarithmic function, B is the normalization parameter, L the length of the coupling area, w_0 the width at the beginning of the coupling area, and w_1 the width at the end. The bottom cantilever is built in a work plane by combining an open curve polygon with a parametric curve, which is then extruded into the 3D model. Similarly, the upper cantilever is built with the function

$$h(x) = h_{\text{top}} - A_{\text{top}} \cdot \log_{10}(B_{\text{top}} \cdot x + 1). \tag{7.4}$$

where

$$B_{\text{up}} = \frac{10^{\frac{h_{\text{top}}}{A_{\text{top}}}} - 1}{L_{\text{top}}}, \tag{7.5}$$

This analytic function describes a line that follows the bottommost curve of the upper cantilever. The full cantilever is created in COMSOL by creating two lines with a logarithmic function, one of which is at an offset to create a cantilever with a constant width.

All of the simulations were carried out utilizing an initial gap width of 150 nm. Three different designs were fabricated, which can be seen in Fig. 7.4. For simplicity, the design in Fig. 7.4(a), with the parametric bottom cantilever, will be referred to

wl	930 nm		940 nm		950 nm	
	Eff [%]	dB	Eff [%]	dB	Eff [%]	dB
Pcirc	76.3	-1.17	76.9	-1.14	77.6	-1.10
LogCirc	87.2	-0.59	91.0	-0.41	93.8	-0.28
LogLog	94.7	-0.24	94.7	-0.25	93.9	-0.28

Table 7.1: Simulated slab-to-slot mode conversion loss for the three different slot wave guide coupler designs.

as "ParamCirc", the design seen in Fig. 7.4(b), will be referred to as "DoubleLog", and the design seen in Fig. 7.4(c) will be referred to as "LogCirc". In the end, the chosen parameters were $L = 2\,\mu\text{m}$, $A_{\text{top}} = 0.15$, and $A_{\text{bot}} = 0.05$, leading to simulated efficiencies and losses, as can be seen in Table 7.1.

Experimental characterization of the slab-to-slot mode conversion loss

The three different designs, as shown in Fig. 7.4, were fabricated for three different gap widths: 140 nm, 160 nm, and 180 nm, all of them with both slot waveguide cantilevers having width $w = 150\,\text{nm}$. For each gap width, four different lengths of the slot waveguide were fabricated, $L = 4\,\mu\text{m}$, $L = 7\,\mu\text{m}$, $L = 10\,\mu\text{m}$, and $L = 12\,\mu\text{m}$. For each set of spatial parameters, a quad of devices was fabricated, with respectively 0, 1, 2, and 3 slot waveguides in a single circuit.

An example of these coupler circuit sets can be seen in Fig. 7.5. Following the fabrication, broken or otherwise damaged structures are identified using an SEM. An example of a structure damaged due to debris can be seen in Fig. 7.5(b). After this, the chip is placed in the cryostat, and a CTL laser at 950 nm is aligned to the excitation grating. The collected light from the other grating is detected with a Princeton Spec-

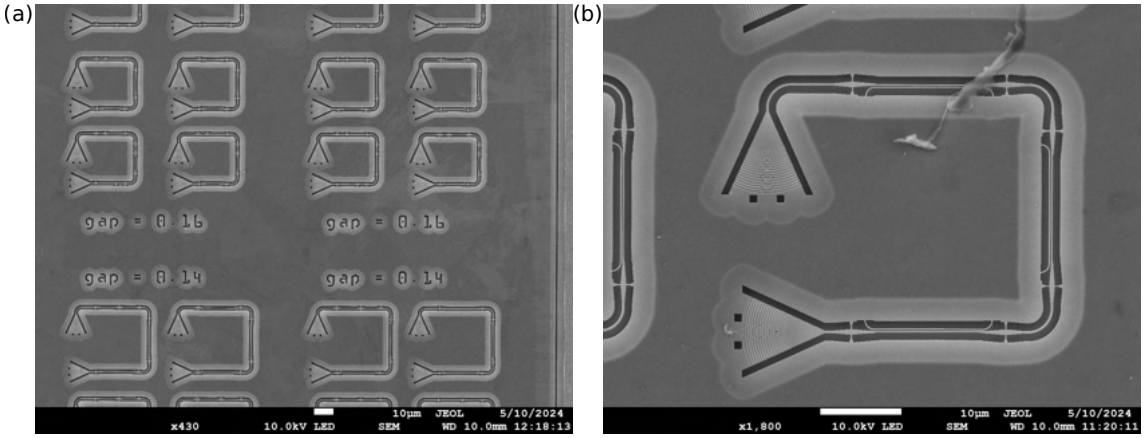

Figure 7.5: Coupler circuits. a: Zoomed-out SEM showing several loss testing circuits with different geometric parameters. b: Zoomed-in SEM of single circuit containing 3 slot waveguides.

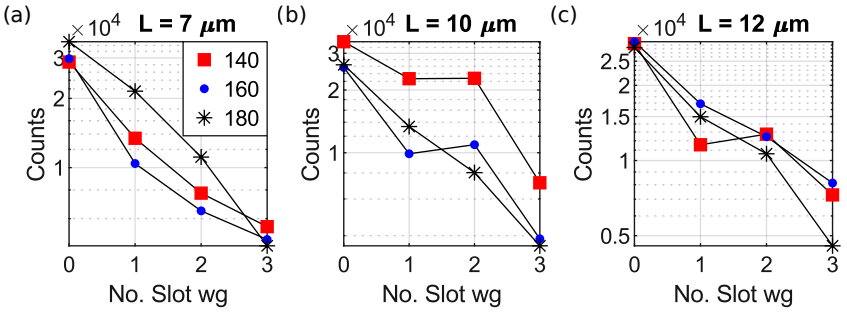

Figure 7.6: Measured counts for test circuits utilizing the ParamCirc coupler design plotted against the number of slot waveguides in the circuits. The transmission is measured for slot waveguides with cantilever widths $w = 150\,\text{nm}$, slot waveguide lengths $L = 7,\ 10,\ 12\,\mu\text{m}$ and gaps $g = 140,\ 160,\ 180\,\text{nm}$.

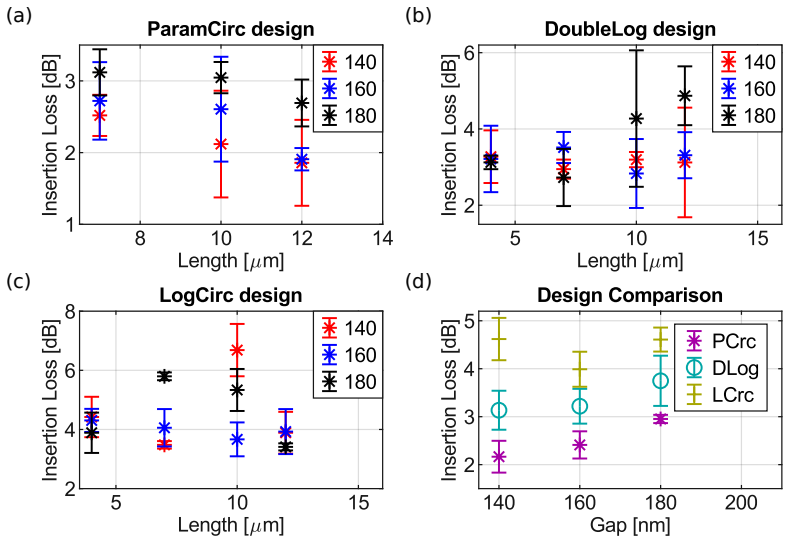

Figure 7.7: Measured insertion loss for the three different designs. a: Loss vs slot waveguide length for the ParamCirc design. b: Loss vs slot waveguide length for the DoubleLog design. c: Loss vs slot waveguide length for the LogCirc design. d: Gap-dependent insertion loss per slot waveguide coupler, found by averaging values for different lengths.

traPro 2500i spectrometer. On each path, polarization control was carried out using a set of wave plates, in order to ensure maximum efficiency and minimum crosstalk between the polarization-sensitive gratings. This characterization was carried out at room temperature. Using the obtained value for the circuit with zero slot waveguides as a reference measurement, the relative loss in dB is found for the circuits with 1, 2, and 3 slot waveguides, from which the loss in dB can be fitted.

Fig. 7.6 shows the dependence of the insertion loss on slot waveguide length and cantilever gap for the ParamCirc design. Each subfigure shows the measured counts plotted against the number of slot waveguides for the three different gaps. From this, a logarithmic fit to the insertion loss per slot waveguide is carried out. A comparison of the calculated losses for the three different designs plotted against the slot waveguide length can be seen in Fig. 7.7. Note that data for the ParamCirc coupler for $L = 4\,\mu\text{m}$

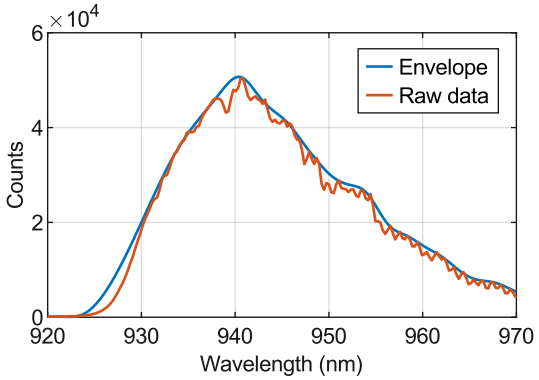

Figure 7.8: Example of raw data taken when measuring a loss test circuit, compared to the fitted envelope function.

is missing and not hidden behind the legend.

It can be seen that the loss is mostly independent of the slot waveguide length, leaving it plausible that the majority of the loss happens during the slab-to-slot waveguide transition. Averaging over the loss for each length, the measured insertion losses for the three different designs can be seen in subFig. 7.7(d). The ParamCirc (PCirc) and DoubleLog (DLog) designs exhibit increasing losses for larger slot waveguide gaps, while the loss of the LogCirc (LCrc) appears gap-independent within the uncertainties of the measurement.

Characterization using a continuous laser

Following the loss characterization carried out at 950 nm, the transmission of the slot waveguide couplers is characterized over a wider spectrum by using an NKT Photonics SuperK supercontinuum laser. An example of the spectrum measured at room temperature can be seen on Fig. 7.8. Fringes can be seen for the long waveguides of the spectra, and are indicative of a standing wave somewhere in the setup. For this reason, an envelope function is applied to the spectrum, as can be seen in the figure. The loss investigation utilizing the continuous laser was done for the length $L = 7\,\mu$m. Following the measurements, the three types of couplers were investigated.

The wavelength-dependent loss profiles of the three different designs can be seen in Figs. 7.9, 7.10 and 7.11. The three designs exhibit different wavelength-dependent behavior. All have similar losses for the lowest investigated wavelengths at 930 nm. The ParamCirc design shows behavior that, while fluctuating slightly, is mostly stable within the uncertainties of each given gap width. The loss in the DoubleLog design is slowly rising, while the loss in the LogCirc design steeply rises.

Conclusion on the loss measurements

To ensure consistency, the simulated losses of a single coupler at 950 nm were compared to the measured values utilizing the SuperK and CTL laser at 950 nm. Here it is assumed that the loss stems purely from the coupling and not the propagation

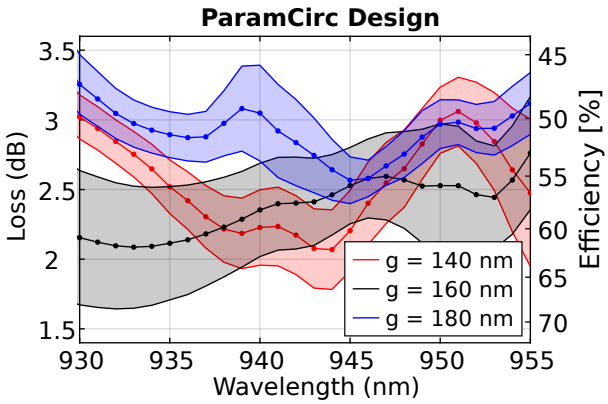

Figure 7.9: Wavelength-dependent insertion loss per slot waveguide for the ParamCirc Design

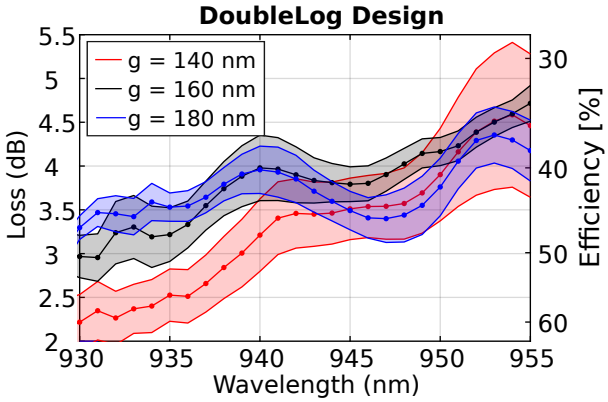

Figure 7.10: Wavelength-dependent insertion loss per slot waveguide for the DoubleLog Design

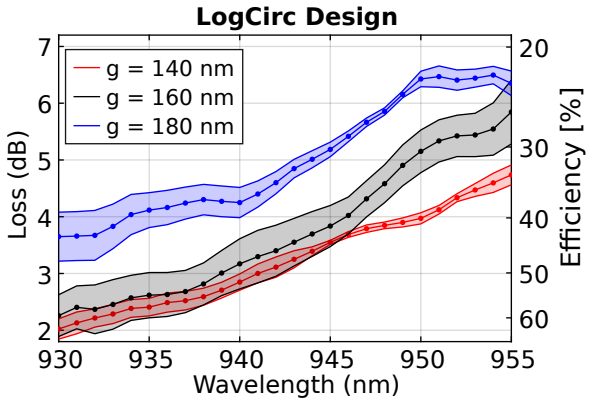

Figure 7.11: Wavelength-dependent insertion loss per slot waveguide for the LogCirc Design

wl	Simulated		CTL 950 nm		SuperK 950 nm	
	Eff [%]	dB	Eff [%]	dB	Eff [%]	dB
Pcirc						
140 nm	79.33	-1.01	78 ± 4	-1.1 ± 0.2	70.9 ± 1.9	-1.5 ± 0.1
160 nm	75.97	-1.19	76 ± 3	-1.2 ± 0.2	74.8 ± 3.8	-1.3 ± 0.2
180 nm	72.81	-1.378	71 ± 3	-1.5± 0.3	71.0 ± 1.4	-1.5 ± 0.1
DoubleLog						
140 nm	94.7	-0.24	69 ± 3	-1.6 ± 0.2	63.8 ± 3.9	- 1.95± 0.26
160 nm	93.2	-0.31	69 ± 3	-1.6 ± 0.2	61.9± 1.1	-2.1 ± 0.1
180 nm	91.3	-0.39	64 ± 4	-1.9 ± 0.3	64.9 ± 2.5	-1.9 ± 0.2
LogCirc						
140 nm	94.7	-0.24	59 ±3	-2.3 ± 0.2	63.3±0.7	-1.99 ± 0.05
160 nm	93.1	-0.31	63 ± 3	-2.0 ± 0.2	55.3 ± 2.4	-2.6 ± 0.2
180 nm	91.3	-0.39	51 ± 0.8	-2.90 ± 0.07	47.7 ± 0.8	-3.21 ± 0.07

Table 7.2: Comparison of simulated and measured efficiency and loss of a single coupler for λ =950 nm.

through the slot waveguide. This can be seen in Table 7.2. The efficiencies measured with respectively the CTL and SuperK lasers are in reasonable agreement and follow the same tendencies, albeit the SuperK measurements tend to have a lower efficiency than the CTL measurements. This can be explained by the fact that whereas the alignment on the measurements utilizing the CTL laser is optimized for a wavelength of $\lambda = 950\,\text{nm}$. As the Shallow Etch gratings have a wavelength-dependent optimal incident angle, the measurements taken utilizing the SuperK cannot have the optimal incident angle over the entire spectrum.

It can be seen how the losses of the ParamCirc design are mostly consistent with the simulated values, while the losses of the DoubleLog and LogCirc designs differ greatly. A likely explanation is that the design for the slab waveguide tapering into a slot waveguide cantilever, which is the same for the DoubleLog and LogCirc designs, features a sharp bend. This sharp crease in the feature might fail to faithfully reproduce during fabrication, leading to a sub-optimal geometry with significant loss.

7.5 Phaseshift characterization

To characterize the displacement-induced phase shift in the slot waveguide, MZIs containing a tuneable phase shifter in one arm were designed. Fig. 7.12 shows a SEM of the finalized device used for characterizing the voltage dependence of the NOEMS phase shifter, which consists of an MZI with two passive 50/50 beam splitters and Shallow Etch Gratings (SEG) for chip-to-fiber coupling. The arm not containing the NOEMS phase shifter contains a passive slot waveguide, which improves the splitting ratio as it offsets the insertion loss of the phase shifter, at the cost of an overall higher insertion loss.

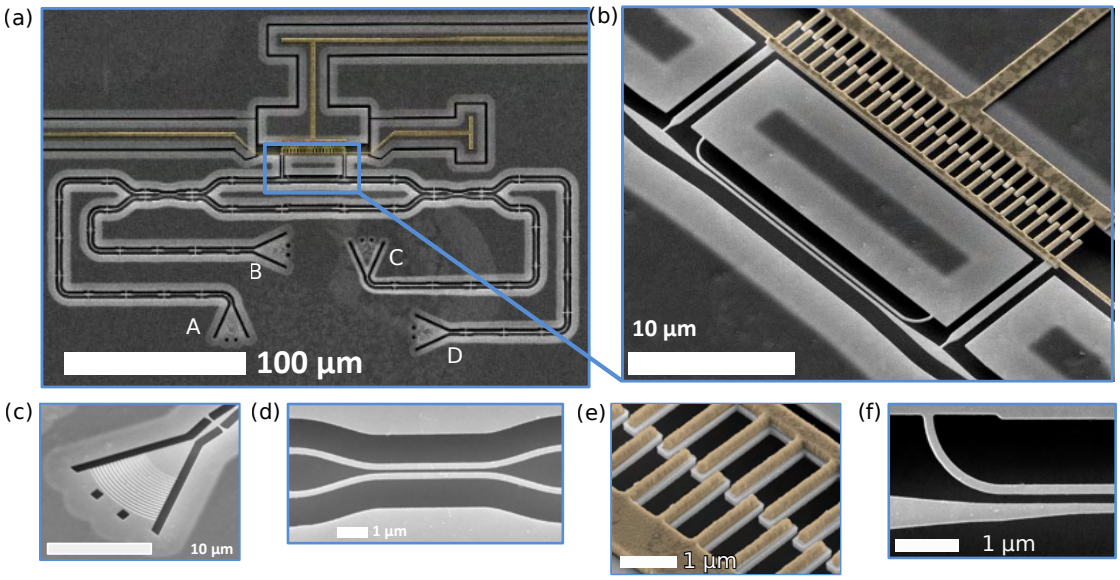

Figure 7.12: a: SEM of MZI containing a NOEMS phase shifter. b: Close up of NOEMS phase shifter device. c: Close up of SEG. d: Close up of passive 50/50 beam splitter e: Close up of comb. f: Close up of slot waveguide coupler.

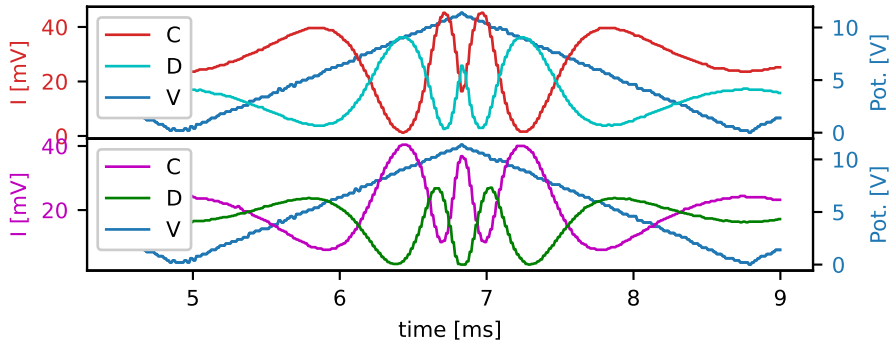

Figure 7.13: Raw data at room temperature for wavelength $\lambda = 950.25\,\text{nm}$ for one full cycle of the triangular pulse. Top row is data taken with the laser light focused on SEG grating A, as seen in Fig. 7.12(a). Bottom row is data taken with the laser light focused on SEG grating B. The data labeled C (D) refers to data collected from grating C (D).

7.5.1 Phase Shift at 293K

After the sample is placed in the cryostat, a CTL, whose power is controlled by a PID, is aligned to one of the grating couplers with the help of an imaging camera. On both the excitation path and the collection path, the polarization is controlled with a set of waveplates. A polarizing beam splitter splits the light in the collection path into two separate paths depending on their polarization, only one of which is shown in Fig. 7.2. By connecting the collimators at the end of those paths to the laser, the collection path is aligned to both output gratings of the device. Following this, each of the

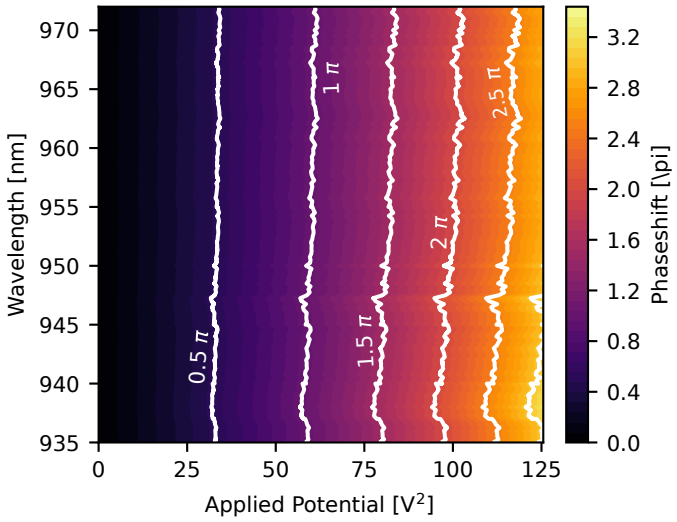

Figure 7.14: Voltage and wavelength-dependence of the phase shift at room temperature.

collimators is routed into a Thorlabs APD 130A/M avalanche photodetector allowing the intensity of the two output paths to be simultaneously measured with a Rigol DS1104Z Oscilloscope. The applied potential is controlled using a Rigol DG1032Z Arbitrary Waveform Generator. In order to prevent device breakdown from electrostatic discharges (ESD) a triangular waveform whose amplitude is ramped by $< 1\,\mathrm{V/s}$ in intervals of 100 mV is used. As the function generator has a peak-to-peak voltage of 20 V (-10 to 10 V), a Thorlabs MDT694 B piezo controller is used to obtain voltages larger than 10 V. This, however, has the disadvantage of severely limiting the maximum frequency, as hysteretic behavior will take place for high frequencies. Using a Python script to initialize the experiment, an interval of desired wavelengths is defined, and the wavelengths are swept over one by one. Once the CTL is adjusted to the desired wavelength, the oscilloscope measures the light collected in the collimators and saves the measured intensities. Following that, the CTL is set to the next wavelength. As the optimal coupling angle for an SEG depends on the wavelength utilized, a single sweep spans an interval of approximately 5 nm. After that, the alignment of the collection and excitation path is slightly rearranged to ensure optimal coupling, and the experiment is repeated for the next wavelength interval. After two wavelength intervals are completed, the excitation path is realigned, and the intervals are repeated for the other input arm of the MZI. This strikes a balance between the laborious work of realigning the excitation path with the need for similar alignment on the collection path for measurements taken on the two different inputs. Both at room temperature and cryogenic temperatures, the wavelengths were swept over an interval corresponding to the bandwidth of the SEGs at that temperature. Raw data taken at room temperature can be seen on Fig. 7.13. The electric potential is swept between 1 and 1.55 V with a frequency of 236 Hz and is multiplied by a factor of 7.5 using a Thorlabs MDT694 B piezo controller.

Data analysis and fitting

The intensity of the fringes follows a sine function

$$I = A \cdot (0.5 + 0.5 \cdot \sin^2(\Delta\phi + \phi_0)) + d,, \tag{7.6}$$

where A is the amplitude of the modulated signal, and d is the signal at the minimum value, leading to a visibility of

$$\nu = \frac{I_{\max} - I_{\min}}{I_{\max} + I_{\min}} = \frac{A}{A + 2d}. \tag{7.7}$$

Given a specific change in the refractive index Δn_{eff}, the change in accumulated phase is as follows

$$\Delta\phi = \frac{2\pi\Delta n_{\text{eff}} L}{\lambda}. \tag{7.8}$$

As found in chapter 4, the gap dependence of n_{eff} in a slot waveguide is best described by a hyperbolic cotangent,

$$n_{\text{eff}}(g) = a_n \cdot \coth(b_n \cdot g + c_n) + d_n. \tag{7.9}$$

Here the gap is described with the following function

$$g(V) = g_{\text{init}} - b_{\text{comb}} \cdot V^2, \tag{7.10}$$

where g_{init} is the initial gap, and b_{comb} is a geometry-dependent coefficient describing the strength of the electromechanical actuation, which for the investigated geometry was found in chapter 4 to be $b_{\text{comb}} = 0.65\,\text{nm/V}^2$.

The cantilevers of the utilized device are 170 nm wide. When carrying out the slot waveguide characterization in chapter 4, the gap dependence of n_{eff} of the guided quasi-TE guided mode with a wavelength $\lambda = 950$ nm in a GaAs ($n = 3.45$) slot waveguide with a cantilever width of 170 nm was found to be

$$n_{\text{eff}}(g) = 0.0917 \cdot \coth(2.32 \cdot 10^{-3}\,\text{nm}^{-1} \cdot g + 0.0954) + 1.2135. \tag{7.11}$$

Identifying A, ϕ_0 and d of Eq. 7.6 as well as b_n and c_n of Eq. 7.9 as fitting parameters, while using wavelength-dependent values found in chapter 4 for a_n and d_n of Eq. 7.9, the potential and wavelength-dependence of the phase shift is fitted as seen in Fig. 7.14. The x-axis of the plot is the square of the applied potential which is proportional to the actuation distance, showing a strong, non-linear relationship between the displacement and the phase shift, as predicted in chapter 4. The phase-shifter exhibits broadband behavior, with an investigated range of 38 nm, limited by the bandwidth of the utilized SEGs.

Focusing on a single wavelength $\lambda = 950$ nm, Fig. 7.15 shows the intensity fringes taken from a single measurement, compared with the fit. The origin of the discrepancy between the magnitudes at high and low applied potential of the path labeled R is unknown, but could result from the coupler having a lower loss at smaller gaps, as measured in chapter 7.4, which again leads to a higher visibility of the interferometer, as calculated in chapter 3. For output path R, the visibility for the first (second) set

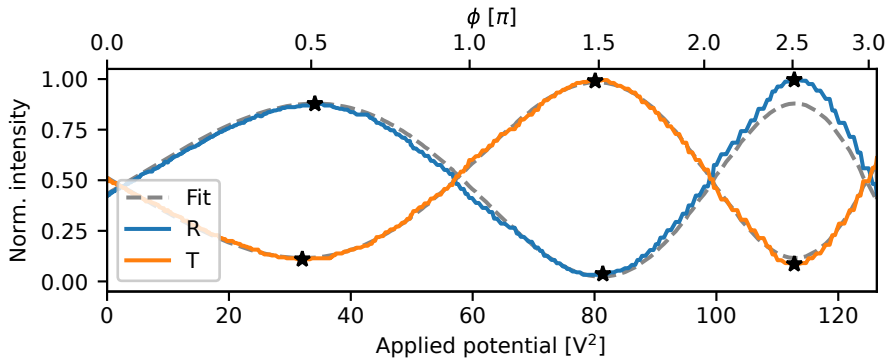

Figure 7.15: Intensity fringes fitted at room temperatures for a wavelength $\lambda = 950\,\text{nm}$. Black stars indicate extrema.

	R	T
$V_\pi L$, first π	$7.71 \cdot 10^{-3}$	$7.73 \cdot 10^{-3}$
$V_\pi L$, peak-to-peak 1	$3.18 \cdot 10^{-3}$, $V_b = 5.84\,\text{V}$	$3.29 \cdot 10^{-3}$, $V_b = 5.66\,\text{V}$
$V_\pi L$, peak-to-peak 2	$1.60 \cdot 10^{-3}$, $V_b = 9.02\,\text{V}$	$1.67 \cdot 10^{-3}$, $V_b = 8.95\,\text{V}$

Table 7.3: Half-wave-voltage length product, $V_\pi L$ for $\lambda = 950\,\text{nm}$. $V_\pi L$, first π utilizes the V needed to obtain a π phase shift from zero actuation. $V_\pi L$, peak-to-peak 1 (2) uses the value of V needed to modulate the intensity from the first (second) observed extrema to the second (third), with application of a bias V_b. All values of $V_\pi L$ are in units of $\text{V} \cdot \text{cm}$.

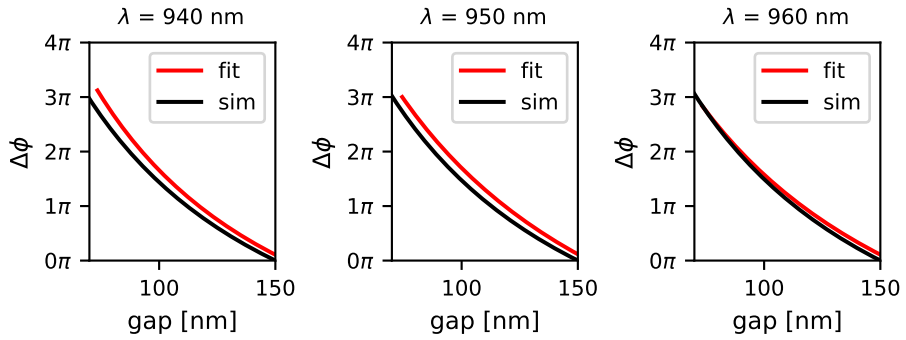

Figure 7.16: Comparison between the gap-dependence of the simulated phase shift and the phase shift derived from fitting the interference fringes, assuming the same voltage-dependence of the displacement as found in the simulation.

of extrema is $\nu_{R,1\,(2)} = 0.92(0.93)$, while the first (second) visibility value for output path T is $\nu_{T,1\,(2)} = 0.80(0.84)$.

The half-wave-voltage length product, $V_\pi L$, an important figure of merit for electrically actuated phase shifters, can be seen in Table 7.3. It can be seen how for a sample wavelength of $\lambda = 950\,\text{nm}$, upon application of a pre-bias of $\sim 9\,\text{V}$, a switch between two extrema can be carried out with an additional voltage as low as $V_\pi = 1.6 \cdot 10^{-3}\,\text{V}$, yielding $V_\pi L = 1.6 \cdot 10^{-3}\,\text{V} \cdot \text{cm}$. From zero actuation, a half-wave-voltage length product $V_\pi L = 7.7 \cdot 10^{-3}\,\text{V} \cdot \text{cm}$ was found.

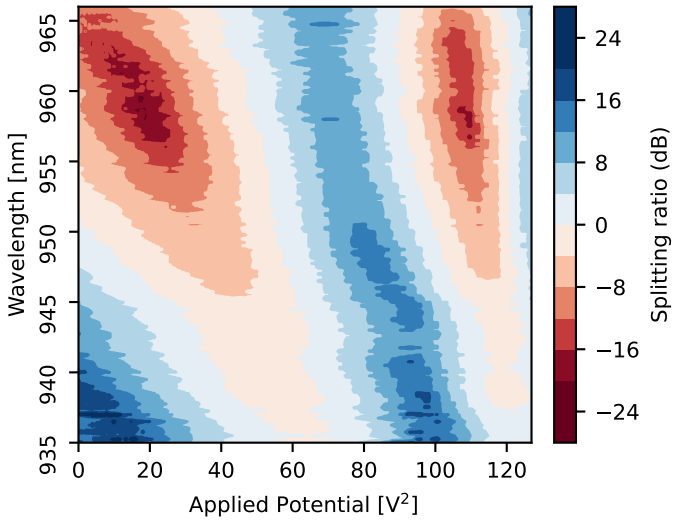

Figure 7.17: Splitting ratio of the Mach-Zender-Interferometer as a function of the wavelength and applied potential.

Fig. 7.16 shows the phase shift plotted against the gap, for a GaAs slot waveguide with an initial gap $g_{\text{init}} = 150\,\text{nm}$. The gap dependence of the phase shift obtained from the simulation, and the phase shift obtained by fitting the interference fringes, are compared. For the experimental result, the voltage dependence of the displacement is assumed to be $g(V_p) = 150\,\text{nm} - 0.65\,\text{nm/V}^2 \cdot V_p^2$, where V_p is the applied potential. The fitted phase shifts obtained from the measurement are in good agreement with the simulated phase shifts for the three investigated wavelengths, suggesting that the displacement of the slot waveguide is consistent with the simulated value.

While a simple splitting ratio can be calculated as $SR_{\text{simple}} = R/T$, it does not take coupling efficiencies into account. The different in- and out-coupling paths of the MZI have different lengths, leading to different losses. Additionally, it cannot be assumed that the coupling efficiency of every single element in the two collection paths is the same. A general term for the inputs and outputs of a beam splitter with a coupling efficiency η_i on the i'th path can be written as

$$\begin{bmatrix} I_C \\ I_D \end{bmatrix} = \begin{bmatrix} \eta_A \eta_D T & \eta_B \eta_D P \\ \eta_A \eta_C R & \eta_B \eta_C \tau \end{bmatrix} \begin{bmatrix} I_A \\ I_B \end{bmatrix}. \tag{7.12}$$

By sending the same light intensity I into either path A or path B, the outgoing intensities can be labeled $I_{ij} = \eta_i \eta_j \mathbf{B}_{ij}$, where $\mathbf{B}_{ij}$ is the ij'th index of the beam splitter matrix $B = \begin{bmatrix} T & P \\ R & \tau \end{bmatrix}$. From here, a coupling efficiency-independent expression for the splitting ratio can be written out as

$$SR = \sqrt{\frac{I_{AD} I_{BC}}{I_{AC} I_{BD}}} = \sqrt{\frac{T\tau}{RP}} \tag{7.13}$$

Fig. 7.17 shows the measured splitting ratio at room temperature, exhibiting wavelength- and voltage-dependent fringes. A likely explanation for the origin of

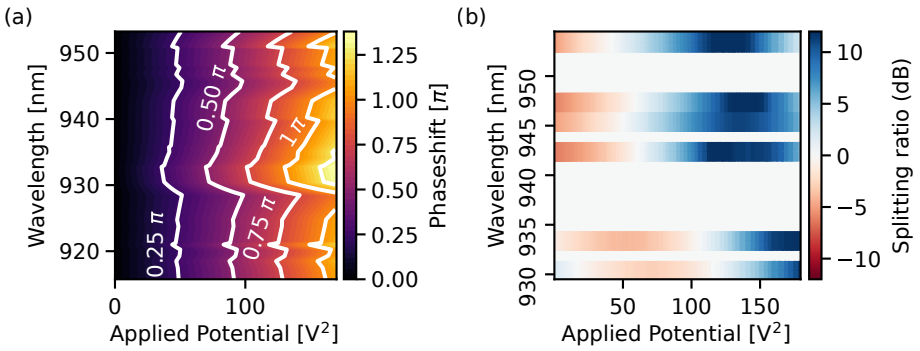

Figure 7.18: a: Voltage- and wavelength-dependence of the phase shift at 10 K. b: Voltage- and wavelength-dependence of the splitting ratio at 10 K. Due to an bug in the measurement software, the data taken at 10 K was lost for some wavelengths.

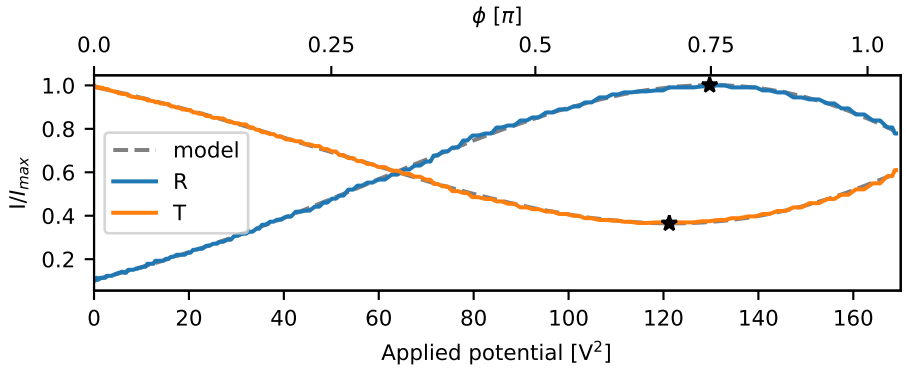

Figure 7.19: Intensity fringes fitted at room temperatures for a wavelength $\lambda = 924\,\text{nm}$. The maximum obtained phase shift is $\Delta\phi_{max} = 1.05\pi$

the wavelength-dependent variation in the intensity of the fringes is that the splitting ratio of the passive beam splitters is wavelength-dependent, leading to a visibility of the MZI which changes depending on the wavelength.

7.5.2 Phase shift at 10K

Following characterization at room temperature, a characterization at cryogenic temperatures was carried out. The sample was cooled down to 10 K in a He flow cryostat while keeping $dT < 8\,\text{K/min}$. Fig. 7.18(a) shows the wavelength- and voltage-dependence of the phase shift at 10 K, measured on the same device as the data taken at room temperature. At cryogenic temperatures, the same voltage yields a significantly lower phase shift. Compared to room temperatures, where phase shifts of $\sim 3\pi$ are obtained for a maximum applied potential of $V_{\text{max, RT}} = 11.6\,\text{V}$, the measurements taken at cryogenic temperatures on the same device obtain phase shifts in the order of $\sim \pi$ while using a maximum applied potential of $V_{\text{max, 10 K}} = 13.8\,\text{V}$.

Figure 7.19 shows a comparison of the measured and fitted interference fringes plotted against the square of the applied potential for $\lambda = 924\,\text{nm}$. The half-wave-

	R	T
$V_\pi L$, first π	$12.4 \cdot 10^{-3}$	$12.4 \cdot 10^{-3}$

Table 7.4: Half-wave-voltage length product $V_\pi L$ for $\lambda = 924\,\text{nm}$ at cryogenic temperatures ($\sim 10\,\text{K}$). $V_\pi L$, first π utilizes the V needed to obtain a π phase shift from zero actuation in units of $\text{V} \cdot \text{cm}$

voltage length product, $V_\pi L$, of the R and T paths of the phase shifter at $T = 10\,\text{K}$ for $\lambda = 924\,\text{nm}$ is shown in Table 7.4. Despite this value being significantly larger than at room temperature, it is still competitive compared to other values found in the literature. Splitting ratios for the MZIs at 10 K can be seen on Fig. 7.18(b). The splitting ratio is much less pronounced than at room temperature. One possible explanation is additional asymmetry between the arms of the MZI, due to the motor cantilever of the slot waveguide being displaced by approximately $-60\,\text{nm}$ in the z-direction, as seen in 6.2.1. The passive arm of the MZI is also equipped with a slot waveguide, which balances the losses of the two arms, improving the visibility and splitting ratio as calculated in section 3.1.2. However, the displacement of the motor cantilever is caused by mismatches of the thermal expansion coefficients between GaAs and the Au utilized in the comb drive. As the simple slot waveguide in the passive arm of the MZI is not connected to a comb drive actuator, it will not undergo a similar displacement.

Investigation of the discrepancy of actuation between room temperature and 10 K.

Investigating the origin of the different phase shifts for the phase shifter at room and cryogenic temperatures is of great interest, because, ideally, the electrical, optical, and mechanical properties of NOEMS are not significantly affected by temperature. The small change in the index between room and cryogenic temperatures makes it unlikely that the smaller phase shift change at cryogenic temperatures is caused by changes in the material refractive index. At $\lambda = 940\,\text{nm}$, the material refractive indices at respectively room and cryogenic temperatures are $n_{\text{GaAs},\,295\,\text{K}} = 3.51$ and $n_{\text{GaAs},\,4\,\text{K}} = 3.46$ [175].

Another possibility to investigate whether the displacement of the slot waveguide decreases at low temperatures. Research shows that the elastic constants of GaAs do not vary significantly between cryogenic and ambient temperatures [176]. Gold, however, exhibits significantly different elastic moduli at room and cryogenic temperatures. The exact value of the elastic properties of gold thin films varies significantly in the literature [177], and little research has been carried out specifically comparing the difference in elastic properties of gold at room and cryogenic temperatures. Despite this, it has been shown that the modulation of MEMS devices utilizing gold thin films can be impeded at cryogenic temperatures [178]. Assuming that the lower phase shift is entirely due to a smaller displacement of the comb drive, Eq. 7.10 is reformulated as

$$g(V) = g_{\text{init}} - c_V b_{\text{comb}} \cdot V^2, \tag{7.14}$$

where $0 < c_V < 1$ is a coefficient that accounts for the reduced displacement at low

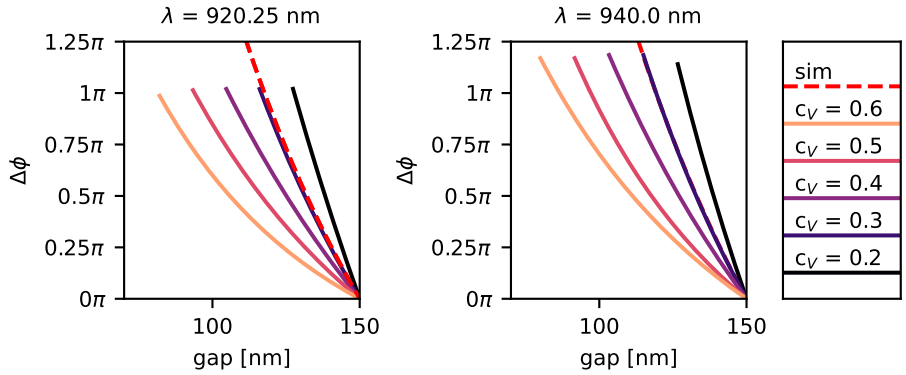

Figure 7.20: Induced phase shift as a function of the calculated gap while sweeping over c_V for a slot waveguide with $g_{\text{init}} = 150\,\text{nm}$, for $\lambda = 920.25\,\text{nm}$ (left) and $\lambda = 940\,\text{nm}$ (right), compared to the simulated value.

temperatures. This gives the following fit function for the effective refractive index,

$$n_{\text{eff}}(g) = a_n \cdot \coth(b_n(g_{\text{init}} - c_V b_{\text{comb}} \cdot V^2) + c_n) + d_n. \tag{7.15}$$

The function inside the coth term, $b_n(g_{\text{init}} - c_V b_{\text{comb}} \cdot V^2) + c_n$ yields three parameters to fit (b_n, c_n and c_V) under the assumption that g_{init} and b_{comb} are fixed, while being a polynomial containing a second-order and a constant term. By fitting for b_n and c_n while sweeping over values of c_V, the relation between the applied voltage and phase shift can be found. The fitted value of $g(V)$ is calculated for each value of c_V, and the phase shift is found by fitting the interference fringes against the calculated $g(V)$, as seen in Fig. 7.20. By comparing this to the simulated values of $\Delta\phi$ for a given gap, which should remain close to unchanged at cryogenic temperatures as the optical properties remain almost unchanged, an estimated value of $c_V = 0.3$ can be identified, corresponding to the displacement at $T = 10\,\text{K}$ being roughly 30% of the displacement at $T = 293\,\text{K}$. Nonetheless, $\Delta\phi(V)$ remains robust to the choice of c_V, with the maximum phase shift for $\lambda = 920.25\,\text{nm}$ being $\Delta\phi_{920.25\,\text{nm}}(V_{\text{max}}) = (1.01 \pm 0.01)\pi$ and the maximum phase shift for $\lambda = 940\,\text{nm}$ being $\Delta\phi_{940\,\text{nm}}(V_{\text{max}}) = (1.17 \pm 0.02)\pi$.

For other NOEMS devices on the same GaAs platform, it has been found that the frequency of the fundamental mode is approximately 41% higher at cryogenic temperatures than at room temperature [179]. Equation 4.3 in section 4.2 states that the fundamental eigenfrequency of a thin, unstressed beam is

$$f = \frac{1}{4\pi}\frac{w}{L^2}\sqrt{\frac{E}{\rho}}. \tag{7.16}$$

This implies that at low temperatures, the elastic coefficient is roughly twice as large as at room temperatures, $E_{10\,\text{K}} \approx 1.41^2 E_{293\,\text{K}} \approx 2E_{293\,\text{K}}$, assuming that neither the dimensions of the device nor the density of the material change significantly. This change in elastic properties could be an intrinsic property of the thin film, or a stiffening induced by the thermal stress in the gold layer.

Year		Mat.	Type	Dev	λ [nm]	Length	$V_{pi}L$ [V · cm]	IL [dB]	Speed
2025	This work	GaAs	NOEMS	ϕ	950 924	10 µm	$7.7 \cdot 10^{-3}$ (RT) $12 \cdot 10^{-3}$ (10 K)	2.4	2.8 µs*
2024	[180]	GaAs	NOEMS	ϕ	930	10 µm	0.04 (RT)		
2017	[115]	GaAs	EO	ϕ	920	400 µm	0.1 (10 K)	> 3	55 ns
2019	[27]	GaAs	NOEMS	BS	940	26 µm	0.026 (10 K)	0.67	1 µs
2023	[29]	Si	NOEMS	ϕ	1550	100 µm	0.075	0.14	18.1 µs
2022	[181]	SiN	NOEMS	ϕ	1550	250 µm	0.15 (1.5 K)	0.5	1.29 µs**
2021	[31]	SiN	NOEMS	ϕ	1550	210 µm	0.042	0.47	1.13 µs**
2021	[32]	Si	NOEMS	ϕ	1550	25 µm	$2.1 \cdot 10^{-4}$	0.04	10 µs**
2021	[28]	Si	NOEMS	ϕ	1550	17.2 µm	$18.1 \cdot 10^{-3}$	0.33	2 µs***

Table 7.5: Comparison of figures of merit for respectively reconfigurable GaAs circuits, and recent NOEMS phase shifters in integrated photonics. Temperature is noted whenever mentioned. * Estimated from 1/(resonance frequency). Resonance frequency is lowest eigenfrequency obtained in COMSOL utilizing an unstrained geometry identical to the one used in section 4.2.3. ** Estimated from 1/(resonance frequency) *** Rise time.

As, for small displacements, an electromechanical actuator follows Hooke's law $F = kx$, a twofold increase in the elastic constant should halve the displacement for a given electric potential. The reason the comb drive devices exhibit an even smaller displacement at cryogenic temperatures is likely due to a combination of different device geometries containing larger gold areas compared to the devices described in [179] and fluctuations during the fabrication procedure causing changes in the material intrinsic strain. Another factor contributing to the lower phase modulation at cryogenic temperatures could be the comb drives experiencing a moderate vertical displacement at low temperatures, as shown in Fig. 6.4, leading to a lower electrostatic force for a given applied potential. The ~ 60 nm negative vertical displacement of the motor cantilever of the slot waveguide, as seen in Fig 6.3, could also lead to a lower phase shift for a given displacement of said cantilever due to said displacement of the phase shifter leading to a larger effective gap in the slot waveguide.

7.5.3 Comparison to state of the art

This thesis aims to fill a research gap, as little research has been carried out into the topic of optical phase shifting on a GaAs platform. Earlier research from this group has investigated photon routing using the Pockels effect with a phase shifter inserted in one arm of an MZI, where $V_\pi L = 0.1\,\mathrm{V \cdot cm}$ [115]. Furthermore, a NOEMS beam splitter, where $V_\pi L = 0.026\,\mathrm{V \cdot cm}$ has been demonstrated [27]. A preliminary result for this thesis, reported in [180], obtained $V_\pi L = 0.04\,\mathrm{V \cdot cm}$ at room temperature. The significantly improved performance in the current result is attributed to the implementation of a more effective design of the comb drives. Table 7.5 compares the work carried out in this thesis to a selection of recently published mechanically actuated slot waveguide phase shifters. With a length of only 10 µm, the device reported on

in this thesis is the shortest reported on, and also has the lowest value for $V_\pi L$ at both room and cryogenic temperatures, except for the remarkable result reported in [32]. This work features a double slot waveguide consisting of three beams, the two outer of which are respectively p- and n-layer. These two outer beams are pulled towards each other when a voltage difference is applied, allowing a half-wave voltage $V_{pi} = 0.850\,\mathrm{V}$. While the response speed of the device has not been experimentally characterized, the eigenfrequencies of an unstrained geometry identical to the one used for the simulation of the electromechanical response in section 4.2.3 were found using COMSOL. The fundamental eigenfrequency, as found in the simulation, was $f_0 = 358\,\mathrm{kHz}$. This indicates a response time in the single-digit microsecond range, which might experience an additional decrease at cryogenic temperatures where a significant increase of the eigenfrequency can be expected [179] A glaring disadvantage, compared to the other phase shifters in Table 7.5, is the high insertion loss of the phase shifter, and the design and fabrication of a slot waveguide phase shifter with a lower insertion loss should be the main priority for further research seeking to improve the performance of the phase shifter.

7.6 Connection and outlook

To conclude, this section demonstrated a compact phase shifter by electromechanically routing the gap of a slot waveguide. At room temperature, the device exhibits a half-wave-voltage length product of $V_\pi L = 7.7 \cdot 10^{-3}\,\mathrm{V \cdot cm}$ from zero actuation, with peak-to-peak switching possible with a switching voltage of $1.6\,\mathrm{V}$ upon application of a bias $V_b = 9\,\mathrm{V}$. At cryogenic temperatures, the actuation is significantly smaller due to significant stiffening of the gold film used for the slot waveguide. Nonetheless, a competitive $V_\pi L = 0.012\,\mathrm{V \cdot cm}$ from zero actuation is demonstrated.

A main drawback to the device is the high insertion loss, which for a slot waveguide with gap $g = 160\,\mathrm{nm}$ was measured to be $L_{\mathrm{in}} = -2.4 \pm 0.2\,\mathrm{dB}$, which was in good agreement with the simulated insertion loss $L_{\mathrm{in,\,sim}} = -2.4$. While two designs promising coupling efficiencies above 90% were fabricated, the measured insertion losses were $> 3\,\mathrm{dB}$. This large discrepancy between simulation and measurement was likely due to the presence of sharp edges, which failed to be reproduced during fabrication. Improvement of the coupling efficiencies could be obtained by optimizing the tapering of the coupler. Furthermore, a slight width difference between the cantilevers of the slot waveguides, with the wider of the two cantilevers tapering into the slab waveguide, can improve the coupling efficiency of the slot waveguide.

With the phase shifter introduced, and its properties characterized, the next chapter covers the slot waveguides being used to modulate the effective optical path length between a quantum dot and a distant mirror ($d \approx 40\,\mu\mathrm{m}$). This changes the local density of optical states (LDOS) at the location of the quantum dot, allowing for control of quantum dot properties such as lifetime and intensity.

Chapter 8

Control of QD emission with a Distant Mirror

The research described in this chapter is covered in a publication under preparation, and a large part of the text and figures is reproduced from the manuscript with minor adjustments.

Quantum dots acting as single photon emitters are essential resources for the realization of quantum photonic integrated circuits with near-deterministic single-photon sources and spin-photon interfaces [182, 183, 184]. A known issue towards scaling up the number of emitters that can be simultaneously controlled in an integrated photonic circuit is to reliably achieve optimal spatial alignment between the guided modes and quantum dot transition dipoles. A widely used approach to circumvent spectral and spatial randomness is to precharacterize the emitters prior to device fabrication, which allows for the identification of suitable candidates that can be subsequently aligned to nanostructures [86]. These methods rely on ultra-precise fabrication and imaging methods to guarantee precise alignment and pose constraints on the design of photonic integrated circuits. An alternative approach explored here is to provide reconfiguration of the emitter-field coupling by modifying the LDOS directly via remote control. Using a novel design where a phase shifter is placed between a quantum dot and a photonic crystal mirror, the possibility of using a phase shifter to change the effective optical path length to the mirror is investigated. This changes the LDOS, which in turn changes the decay dynamics and the intensity of the light emitted by the quantum dot.

8.1 Spontaneous emitters and local density of states

The ground state, $|g\rangle$ and excited state, $|e\rangle$, of a two level system (TLS) are considered orthogonal. As their wave functions have zero overlap, spontaneous emission should be impossible according to the laws of traditional quantum mechanics. Neither have classical electrodynamics managed to provide a satisfactory description of the phenomena of spontaneous emission [185]. Yet spontaneous emission, which is the origin of most photons around us, is evidently not only possible, but plentiful.

The flawed description was happening due to an oversight in the mathematical formulation of an excited emitter in the absence of an electric field. By considering the ever-present fluctuations of a vacuum field, which couples the two states of the TLS [186], a mathematical description of spontaneous emission was derived. As spontaneous emission is thus not solely a property of the emitter, but an interaction of an excited emitter with its surroundings, it is sensible that the shape and nature of the surrounding environment should influence the emission properties. By engineering the surroundings of the emitter, the local density of states (LDOS) can be enhanced or suppressed compared to a free-space emitter [87].

In the 1960's and 70's, it was discovered that by placing a mirror close to an emitter, it was possible to not only influence the intensity of the light, which is modulated due to a standing wave between the emitter and the mirror, but also the lifetime of the state, which changes to the influence on the (LDOS). While the Purcell effect in microcavities, where the cavity length can suppress or enhance states by controlling the LDOS and thus the vacuum fluctuations, had been known since the 1940s [187], the control of the LDOS outside a cavity system was first demonstrated by Drexhage in 1966. Drexhage and his colleagues found that by placing a mirror close to a fluorescing molecule, both the angular distribution of the fluorescence and the decay time of the molecule could be controlled by actuating the distance to the mirror [188]. This fluorescence was found to have a strong dependence on the angle of incidence between the emitted light and the mirror. This actuation of the lifetime, however, strongly declined as the mirror was moved further away from the fluorescent molecule, with the effect vanishing almost completely at just a few wavelengths' distance.

In this section, a similar system is utilized. A small device consisting of a SEG, a phase shifter, and a photonic crystal mirror is created. By exciting a quantum dot located in between the SEG and the phase shifter, single photons can be emitted. By tuning the phase shifter, the effective path length between the emitter and the photonic crystal mirror can be actuated, allowing control of both the intensity measured at the SEG and the quantum dot lifetime. Due to the light being confined in the quantum dot, the visibility of the light when the effective path length is changed by a single effective wavelength is not dependent on the distance between the emitter and the mirror, allowing nonlocal control of the emitter properties over a large distance $L > 40\,\mu\text{m}$.

8.1.1 Intensity modulation of a quantum dot in a 1D system

Fig. 8.1(a) shows the concept of the experiment described in this section. A waveguide, which contains a quantum dot excited by a laser, is terminated by a movable mirror. By changing the distance between the mirror and the quantum dot, the electric field and the local density of states are both changed, which influence the emitted light from the quantum dot. Fig. 8.1(c) shows the physical implementation of the experiment, where the waveguide is terminated with a photonic crystal mirror, the effective distance to which is modulated using a nanomechanical phase shifter.

The waveguide is oriented along the x-axis. The mirror has reflectivity r, and is located at $x = L$, the slot waveguide has transmittivity $t_s e^{i\phi}$ and can apply a controllable

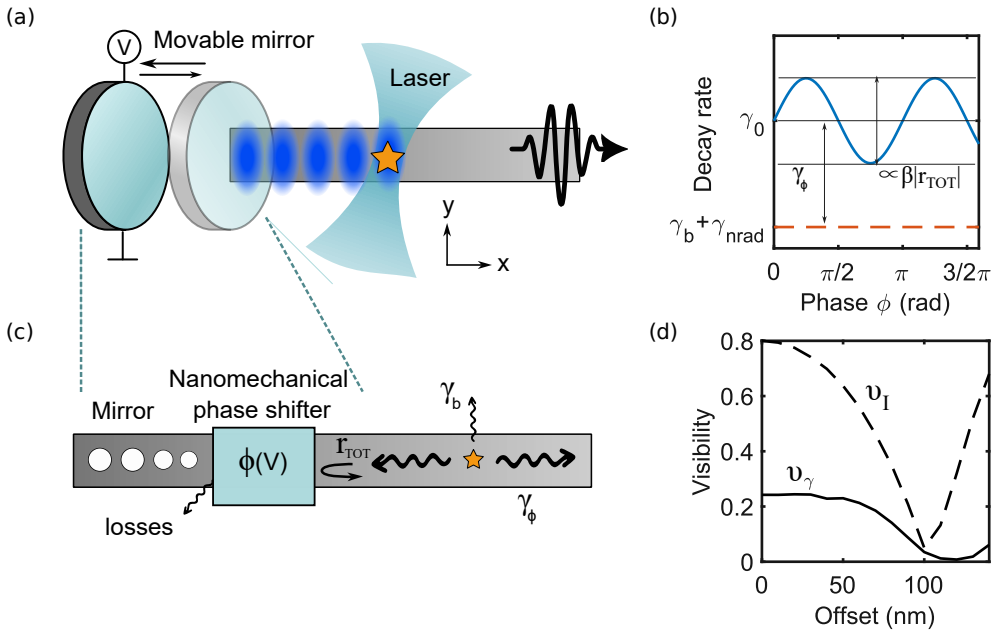

Figure 8.1: One-dimensional implementation of the Drexhage experiment. a: Schematic of a waveguide with a movable mirror on one end, enabling the control of the LDOS at the location of a distant QD. b: Expected phase-dependent modulation of decay rate in the presence of mirror reflectivity r_{tot}, background radiation γ_b and non-radiative decay rate γ_{nrad}. c: Experimental realization with a fixed photonic crystal mirror and a NOEMS phase shifter. d: Calculated visibilities for intensity (ν_I) and decay rate (ν_γ) as a function of the offset from the waveguide center assuming $r_{\text{tot}} = 0.5$ and above-band excitation.

phase ϕ, and the waveguides have transmittivity t_w. The system can thus be considered to have a total reflectivity $r_{\text{tot}} = |t_s^2 t_w^2 r| \exp(2i\phi)$. Setting an electric field from the source, $\mathbf{E}(x, y_0, z_0) = \mathbf{E}(y_0, z_0)e^{-ikx}$, the total electric field at the position of the emitter is

$$\mathbf{E}_{tot}(0, y_0, z_0) = \mathbf{E}(y_0, z_0) + |r_{\text{tot}}|\mathbf{E}^*(y_0, z_0)e^{-2i(kL+\phi)}. \tag{8.1}$$

Here the first term is the field emitted from the source, and the second is a mirror field. In a rectangular waveguide with QDs located in the middle, i.e. z = 0, the transverse electric field can be approximated as a linear combination of purely real eigenfunctions $e_x(y)$ and $e_y(y)$,

$$\mathbf{E} = e_x(y)\hat{\mathbf{x}} + ie_y(y)\hat{\mathbf{y}}, \tag{8.2}$$

with intensity being

$$I = \frac{cn\varepsilon_0}{2}|E|^2. \tag{8.3}$$

Due to the nature of the quantum dots grown on the GaAs substrate, their electric dipole can be oriented either along the $x-$ or the y-axis. This leads to the following expressions for the light radiated by respectively an x-dipole

$$I_{x/y} = \frac{cn\varepsilon_0}{2}|e_x(y)|^2 \left[1 + |r_{\text{tot}}|^2 \pm 2|r_{\text{tot}}|\cos(2\phi + \theta)\right], \tag{8.4}$$

where $\theta = 2kL$ is a fixed phase depending on the optical distance between the emitter and the mirror. Similarly, in the absence of a mirror the intensity is

$$I_{0,x/y} = \frac{cn\varepsilon_0}{2}|e_{x/y}|^2. \tag{8.5}$$

This leads to the following intensity modulation

$$\frac{I_{x/y}}{I_{0,x/y}} = \frac{1}{2}\left(1+|r_{\text{tot}}|^2 \pm 2|r_{\text{tot}}|\cos(2\phi)\right). \tag{8.6}$$

If the collected light originates from just a single dipole, the visibility is as follows

$$\begin{aligned} V &= \frac{\max(I_{x/y})-\min(I_{x/y})}{\max(I_{x/y})+\min(I_{x/y})} = \frac{(1+|r_{\text{tot}}|^2+2|r_{\text{tot}}|)-(1+|r_{\text{tot}}|^2-2|r_{\text{tot}}|)}{(1+|r_{\text{tot}}|^2+2|r_{\text{tot}}|)+(1+|r_{\text{tot}}|^2-2|r_{\text{tot}}|)} \\ &= \frac{2|r_{\text{tot}}|}{1+|r_{\text{tot}}|^2}. \end{aligned} \tag{8.7}$$

However, if the quantum dots are excited with above band excitation, the visibility will contain components of both the x-dipole and the y-dipole. If the fine structure splitting of the dipoles is not resolved by the spectrometer, the light will contain two components given by

$$\begin{aligned} I_{tot} = \frac{cn\varepsilon_0}{2}\Bigg\{ &\left[|e_x(y)|^2+|e_y(y)|^2\right]\left(1+|r_{\text{tot}}|^2\right) \\ &+\left[|e_x(y)|^2-|e_y(y)|^2\right]\left(2|r_{\text{tot}}|^2\cos(2\phi+\theta)\right)\Bigg\}. \end{aligned} \tag{8.8}$$

Assuming that $e_x(y)$ has the larger magnitude of the two functions, this leads to

$$\min(I_{tot}) = |e_x(y)|^2(1+|r_{\text{tot}}|^2-2|r_{\text{tot}}|)+|e_y(y)|^2(1+|r_{\text{tot}}|^2+2|r_{\text{tot}}|), \tag{8.9}$$

$$\max(I_{tot}) = |e_x(y)|^2(1+|r_{\text{tot}}|^2+2|r_{\text{tot}}|)+|e_y(y)|^2(1+|r_{\text{tot}}|^2-2|r_{\text{tot}}|), \tag{8.10}$$

yielding a visibility

$$V_{tot} = \frac{2|r_{\text{tot}}|}{1+|r_{\text{tot}}|^2}\text{abs}\left|\frac{|e_x(y)|^2-|e_y(y)|^2}{|e_x(y)|^2+|e_y(y)|^2}\right|. \tag{8.11}$$

8.1.2 Lifetime modulation of a quantum dot in a 1D system

In the absence of a mirror, the total decay rate $\Gamma_{x/y,0}$ of the quantum dot emitting into either the x or the y dipole is

$$\Gamma_{x/y,0} = \gamma_{x/y,0}+\gamma_{x/y,b}+\gamma_{x/y,\text{nrad}}, \tag{8.12}$$

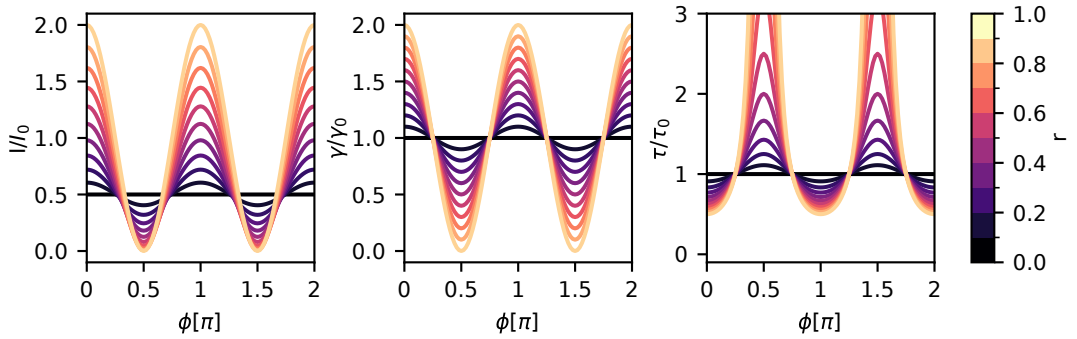

Figure 8.2: Phase- and reflectivity-dependent behavior of an emitter in a waveguide with a mirror. (a) Intensity modulation. (b): Decay rate modulation. (c): Lifetime modulation. The color of the plot corresponds to the reflectivity of the mirror, as seen on the colorbar to the far right.

where $\gamma_{x/y,0}$ is the rate of spontaneous emission into the waveguide, $\gamma_{x/y,b}$ is the decay rate due to coupling to leaky modes, and $\gamma_{x/y,\text{nrad}}$ is the decay rate due to non-radiative decay processes. Combined, they define a β-factor, which signifies the probability of a given excited quantum dot to emit into a guided mode, i.e.

$$\beta_{x/y,0} = \frac{\gamma_{x/y,0}}{\gamma_{x/y,0} + \gamma_{x/y,b}} = \frac{\gamma_{x/y,0}}{\Gamma_{x/y,0}}, \tag{8.13}$$

where $\gamma_{x/y,\text{nrad}}$ is disregarded due to typical values of $\gamma_{\text{nrad}} \simeq 0.1\ \text{ns}^{-1} \ll \gamma_{\text{rad}}$. Given the large distance between the emitter and the NOEMS phase shifter, it can be assumed that the background decay rate is independent of the phase shift.The spontaneous emission of a quantum emitter can be described in terms of Green's Tensor using Fermi's golden rule

$$\gamma = \frac{\pi\omega_A|\mathbf{d}|^2}{3\hbar\varepsilon_0}\rho(\mathbf{r}_0,\omega_A), \tag{8.14}$$

where $\rho(\mathbf{r}_0,\omega_A)$ is the partial local density of optical states (partial LDOS), ω_A is the energy between the ground state and excited state of the two-level system of the emitter, $\mathbf{d}$ is the transition dipole moment, $\mathbf{d} = \langle g|\hat{\mathbf{d}}|e\rangle$, and $\mathbf{r}_0$ the position of the emitter. Assuming we have a TE-mode, which has the largest electrical field in the polarization transverse to the waveguide (i.e. the y-axis), the perturbed decay rate of the quantum dot can be derived, as detailed in Appendix B

$$\frac{\gamma_{x/y,\phi}}{\gamma_{x/y,0}} = \frac{\rho_{x/y,\phi}}{\rho_{x/y,0}} = 1 - |r_{\text{tot}}|\cos(2\phi+\theta). \tag{8.15}$$

From here, the following equation for the total decay rate in presence of a mirror can be derived under the assumption that the waveguide light is in the TE mode

$$\Gamma_{x/y,\phi}(\phi) = \gamma_{x/y,\phi} + \gamma_{x/y,b} = \gamma_{x/y,0}\left(1 \pm |r_{\text{tot}}|\cos(2\phi+\theta)\right) + \gamma_{x/y,b}, \tag{8.16}$$

where it is assumed that $\gamma_{x/y,b}$ does not change in the presence of a mirror, and does not depend on ϕ. From this, the visibility of the total decay rate can be found to be

$$\nu\gamma = \beta_{x/y,0}|r_{\text{tot}}|. \tag{8.17}$$

These equations hold in the case of single dipole orientations in single-mode waveguides. However, the sample used for the experiment was grown on undoped GaAs, and the quantum dots were thus not gated. A non-resonant excitation scheme was carried out, which equally populates the two dipoles. This causes an effective decay rate that is the average of the rates for each of the two dipoles,

$$\Gamma_{\text{eff}}(\phi) = \frac{1}{2}\left(\Gamma_{x,\phi}(\phi) + \Gamma_{y,\phi}(\phi)\right). \tag{8.18}$$

Inserting Eq. 8.16

$$\Gamma_{\text{eff}}(\phi) = \frac{1}{2}\Big(\gamma_{x,0} + \gamma_{y,0} + \gamma_{x,b} + \gamma_{y,b} + |r_{\text{tot}}|\cos(2\phi+\theta)(\gamma_{x,0} - \gamma_{y,0})\Big), \tag{8.19}$$

From this, the visibility can be calculated, yielding

$$\nu\Gamma_{\text{eff}} = \text{abs}\left[\beta_y \frac{\Gamma_{y,0}}{(\Gamma_{x,0}+\Gamma_{y,0})} - \beta_x \frac{\Gamma_{x,0}}{(\Gamma_{x,0}+\Gamma_{y,0})}\right]|r_{\text{tot}}|, \tag{8.20}$$

where the following relationship is used

$$\beta_{x/y} = \frac{\gamma_{x/y,0}}{\Gamma_{x/y,0}} \rightarrow \gamma_{x/y,0} = \beta_{x/y}\Gamma_{x/y,0}. \tag{8.21}$$

The radiative rate for an $X-$ or $Y-$ oriented dipole differs only slightly as a function of the lateral offset, i.e. $\gamma_{x0} \simeq \gamma_{y0}$, thus for QDs located in the waveguide center, where $\beta_{x0} \simeq 0$, a good approximation is $\nu\gamma \simeq \frac{1}{2}\beta_{y0}|r_{\text{T}}|$. The count intensity is also modified due to the combined modulation of the two dipoles, resulting in:

$$\nu_{\text{I}} = \frac{2|r_{\text{T}}|}{1+|r_{\text{T}}|^2}\left|\frac{|e_y(y_0)|^2 - |e_x(y_0)|^2}{|e_y(y_0)|^2 + |e_x(y_0)|^2}\right|. \tag{8.22}$$

where e_x and e_y are the normalized electric field eigenmodes of the rectangular waveguide. Both visibilities have been computed numerically using finite element simulation of a rectangular waveguide and plotted in Fig. 8.1(d) for a mirror reflectivity of $r_{\text{T}} = 0.5$, which is the estimated value for the devices used in this work.

Fig. 8.2 shows a simulation of the phase- and reflectivity-dependent behavior of an emitter in a waveguide with a mirror. The color of the plot indicates $|r_{\text{tot}}|$, the absolute value of the reflectivity of the combined phase-shifter and photonic crystal mirror system. It can be seen by comparing Fig. 8.2(a) and Fig. 8.2(b) that the intensity modulation and decay rate modulation are correlated, that is, a phase shift that gives a large intensity will additionally lead to a high decay rate.

An intuitive understanding of this can be obtained by considering a standing wave between the quantum dot and the emitter. If the standing wave is in phase, leading

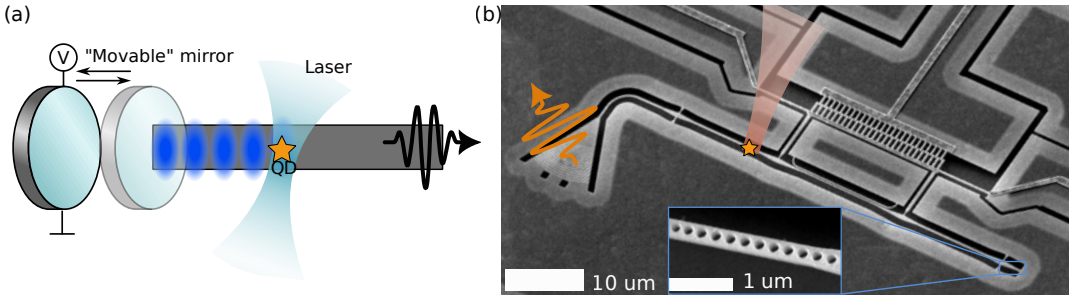

Figure 8.3: The designed device. A slot waveguide phase shifter is placed in between a SEG and a photonic crystal mirror. Emission properties of a quantum dot located before the phase shifter can be actively controlled via modulation of the phase.

to constructive interference between the outgoing wave emitted from the quantum dot and the outgoing wave reflected by the mirror, the intensity will rise. These conditions will additionally make the decay rate higher. If the standing wave is out of phase, leading to totally destructive interference between the outgoing wave emitted from the quantum dot and the outgoing wave reflected by the mirror, the intensity measured at the grating will fall to zero.

8.2 Experiment

On Fig. 8.3, the fabricated device is shown. The device consists of a set of shallow etched gratings (SEG), a NOEMS phase shifter, and a photonic crystal mirror. A pulsed laser is focused on the waveguide section between the SEG and the NOEMS phase shifter. Light is collected from the SEG, which is rotated by 90° compared to the rest of the device in order to minimize collection from backscattered light. By actuating the phase shifter, the effective path length between the QD and the photonic crystal mirror is changed, allowing tuning of the intensity and lifetime of the quantum dot. The total length of the device, from the bend just before the SEG to the beginning of the photonic crystal is 53 µm. The sample is wire-bonded to a printed circuit board and mounted inside a closed-cycle cryostat operating at 4 K. Excitation of the QDs is carried out with an above-band pulsed diode laser at 800 nm. The emitted light is collected from the SEG and analyzed in a Princeton Spectrometer SpectraPro 2500i. The grating is designed to collect only the fundamental transverse electric mode (TE0) while rejecting higher-order odd modes. For lifetime measurements, we included a tunable filter to select individual excitonic transitions and performed time-resolved spectroscopy with superconducting single-photon detectors (SSPD). All measurements are performed while sweeping the voltage that controls the phase shifter. A sample spectrum, showing several different quantum dots with different voltage-dependent responses, can be seen in Fig. 8.4.

To confirm that the measured light is, indeed, single photons, a second order correlation measurement was carried out, the results of which can be seen in Fig. 8.5. The g^2 was calculated to be $g^2 = 0.007 \pm 0.003$ As $g^2 < 0.5$ signifies antibunching for

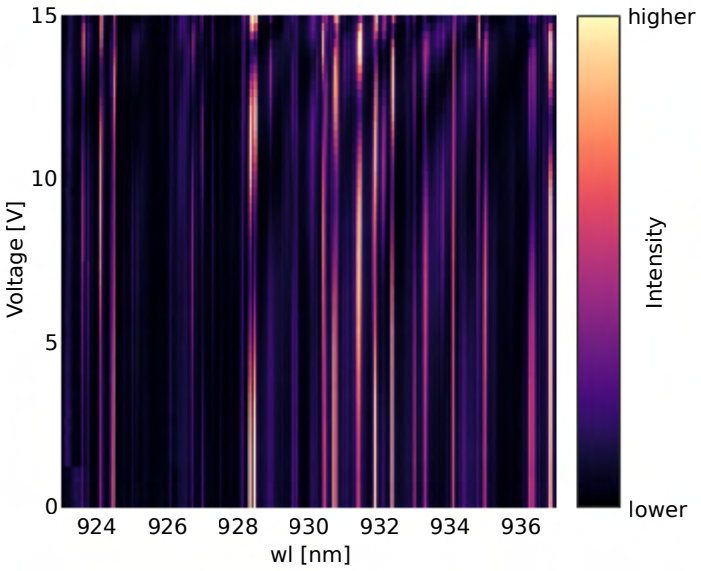

Figure 8.4: Sample spectrum showing several quantum dots with different voltage-dependent response. As the individual dots have very different intensities, each dot is normalized with respect to its individual maximum.

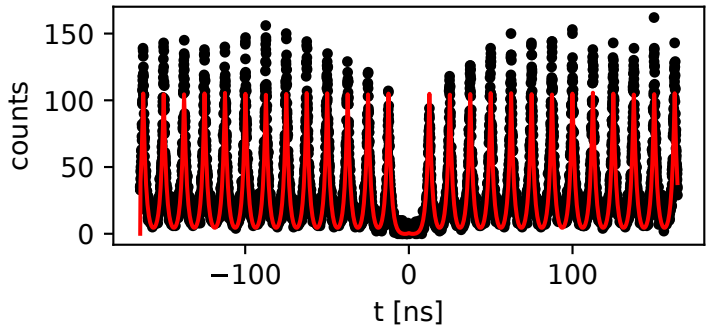

Figure 8.5: Fit to g2 for quantum dot

single photon sources, and $g^2 = 0$ signifies the ideal single photon source, this means that the photons emitted are highly antibunched single photons. Following this, the emission was fitted using a double exponential model, as detailed in Eq. 2.17

$$I(t) = A_f \cdot \exp\left(-\frac{t-t_0}{\tau_f}\right) + A_s \cdot \exp\left(-\frac{t-t_0}{\tau_s}\right) + B. \tag{8.23}$$

Here, the fast decay rate γ_f is due to the bright transition, while the slow rate γ_s probes the non-radiative decay rate from the dark exciton. A slow (> 1 μs, typically) spin-flip rate couples the bright and dark transitions, allowing us to accurately extract the radiative decay rate from $\gamma_{\mathrm{rad}} = \gamma_{\mathrm{f}} - \gamma_{\mathrm{s}}$ and the non-radiative rate from $\gamma_{\mathrm{nrad}} \simeq \gamma_{\mathrm{s}}$. As the laser is not perfect and instant, the shape of the laser will have an influence on the emission shape of the quantum dot. This is corrected for by obtaining a spectrum of

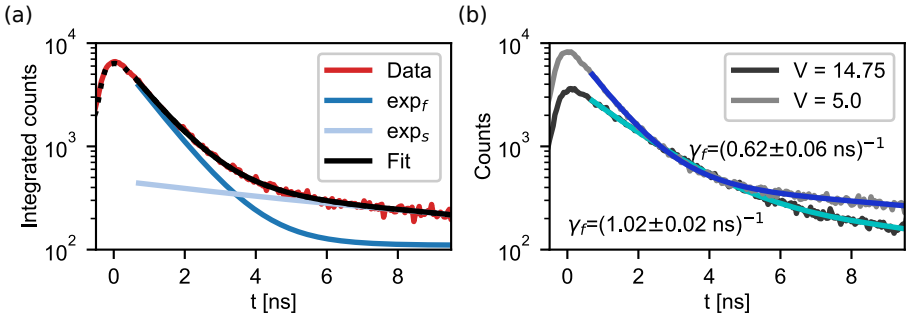

Figure 8.6: Sample raw data. a: Data, shown in red, compared to the fast (light blue) and slow (dark blue) decaying exponential obtained by fitting. The black line shows the fit, which is the sum of the slow and the fast exponential. Dotted black line shows the result of the fitting function applied outside the fitting interval. b: Comparison of the decay for the measurement with the highest decay rate (light grey, fitted with dark blue) and the measurement with the lowest decay rate (dark grey, fitted with teal).

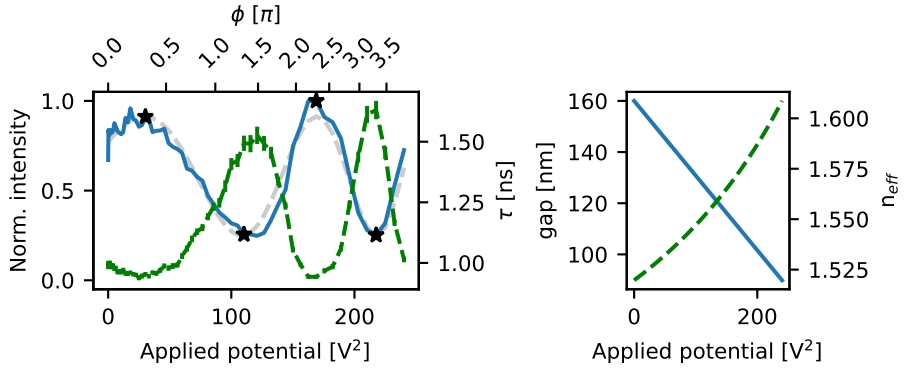

Figure 8.7: Modulation of intensity (blue continuous line) and lifetime (green dashed line) of sample quantum dot. a: Voltage-dependent lifetime and intensity. b: Calculated voltage-dependent gap and effective refractive index.

the emission of the laser, a so-called instrument response function (IRF). The fitting function is convoluted with the IRF.

$$I(t) = \left(A_f \cdot \exp\left(-\frac{t-t_0}{\tau_f} \right) + A_s \cdot \exp\left(-\frac{t-t_0}{\tau_s} \right) \right) * IRF(t) + B. \tag{8.24}$$

Fig. 8.6(a) shows sample raw data for a QD with an emission line at $\lambda = 923.45\,\text{nm}$, compared to the fitted exponential functions corresponding to respectively the slow decay rate γ_s (exp$_s$) and the fast decay rate γ_f (exp$_s$). Furthermore, Fig. 8.6(b) shows the time-resolved fluorescence for the two applied voltages corresponding to the highest and lowest intensities, which additionally were the voltages containing the highest and lowest decay rates. Fig. 8.7 shows the voltage-dependent modulation of the lifetime and intensity of the quantum dot shown in Fig. 8.6. It is evident that both lifetime and intensity follow the same oscillatory response, with a shorter (longer) lifetime at

QD	λ (nm)	γ_{max}	γ_{min}	v_γ	v_I
1	923.45	1.00±0.08	0.63±0.08	0.27±0.04	0.42
2	925.82	1.14±0.01	0.77±0.01	0.15±0.01	0.64
3	936.82	0.96±0.01	0.58±0.07	0.18±0.03	0.65
4	940.21	0.83±0.01	0.60±0.05	0.17±0.01	0.70
5	942.74	1.29±0.03	1.07±0.05	0.08±0.01	0.62
6	945.98	1.31±0.01	0.90±0.01	0.18±0.01	0.83

Table 8.1: Measured lifetime modulation for different QDs in the same device.

the corresponding highest (minimum) emission intensity. The lifetime is modulated between (1.00 ± 0.08) ns, when enhanced by the mirror and (1.53 ± 0.08) ns, when suppressed (i.e. over 50% modulation), with a total visibility of $v\gamma = (0.27 \pm 0.04)$. The visibility of the intensity is $v\mathrm{I} = (0.48 \pm 0.01)$, suggesting that the QD is likely offset by approximately 60 nm, laterally and $|r_\mathrm{T}| \sim 0.6$.

8.2.1 Conclusion of experiments

Table 8.1 shows measured emission properties for a series of QDs in the same device, spanning an emission wavelength range of ~ 20 nm. In section 7.4, the loss in the circuits is estimated to be around -1.1--1.3 dB per coupler. As the light passes the phase shifter, which contains two couplers, twice this is a total loss of -4.4--6 dB, corresponding to a maximum possible $|r_{tot}| = 0.60 - 0.50$ using the formula

$$|r_{tot}| = \sqrt{10^{\frac{L_{dB}}{10}}}. \tag{8.25}$$

Assuming that the reflectivity of the mirror and β_0 are both unity, this gives the following maximum possible visibilities of, respectively, the intensity and the decay rate in the single dipole case:

$$v_I = \frac{2|r_{tot}|}{1+|r_{tot}|^2} = 0.8 - 0.88, \tag{8.26}$$

and

$$v_\gamma = \beta_0 |r_{tot}| = 0.50 - 0.60. \tag{8.27}$$

Considering the presence of both x- and y-dipoles, the visibilities of respectively the intensity and the decay rate in of a y-dipole in the center of the waveguide is

$$v_I = \frac{2|r_{tot}|}{1+|r_{tot}|^2} = 0.8 - 0.88, \tag{8.28}$$

$$v_\gamma \approx \frac{1}{2}\beta_0 |r_{tot}| \approx 0.25 - 0.30. \tag{8.29}$$

8.3 Outlook

In this experiment, carried out with above-band laser excitation, the *x*- and *y*-dipoles are not distinguished between, as the fine structure splitting of < 5 GHz is too small to be resolved in the spectrometer. Hence, there is no direct way to measure the losses in our system and the ideal β-factor in waveguides. Nevertheless, from the observed visibilities, it can however be concluded that the overall reflectivity of the mirror is somewhere between 0.4 and 0.6, and that the QDs are likely distributed with different lateral offsets, potentially all the way to the edge of the waveguide. It should be noted that with the method presented in this work, combined with resonant excitation schemes, it would be possible to directly measure β for each emitter and potentially calculate the lateral offset. This would not only allow the direct control of spontaneous emission or emitter-photon coupling, but also could serve as a characterization tool to determine the best quantum emitter among randomly-distributed QD ensembles.

Chapter 9

Conclusion and Outlook

This thesis presented the design, fabrication, and experimental characterization of a nano-opto-electro-mechanical system (NOEMS) slot waveguide phase shifter implemented on a gallium arsenide (GaAs) platform. Utilizing the strong, nonlinear gap dependence of the effective refractive index in slot waveguides, a compact phase shifter with an active length of $L_{\text{slot}} = 10\,\mu\text{m}$ and a total footprint of less than $60 \times 20\,\mu\text{m}^2$ was realized.

The device demonstrated broadband performance at both room and cryogenic temperatures, with the wavelength interval investigated (37 nm at room temperature and 40 nm at $10:\text{K}$) primarily limited by the bandwidth of the shallow etch gratings used for chip-to-fiber coupling. At room temperature, the device exhibited a half-wave-voltage length product of $V_\pi L = 7.7 \cdot 10^{-3}\,\text{V} \cdot \text{cm}$ from zero actuation, with peak-to-peak switching achieved with a switching voltage 1.6 V using an applied bias of $V_b = 9\,\text{V}$. At cryogenic temperatures, the phase shifter demonstrated $V_\pi L = 0.012\,\text{V} \cdot \text{cm}$ from zero actuation. The reduced phase modulation observed at cryogenic temperatures is attributed to the significant stiffening of the gold membranes in the comb drive under low-temperature conditions.

In addition to the characterization of the phase shifter, which was carried out by investigating the interference fringes of an MZI with a phase shifter embedded in one arm, its application for actively controlling the emission properties of a quantum dot was demonstrated. By placing the phase shifter between a quantum dot and a photonic crystal mirror, the effective optical path length to the mirror was modulated. Quantum dots spanning a variety of lateral positions were investigated, with intensity and decay rate visibilities ranging from $\nu_I = 0.42$-0.83 and $\nu_\tau = 0.08$-0.27, respectively. These results showcase the ability to manipulate quantum dot emission properties using the NOEMS phase shifter.

In conclusion, this work represents a step toward scalable, low-temperature-compatible phase shifters for integrated quantum photonics, with applications ranging from quantum state manipulation to advanced photonic circuit architectures. Future research should focus on optimizing the couplers to achieve lower insertion losses, as the current designs exhibit losses in the range of -2.2 to $-3\,\text{dB}$, as measured with a CTL laser. Reducing these losses would significantly enhance the phase shifter's potential for integrated quantum photonic circuits. Moreover, decreasing the stiffness of the

comb drive or increasing the slot waveguide length would enable devices with lower actuation voltages, making them compatible with the voltage restrictions imposed by p-i-n wafers.

Bibliography

[1] Wikiquote contributors. *William Thomson — Misattributed Quotes*. [Accessed: 14-Jan-2025]. 2025. URL: https://en.wikiquote.org/wiki/William_Thomson#Misattributed.

[2] Albert A Michelson. "Register of the University of Chicago, 1895-1896". *Campbell Biology*. University of Chicago Press, 1896, p. 159.

[3] James D. Wells. *Prof. von Jolly's 1878 prediction of the end of Theoretical Physics as Reported by Max Planck*. University of Michigan Library, https://deepblue.lib.umich.edu/handle/2027.42/163719. Accessed: 2024-12-11. 2016.

[4] Michael Nauenberg. "Max Planck and the birth of the quantum hypothesis". *American Journal of Physics* 84.9 (Sept. 2016), pp. 709–720.

[5] A. Einstein. "Über einen die Erzeugung und Verwandlung des Lichtes betreffenden heuristischen Gesichtspunkt". *Annalen der Physik* 322.6 (1905), pp. 132–148.

[6] N. Bohr. "I. On the constitution of atoms and molecules". *The London, Edinburgh, and Dublin Philosophical Magazine and Journal of Science* 26.151 (1913), pp. 1–25.

[7] Louis de Broglie. "Recherches sue la Theorie Des Quantas". *Ann. de Phys.* (1925).

[8] W. Heisenberg. "Über quantentheoretische Umdeutung kinematischer und mechanischer Beziehungen". *Zeitschrift für Physik* 33.151 (1925), pp. 879–893.

[9] E. Schrödinger. "An Undulatory Theory of the Mechanics of Atoms and Molecules". *Phys. Rev.* 28 (6 Dec. 1926), pp. 1049–1070.

[10] W. Shockley. "The Theory of p-n Junctions in Semiconductors and p-n Junction Transistors". *Bell System Technical Journal* 28.3 (1949), pp. 435–489.

[11] Richard P. Feynman. "Simulating physics with computers". *International Journal of Theoretical Physics* 21.6 (June 1982), pp. 467–488.

[12] Peter W. Shor. "Polynomial-Time Algorithms for Prime Factorization and Discrete Logarithms on a Quantum Computer". *SIAM Journal on Computing* 26.5 (Oct. 1997), pp. 1484–1509.

[13] David P. DiVincenzo. "The Physical Implementation of Quantum Computation". *Fortschritte der Physik* 48.9-11 (2000), pp. 771–783.

[14] Ramón Aguado and Leo P. Kouwenhoven. "Majorana qubits for topological quantum computing". *Physics Today* 73.6 (June 2020), pp. 44–50. eprint: https://pubs.aip.org/physicstoday/article-pdf/73/6/44/10124104/44_1_online.pdf.

[15] Gabriel P. L. M. Fernandes, Alexandre C. Ricardo, Fernando R. Cardoso, and Celso J. Villas-Boas. *Trapped Ions as an Architecture for Quantum Computing*. 2022. arXiv: 2207.11619 [quant-ph]. URL: https://arxiv.org/abs/2207.11619.

[16] Morten Kjaergaard et al. "Superconducting Qubits: Current State of Play". *Annual Review of Condensed Matter Physics* 11.Volume 11, 2020 (2020), pp. 369–395.

[17] Sergei Slussarenko and Geoff J. Pryde. "Photonic quantum information processing: A concise review". *Applied Physics Reviews* 6.4 (Oct. 2019), p. 041303.

[18] E. Knill, R. Laflamme, and G. J. Milburn. "A scheme for efficient quantum computation with linear optics". *Nature* 409.6816 (Jan. 2001), pp. 46–52.

[19] Michael Reck, Anton Zeilinger, Herbert J. Bernstein, and Philip Bertani. "Experimental realization of any discrete unitary operator". *Phys. Rev. Lett.* 73 (1 July 1994), pp. 58–61.

[20] Jacques Carolan et al. "Universal linear optics". *Science* 349.6249 (2015), pp. 711–716.

[21] W. K. Wootters and W. H. Zurek. "A single quantum cannot be cloned". *Nature* 299.5886 (Oct. 1982), pp. 802–803.

[22] Peter Lodahl, Sahand Mahmoodian, and Søren Stobbe. "Interfacing single photons and single quantum dots with photonic nanostructures". *Rev. Mod. Phys.* 87 (2 May 2015), pp. 347–400.

[23] Ravitej Uppu et al. "Scalable integrated single-photon source". *Science Advances* 6.50 (2020), eabc8268.

[24] Peter Lodahl, Arne Ludwig, and Richard J. Warburton. "A deterministic source of single photons". *Physics Today* 75.3 (Mar. 2022), pp. 44–50.

[25] M. Arcari et al. "Near-Unity Coupling Efficiency of a Quantum Emitter to a Photonic Crystal Waveguide". *Phys. Rev. Lett.* 113 (9 Aug. 2014), p. 093603.

[26] Ying Wang et al. "Electroabsorption in gated GaAs nanophotonic waveguides". *Applied Physics Letters* 118.13 (Mar. 2021), p. 131106.

[27] Camille Papon et al. "Nanomechanical single-photon routing". *Optica* 6.4 (Apr. 2019), pp. 524–530.

[28] Pierre Edinger et al. "Silicon photonic microelectromechanical phase shifters for scalable programmable photonics". *Opt. Lett.* 46.22 (Nov. 2021), pp. 5671–5674.

[29] Dong Uk Kim et al. "Programmable photonic arrays based on microelectromechanical elements with femtowatt-level standby power consumption". *Nature Photonics* 17.12 (Dec. 2023), pp. 1089–1096.

[30] Hamed Sattari et al. “Silicon Photonic MEMS Phase-Shifter”. *Opt. Express* 27.13 (June 2019), pp. 18959–18969.

[31] Thomas Grottke, Wladick Hartmann, Carsten Schuck, and Wolfram H. P. Pernice. “Optoelectromechanical phase shifter with low insertion loss and a 13pi tuning range”. *Opt. Express* 29.4 (Feb. 2021), pp. 5525–5537.

[32] Reza Baghdadi et al. “Dual slot-mode NOEM phase shifter”. *Opt. Express* 29.12 (June 2021), pp. 19113–19119.

[33] Georg A. Reider. *Photonics*. Springer, 2016.

[34] Koen Alexander et al. *A manufacturable platform for photonic quantum computing*. 2024. arXiv: 2404.17570 [quant-ph]. URL: https://arxiv.org/abs/2404.17570.

[35] S. Bogdanov, M. Y. Shalaginov, A. Boltasseva, and V. M. Shalaev. “Material platforms for integrated quantum photonics”. *Opt. Mater. Express* 7.1 (Jan. 2017), pp. 111–132.

[36] Zian Xiao et al. “Recent Progress in Silicon-Based Photonic Integrated Circuits and Emerging Applications”. *Advanced Optical Materials* 11.20 (2023), p. 2301028.

[37] Syed Ahamed and Victor Lawrence. “Impact of Fiber Optic Technology”. Jan. 1997, pp. 503–557. ISBN: 978-1-4613-7888-4.

[38] Alberto Politi et al. “Silica-on-Silicon Waveguide Quantum Circuits”. *Science* 320.5876 (May 2008), pp. 646–649.

[39] Aviad Katiyi and Alina Karabchevsky. “Passive and Active Materials for Advanced Photonic Integrated Circuitry in Visible and Near-Infrared”. *Encyclopedia of Materials: Electronics*. Ed. by A.S.M.A. Haseeb. Oxford: Academic Press, 2023, pp. 193–202. ISBN: 978-0-12-819735-6.

[40] M. Cazzanelli et al. “Second-harmonic generation in silicon waveguides strained by silicon nitride”. *Nature Materials* 11.2 (Feb. 2012), pp. 148–154.

[41] E. Timurdogan, C. V. Poulton, M. J. Byrd, and M. R. Watts. “Electric field-induced second-order nonlinear optical effects in silicon waveguides”. *Nature Photonics* 11.3 (Mar. 2017), pp. 200–206.

[42] A. Boretti, Q. Li, and S. Castelletto. “Pioneering the future with silicon carbide integrated photonics”. *Optics and Laser Technology* 181 (2025), p. 111910.

[43] Zhenda Xie et al. “Recent development in integrated Lithium niobate photonics”. *Advances in Physics: X* 9.1 (2024), p. 2322739.

[44] Sina Saravi, Thomas Pertsch, and Frank Setzpfandt. “Lithium Niobate on Insulator: An Emerging Platform for Integrated Quantum Photonics”. *Advanced Optical Materials* 9.22 (2021), p. 2100789.

[45] Wikipedia User Benjah-bmm27. *File:Sphalerite-unit-cell-depth-fade-3D-balls.png*. [Accessed: 13/01 2025]. 2007. URL: https://commons.wikimedia.org/wiki/File:Sphalerite-unit-cell-depth-fade-3D-balls.png.

[46] Jasprit Singh. *Electronic and Optoelectronic Properties of Semiconductor Structures*. Cambridge University Press, 2003.

[47] Kaustubh Vyas et al. "Group III-V semiconductors as promising nonlinear integrated photonic platforms". *Advances in Physics: X* 7.1 (2022), p. 2097020.

[48] Tiantian Wang, Huading Song, and Ke He. "Structural design and molecular beam epitaxy growth of GaAs and InAs heterostructures for high mobility two-dimensional electron gas". *Quantum Frontiers* 3.1 (July 2024), p. 13.

[49] Atefeh Shadmani et al. "Integration of GaAs waveguides on a silicon substrate for quantum photonic circuits". *Opt. Express* 30.21 (Oct. 2022), pp. 37595–37602.

[50] Noel H. Wan et al. "Large-scale integration of artificial atoms in hybrid photonic circuits". *Nature* 583.7815 (July 2020), pp. 226–231.

[51] Stefan Preble et al. "5 - Passive silicon photonic devices". *Integrated Photonics for Data Communication Applications*. Ed. by Madeleine Glick, Ling Liao, and Katharine Schmidtke. Integrated Photonics Apps Specific Design and Manufacturing. Elsevier, 2023, pp. 159–199.

[52] Emmanuel Rosencher and Borge Vinter. *Optoelectronics*. Ed. by P. G.Translator Piva. Cambridge University Press, 2002.

[53] T. Alasaarela et al. "Reduced propagation loss in silicon strip and slot waveguides coated by atomic layer deposition". *Opt. Express* 19.12 (June 2011), pp. 11529–11538.

[54] Vilson R. Almeida, Qianfan Xu, Carlos A. Barrios, and Michal Lipson. "Guiding and confining light in void nanostructure". *Opt. Lett.* 29.11 (June 2004), pp. 1209–1211.

[55] *Specification sheet for the Thorlabs HP 780 optical fiber*. [Accessed: 27/12 2024]. URL: https://www.thorlabs.com/drawings/72df2226bad235d4-539E2889-A4A1-196C-A97F7EC0559179B9/780HP-SpecSheet.pdf.

[56] Riccardo Marchetti et al. "Coupling strategies for silicon photonics integrated chips, Invited". *Photon. Res.* 7.2 (Feb. 2019), pp. 201–239.

[57] Haoyang Sun, Qifeng Qiao, Qingze Guan, and Guangya Zhou. "Silicon Photonic Phase Shifters and Their Applications: A Review". *Micromachines* 13.9 (2022).

[58] H HAFFNER, C ROOS, and R BLATT. "Quantum computing with trapped ions". *Physics Reports* 469.4 (Dec. 2008), pp. 155–203.

[59] Sergei Slussarenko and Geoff J. Pryde. "Photonic quantum information processing: A concise review". *Applied Physics Reviews* 6.4 (Oct. 2019), p. 041303.

[60] Mikael Afzelius, Nicolas Gisin, and Hugues de Riedmatten. "Quantum memory for photons". *Physics Today* 68.12 (Dec. 2015), pp. 42–47.

[61] Lian-Ao Wu, Philip Walther, and Daniel A. Lidar. "No-go theorem for passive single-rail linear optical quantum computing". *Scientific Reports* 3.1 (Mar. 2013), p. 1394.

[62] Tim C. Ralph and Geoff J. Pryde. “Chapter 4 - Optical Quantum Computation”. Vol. 54. Progress in Optics. Elsevier, 2010, pp. 209–269.

[63] Hao Yu, Alexander O. Govorov, Hai-Zhi Song, and Zhiming Wang. “Time-encoded photonic quantum states: Generation, processing, and applications”. *Applied Physics Reviews* 11.4 (Nov. 2024), p. 041318.

[64] Xiaojiong Chen, Zhaorong Fu, Qihuang Gong, and Jianwei Wang. “Quantum entanglement on photonic chips: a review”. *Advanced Photonics* 3.6 (2021), p. 064002.

[65] Pieter Kok et al. “Linear optical quantum computing with photonic qubits”. *Rev. Mod. Phys.* 79 (1 Jan. 2007), pp. 135–174.

[66] R. HANBURY BROWN and R. Q. TWISS. “Correlation between Photons in two Coherent Beams of Light”. *Nature* 177.4497 (Jan. 1956), pp. 27–29.

[67] Christopher Gerry and Peter Knight. *Introductory Quantum Optics*. Cambridge University Press, 2004.

[68] Jiefei Zhang et al. “On-chip scalable highly pure and indistinguishable single-photon sources in ordered arrays: Path to quantum optical circuits”. *Science Advances* 8.35 (2022), eabn9252.

[69] C. K. Hong, Z. Y. Ou, and L. Mandel. “Measurement of subpicosecond time intervals between two photons by interference”. *Phys. Rev. Lett.* 59 (18 Nov. 1987), pp. 2044–2046.

[70] Nicolas Gisin, Grégoire Ribordy, Wolfgang Tittel, and Hugo Zbinden. “Quantum cryptography”. *Rev. Mod. Phys.* 74 (1 Mar. 2002), pp. 145–195.

[71] Alex McMillan et al. “Chapter 12 - Four-Wave Mixing in Single-Mode Optical Fibers”. *Single-Photon Generation and Detection*. Ed. by Alan Migdall, Sergey V. Polyakov, Jingyun Fan, and Joshua C. Bienfang. Vol. 45. Experimental Methods in the Physical Sciences. Academic Press, 2013, pp. 411–465.

[72] Christophe Couteau. “Spontaneous parametric down-conversion”. *Contemporary Physics* 59.3 (2018), pp. 291–304.

[73] Fumihiro Kaneda, Karina Garay-Palmett, Alfred B. U’Ren, and Paul G. Kwiat. “Heralded single-photon source utilizing highly nondegenerate, spectrally factorable spontaneous parametric downconversion”. *Opt. Express* 24.10 (May 2016), pp. 10733–10747.

[74] Daniel A. Vajner et al. “On-Demand Generation of Indistinguishable Photons in the Telecom C-Band Using Quantum Dot Devices”. *ACS Photonics* 11.2 (Feb. 2024), pp. 339–347.

[75] Martin Esmann, Stephen C. Wein, and Carlos Antón-Solanas. “Solid-State Single-Photon Sources: Recent Advances for Novel Quantum Materials”. *Advanced Functional Materials* 34.30 (2024), p. 2315936.

[76] M. D. Eisaman, J. Fan, A. Migdall, and S. V. Polyakov. "Invited Review Article: Single-photon sources and detectors". *Review of Scientific Instruments* 82.7 (July 2011), p. 071101.

[77] J. McKeever et al. "Deterministic Generation of Single Photons from One Atom Trapped in a Cavity". *Science* 303.5666 (2004), pp. 1992–1994.

[78] Greta Andrini et al. "Solid-State Color Centers for Single-Photon Generation". *Photonics* 11.2 (2024).

[79] I Aharonovich et al. "Diamond-based single-photon emitters". *Reports on Progress in Physics* 74.7 (June 2011), p. 076501.

[80] Pascale Senellart, Glenn Solomon, and Andrew White. "High-performance semiconductor quantum-dot single-photon sources". *Nature Nanotechnology* 12.11 (Nov. 2017), pp. 1026–1039.

[81] P. W. Fry et al. "Inverted Electron-Hole Alignment in InAs-GaAs Self-Assembled Quantum Dots". *Phys. Rev. Lett.* 84 (4 Jan. 2000), pp. 733–736.

[82] F. Ding et al. "Tuning the Exciton Binding Energies in Single Self-Assembled InGaAs/GaAs Quantum Dots by Piezoelectric-Induced Biaxial Stress". *Phys. Rev. Lett.* 104 (6 Feb. 2010), p. 067405.

[83] Gabija Kiršansk˙e. "Electrical control of excitons in semiconductor nanostructures". PhD thesis. University of Copenhagen, Jan. 2016.

[84] P. B. Joyce et al. "Composition of InAs quantum dots on GaAs(001): Direct evidence for (In,Ga)As alloying". *Phys. Rev. B* 58 (24 Dec. 1998), R15981–R15984.

[85] J. X. Chen et al. "Tuning InAs/GaAs quantum dot properties under Stranski-Krastanov growth mode for 1.3 micron applications". *Journal of Applied Physics* 91.10 (May 2002), pp. 6710–6716.

[86] T. Pregnolato et al. "Deterministic positioning of nanophotonic waveguides around single self-assembled quantum dots". *APL Photonics* 5.8 (Aug. 2020), p. 086101.

[87] Lukas Novotny and Bert Hecht. *Principles of Nano-Optics*. 2nd ed. Cambridge University Press, 2012.

[88] J S Blakemore. "Semiconducting and other major properties of gallium arsenide". *Journal of Applied Physics* 53.10 (Oct. 1982), R123–R181.

[89] Z. M. Fang et al. "Photoluminescence of InSb, InAs, and InAsSb grown by organometallic vapor phase epitaxy". *Journal of Applied Physics* 67.11 (June 1990), pp. 7034–7039.

[90] S.T. Harry and Martins Adekanmbi. "Confinement Energy of Quantum Dots and the Brus Equation". *International Journal of Research -GRANTHAALAYAH* 8 (Dec. 2020), pp. 318–323.

[91] Xueyong Yuan et al. "Uniaxial stress flips the natural quantization axis of a quantum dot for integrated quantum photonics". *Nature Communications* 9.1 (Aug. 2018), p. 3058.

[92] M. Bayer et al. “Fine structure of neutral and charged excitons in self-assembled In(Ga)As/(Al)GaAs quantum dots”. *Phys. Rev. B* 65 (19 May 2002), p. 195315.

[93] Paul A. Dalgarno et al. “Dark exciton decay dynamics of a semiconductor quantum dot”. *physica status solidi (a)* 202.14 (2005), pp. 2591–2597.

[94] D.F. Walls and Gerard J. Milburn. *Quantum Optics*. Springer, 2008.

[95] Thang B. Hoang, Gleb M. Akselrod, and Maiken H. Mikkelsen. “Ultrafast Room-Temperature Single Photon Emission from Quantum Dots Coupled to Plasmonic Nanocavities”. *Nano Letters* 16.1 (Jan. 2016), pp. 270–275.

[96] Daniel Najer et al. “A gated quantum dot strongly coupled to an optical microcavity”. *Nature* 575.7784 (Nov. 2019), pp. 622–627.

[97] Xing Ding et al. “On-Demand Single Photons with High Extraction Efficiency and Near-Unity Indistinguishability from a Resonantly Driven Quantum Dot in a Micropillar”. *Phys. Rev. Lett.* 116 (2 Jan. 2016), p. 020401.

[98] Nicholas C. Harris et al. “Linear programmable nanophotonic processors”. *Optica* 5.12 (Dec. 2018), pp. 1623–1631.

[99] Leonardo Midolo, Albert Schliesser, and Andrea Fiore. “Nano-opto-electro-mechanical systems”. *Nature Nanotechnology* 13.1 (Jan. 2018), pp. 11–18.

[100] Richard A. Campos, Bahaa E. A. Saleh, and Malvin C. Teich. “Quantum-mechanical lossless beam splitter: SU(2) symmetry and photon statistics”. *Phys. Rev. A* 40 (3 Aug. 1989), pp. 1371–1384.

[101] T. Gruner and D.-G. Welsch. “Quantum-optical input-output relations for dispersive and lossy multilayer dielectric plates”. *Phys. Rev. A* 54 (2 Aug. 1996), pp. 1661–1677.

[102] Ravitej Uppu, Tom A. W. Wolterink, Tristan B. H. Tentrup, and Pepijn W. H. Pinkse. “Quantum optics of lossy asymmetric beam splitters”. *Opt. Express* 24.15 (July 2016), pp. 16440–16449.

[103] Michael A. Nielsen and Isaac L. Chuang. *Quantum Computation and Quantum Information: 10th Anniversary Edition*. Cambridge University Press, 2010.

[104] Andrés Macho, Daniel Pérez-López, and José Capmany. “Optical Implementation of 2×2 Universal Unitary Matrix Transformations”. *Laser and Photonics Review* (May 2021).

[105] William R. Clements et al. “Optimal design for universal multiport interferometers”. *Optica* 3.12 (Dec. 2016), pp. 1460–1465.

[106] David A. B. Miller. “Perfect optics with imperfect components”. *Optica* 2.8 (Aug. 2015), pp. 747–750.

[107] Roel Burgwal et al. “Using an imperfect photonic network to implement random unitaries”. *Opt. Express* 25.23 (Nov. 2017), pp. 28236–28245.

[108] Shengping Liu et al. “Thermo-optic phase shifters based on silicon-on-insulator platform: state-of-the-art and a review”. *Frontiers of Optoelectronics* 15.1 (Apr. 2022), p. 9.

[109] Michael R. Watts et al. “Adiabatic thermo-optic Mach and #x2013;Zehnder switch”. *Opt. Lett.* 38.5 (Mar. 2013), pp. 733–735.

[110] SungWon Chung, Makoto Nakai, and Hossein Hashemi. “Low-power thermo-optic silicon modulator for large-scale photonic integrated systems”. *Opt. Express* 27.9 (Apr. 2019), pp. 13430–13459.

[111] Shi Zhao, Jingye Chen, Daoxin Dai, and Yaocheng Shi. “Low-loss and power-efficient phase shifter based on an optimized multimode spiral silicon waveguide”. *Opt. Lett.* 48.17 (Sept. 2023), pp. 4653–4656.

[112] Gorachand Ghosh. “Temperature dispersion of refractive indices in semiconductors”. *Journal of Applied Physics* 79.12 (June 1996), pp. 9388–9389.

[113] Sidney Lourenço et al. “Thermal Expansion Contribution to the Temperature Dependence of Excitonic Transitions in GaAs and AlGaAs”. *Brazilian Journal of Physics* 34 (June 2004), pp. 517–525.

[114] M. Thomaschewski and S. I. Bozhevolnyi. “Pockels modulation in integrated nanophotonics”. *Applied Physics Reviews* 9.2 (May 2022), p. 021311.

[115] Leonardo Midolo et al. “Electro-optic routing of photons from a single quantum dot in photonic integrated circuits”. *Opt. Express* 25.26 (Dec. 2017), pp. 33514–33526.

[116] Mitsuru Takenaka et al. “III–V/Si Hybrid MOS Optical Phase Shifter for Si Photonic Integrated Circuits”. *J. Lightwave Technol.* 37.5 (Mar. 2019), pp. 1474–1483.

[117] H I Ralph. “On the theory of the Franz-Keldysh effect”. *Journal of Physics C: Solid State Physics* 1.2 (Apr. 1968), p. 378.

[118] Shun Lien Chuang. “Efficient band-structure calculations of strained quantum wells”. *Phys. Rev. B* 43 (12 Apr. 1991), pp. 9649–9661.

[119] Wolfram H.P. Pernice and Harish Bhaskaran. “1 - Introduction to phase change photonics”. *Phase Change Materials-Based Photonic Computing*. Ed. by Harish Bhaskaran and Wolfram H.P. Pernice. Materials Today. Elsevier, 2024, pp. 1–10. ISBN: 978-0-12-823491-4.

[120] Carlos A. Ríos Ocampo and Nathan Youngblood. “4 - Configuring phase-change materials for photonics”. *Phase Change Materials-Based Photonic Computing*. Ed. by Harish Bhaskaran and Wolfram H.P. Pernice. Materials Today. Elsevier, 2024, pp. 67–117. ISBN: 978-0-12-823491-4.

[121] Carlos Ríos et al. “Ultra-compact nonvolatile phase shifter based on electrically reprogrammable transparent phase change materials”. *PhotoniX* 3.1 (Oct. 2022), p. 26.

[122] Shengru Zhou et al. “Reconfigurable mode converter based on a Sb2Se3 phase change material and inverse design”. *Opt. Express* 32.20 (Sept. 2024), pp. 35903–35914.

[123] Zhuoran Fang et al. “Ultra-low-energy programmable non-volatile silicon photonics based on phase-change materials with graphene heaters”. *Nature Nanotechnology* 17.8 (Aug. 2022), pp. 842–848.

[124] Rui Chen et al. *Low-loss multilevel operation using lossy PCM-integrated silicon photonics*. 2024. arXiv: 2402.08803 [physics.optics]. URL: https://arxiv.org/abs/2402.08803.

[125] Haoyang Sun, Qifeng Qiao, Qingze Guan, and Guangya Zhou. “Silicon Photonic Phase Shifters and Their Applications: A Review”. *Micromachines* 13.9 (2022).

[126] Yunda Wang, Ming Kong, and Yung-Chen Lee. “Thermal Stress in MEMS”. *Encyclopedia of Thermal Stresses*. Ed. by Richard B. Hetnarski. Dordrecht: Springer Netherlands, 2014, pp. 5237–5248.

[127] Lakshmi Swaminathan. “RF MEMS Switch Fabrication and Packaging”. *Nanofibers*. Ed. by Brajesh Kumar. Rijeka: IntechOpen, 2020. Chap. 15.

[128] Jeremy Walraven et al. “Electrostatic discharge/electrical overstress susceptibility in MEMS: a new failure mode”. *Proceedings of SPIE - The International Society for Optical Engineering* (Jan. 2000).

[129] James Vinson and J.J. Liou. “Electrostatic discharge in devices: Protection techniques”. *Proceedings of the IEEE* 88 (Jan. 2001), pp. 1878–1902.

[130] Jonatan Piasetzky et al. *Robust Characterization of Integrated Photonics Directional Couplers*. 2024. arXiv: 2412.11670 [physics.optics]. URL: https://arxiv.org/abs/2412.11670.

[131] A. Hardy and W. Streifer. “Coupled mode theory of parallel waveguides”. *Journal of Lightwave Technology* 3.5 (1985), pp. 1135–1146.

[132] Patrick Steglich. “Silicon-on-Insulator Slot Waveguides: Theory and Applications in Electro-Optics and Optical Sensing”. *Emerging Waveguide Technology*. Ed. by Kok Yeow You. Rijeka: IntechOpen, 2018. Chap. 10.

[133] Karel Van Acoleyen et al. “Ultracompact Phase Modulator Based on a Cascade of NEMS-Operated Slot Waveguides Fabricated in Silicon-on-Insulator”. *IEEE Photonics Journal* 4 (2012), pp. 779–788.

[134] Vinay Bhatia et al. “Design and Simulation of Capacitive MEMS Switch for Ka Band Application”. *Wireless Communications and Mobile Computing* 2021.1 (2021), p. 2021513.

[135] Z. Charles Ying, Mark G. Reitsma, and Richard S. Gates. “Direct measurement of cantilever spring constants and correction for cantilever irregularities using an instrumented indenter”. *Review of Scientific Instruments* 78.6 (June 2007), p. 063708.

[136] Ville Kaajakari. *MEMS Tutorial:Pull-in voltage in electrostatic microactuators*. [Accessed: 13/12 2024]. URL: http://www.kaajakari.net/~ville/research/tutorials/pull_in_tutorial.pdf.

[137] Konstantinos Tsoukalas, Babak Vosoughi Lahijani, and Søren Stobbe. "Impact of Transduction Scaling Laws on Nanoelectromechanical Systems". *Phys. Rev. Lett.* 124 (22 June 2020), p. 223902.

[138] Melinda Baldwin. "What it took to be a NASA computer". *Physics Today* (Jan. 2017).

[139] *August 1946: The Moore School Lectures*. [Accessed: 13/12 2024]. URL: https://www.aps.org/archives/publications/apsnews/200208/history.cfm.

[140] *Pioneering photolithography for 7nm chips*. [Accessed: 12/01 2025]. 2021. URL: https://projects.research-and-innovation.ec.europa.eu/en/projects/success-stories/all/pioneering-photolithography-7nm-chips.

[141] Xiaoyan Zhou et al. "High-efficiency shallow-etched grating on GaAs membranes for quantum photonic applications". *Applied Physics Letters* 113.25 (2018), p. 251103.

[142] L Midolo, T Pregnolato, G Kiršanskė, and S Stobbe. "Soft-mask fabrication of gallium arsenide nanomembranes for integrated quantum photonics". *Nanotechnology* 26.48 (Nov. 2015), p. 484002.

[143] A. Pimpin and W. Srituravanich. "Review on Micro- and Nanolithography Techniques and Their Applications". *Eng. J* 16.1 (2011).

[144] Harry Levinson. *Principles of lithography: Third edition*. SPIE, Jan. 2011, pp. 1–505. ISBN: 9780819483249.

[145] Inc. MKS Instruments. *Semiconductor Devices and Process Technology*. MKS Instruments, Inc, 2007.

[146] Iason Giannopoulos et al. "Extreme ultraviolet lithography reaches 5 nm resolution". *Nanoscale* 16 (33 2024), pp. 15533–15543.

[147] Seung Lee and R. Sankaran. "Direct writing via electron-driven reactions". *Materials Today* 16 (Apr. 2013), pp. 117–122.

[148] Sergio O. Martinez-Chapa, Arnoldo Salazar, and Marc J. Madou. "Chapter 13.2 - Two-Photon Polymerization as a Component of Desktop Integrated Manufacturing Platforms". *Three-Dimensional Microfabrication Using Two-photon Polymerization*. Ed. by Tommaso Baldacchini. Micro and Nano Technologies. Oxford: William Andrew Publishing, 2016, pp. 374–416. ISBN: 978-0-323-35321-2.

[149] Ripon Kumar Dey and Bo Cui. "Stitching error reduction in electron beam lithography with in-situ feedback using self-developing resist". *Journal of Vacuum Science and Technology B* 31.6 (Nov. 2013), 06F409.

[150] *Elionix ELS F 125 Datasheet*. [Accessed: 18/0½ 2025]. 2024. URL: https://sts-elionix.com/product/els-f125/.

[151] Araldo van de Kraats and Raghunath Murali. *Proximity effect in e-beam lithography*. Nanotechnoogy Research Center, Georgia Institute of Technoogy, 2005.

[152] Stephen A. Campbell. *Fabrication Engineering at the Micro- and Nanoscale*. Oxford University Press, 2012.

[153] Vincent M. Donnelly and Avinoam Kornblit. "Plasma etching: Yesterday, today, and tomorrow". *Journal of Vacuum Science and Technology A* 31.5 (Sept. 2013), p. 050825.

[154] Katarzyna Racka-Szmidt et al. "A Review: Inductively Coupled Plasma Reactive Ion Etching of Silicon Carbide". *Materials* 15.1 (2022).

[155] Ijaz H. Jafri, Heinz Busta, and Steven T. Walsh. "Critical point drying and cleaning for MEMS technology". *MEMS Reliability for Critical and Space Applications*. Ed. by Russell A. Lawton, William M. Miller, Gisela Lin, and Rajeshuni Ramesham. Vol. 3880. International Society for Optics and Photonics. SPIE, 1999, pp. 51–58.

[156] *Surface Tension of Solvents*. [Accessed: 5/12 2024]. 2024. URL: https://macro.lsu.edu/howto/solvents/Surface%20Tension.html.

[157] Grégory Abadias et al. "Review Article: Stress in thin films and coatings: Current status, challenges, and prospects". *Journal of Vacuum Science and Technology A* 36.2 (Mar. 2018), p. 020801.

[158] COMSOL Multiphysics Encyclopedia. *Analysis of Deformation in Solid Mechanics*. [Accessed: 11/01 2025]. URL: https://www.comsol.com/multiphysics/analysis-of-deformation.

[159] Henrik Sönnerlind. *What Is Geometric Nonlinearity?* [Accessed: 04/01 2025]. URL: https://www.comsol.com/blogs/what-is-geometric-nonlinearity.

[160] Yongke Sun, Scott E Thompson, and Toshikazu Nishida. *Strain effect in semiconductors: theory and device applications*. Springer Science and Business Media, 2009.

[161] Milan Jirásek. *Basic concepts and equations of solid mechanics*. Accessed: 2025-01-12. 2007. URL: https://mech.fsv.cvut.cz/~milan/regc07-1.pdf.

[162] E. V. Moiseeva, Y. M. Senousy, Shamus Mcnamara, and Cindy K. Harnett. "Single-mask microfabrication of three-dimensional objects from strained bimorphs". *Journal of Micromechanics and Microengineering* 17 (2007).

[163] RE Mihailovich, T Koscica, and RJ Zeto. "Measurement of the elastic stress of thin films deposited on gallium arsenide". *Journal of Vacuum Science and Technology A: Vacuum, Surfaces, and Films* 14.4 (1996), pp. 2483–2487.

[164] W. A. Strifler and C. W. Bates. "Stress in evaporated films used in GaAs processing". *Journal of Materials Research* 6.3 (Mar. 1991), pp. 548–552.

[165] Ioffe Institute. *Gallium Arsenide - Thermal properties*. Accessed: 2025-01-12. URL: https://www.ioffe.ru/SVA/NSM/Semicond/GaAs/thermal.html.

[166] Jack Ekin. *Experimental Techniques for Low-Temperature Measurements: Cryostat Design, Material Properties and Superconductor Critical-Current Testing*. Oxford University Press, Oct. 2006. ISBN: 9780198570547.

[167] Celeste Qvotrup et al. “Curved GaAs cantilever waveguides for the vertical coupling to photonic integrated circuits”. *Opt. Express* 32.3 (Jan. 2024), pp. 3723–3734.

[168] Tomoya Yoshida et al. “Vertical silicon waveguide coupler bent by ion implantation”. *Opt. Express* 23.23 (Nov. 2015), pp. 29449–29456.

[169] Saeed Sharif Azadeh et al. “Microcantilever-integrated photonic circuits for broadband laser beam scanning”. *Nature Communications* 14.1 (May 2023), p. 2641.

[170] Matt Saha et al. *Nanophotonic waveguide chip-to-free-space beam scanning at 68 Million Spots/(s·mm^2)*. 2024. arXiv: 2406.17662 [physics.optics].

[171] Aslı D Uğurlu et al. “Suspended Spot-Size Converters for Scalable Single-Photon Devices”. *Advanced Quantum Technologies* 3.2 (2020).

[172] Camille Papon et al. “Supplementary material to Nanomechanical single-photon routing”. *Optica* (2019).

[173] COMSOL Multiphysics Documentation. Accessed: 2025-01-18. URL: https://doc.comsol.com/5.5/doc/com.comsol.help.rf/rf_ug_theory.06.12.html.

[174] R. Palmer et al. “Low-Loss Silicon Strip-to-Slot Mode Converters”. *IEEE Photonics Journal* 5.1 (2013), pp. 2200409–2200409.

[175] Guo-qiu Jiang et al. “Comprehensive measurement of the near-infrared refractive index of GaAs at cryogenic temperatures”. *Opt. Lett.* 48.13 (July 2023), pp. 3507–3510.

[176] R I Cottam and G A Saunders. “The elastic constants of GaAs from 2 K to 320 K”. *Journal of Physics C: Solid State Physics* 6.13 (July 1973), p. 2105.

[177] Julien G. Noel. “Review of the properties of gold material for MEMS membrane applications”. *IET Circuits, Devices and Systems* 10.2 (2016), pp. 156–161.

[178] A. Bogozi et al. “Elastic modulus study of gold thin film for use as an actuated membrane in a Superconducting RF MEM switch”. *IEEE Transactions on Applied Superconductivity* 15.2 (2005), pp. 980–983.

[179] Rodrigo A. Thomas, Celeste Qvotrup, Zhe Liu, and Leonardo Midolo. “Noise Performance of On-Chip Nano-Mechanical Switches for Quantum Photonics Applications”. *Advanced Quantum Technologies* n/a.n/a (2024), p. 2400012.

[180] Celeste Qvotrup et al. “Nanomechanical Phase Shifting on a Gallium Arsenide Platform”. *The 25th European Conference on Integrated Optics*. June 2024.

[181] Fabian Beutel et al. “Cryo-compatible opto-mechanical low-voltage phase-modulator integrated with superconducting single-photon detectors”. *Opt. Express* 30.17 (Aug. 2022), pp. 30066–30074.

[182] Jianwei Wang, Fabio Sciarrino, Anthony Laing, and Mark G Thompson. “Integrated photonic quantum technologies”. *Nature Photonics* 14.5 (2020), pp. 273–284.

[183] Ravitej Uppu et al. "Quantum-dot-based deterministic photon–emitter interfaces for scalable photonic quantum technology". *Nature nanotechnology* 16.12 (2021), pp. 1308–1317.

[184] Stephanie Simmons. "Scalable fault-tolerant quantum technologies with silicon color centers". *PRX Quantum* 5.1 (2024), p. 010102.

[185] P. W. Milonni. "Why spontaneous emission?" *American Journal of Physics* 52.4 (Apr. 1984), pp. 340–343.

[186] Theodore A. Welton. "Some Observable Effects of the Quantum-Mechanical Fluctuations of the Electromagnetic Field". *Phys. Rev.* 74 (9 Nov. 1948), pp. 1157–1167.

[187] E. M. Purcell. "Spontaneous Emission Probabilities at Radio Frequencies". *Physical Review* 69 (1946).

[188] K.H. Drexhage. "Influence of a dielectric interface on fluorescence decay time". *Journal of Luminescence* 1-2 (1970), pp. 693–701.

[189] Yuntian Chen et al. "Finite-element modeling of spontaneous emission of a quantum emitter at nanoscale proximity to plasmonic waveguides". *Physical Review B—Condensed Matter and Materials Physics* 81.12 (2010), p. 125431.

[190] Thomas Hümmer, FJ García-Vidal, Luis Martín-Moreno, and David Zueco. "Weak and strong coupling regimes in plasmonic QED". *Physical Review B—Condensed Matter and Materials Physics* 87.11 (2013), p. 115419.

Appendix A

Comparison of BCW Devices

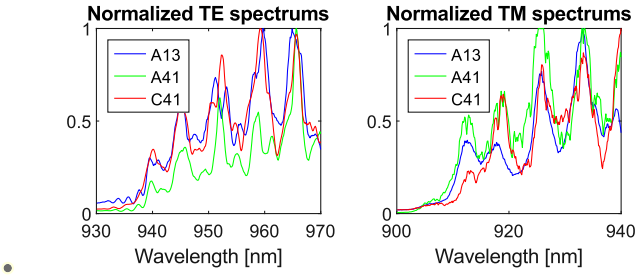

Figure A.1: Comparison of the normalized intensity of respectively the TE and TM mode for several different bent cantilever coupler devices.

During the characterization of the vertical bending couplers, several devices were investigated. Fig. A.1 shows the normalized intensity of the cutoff at room temperatures for several different devices. The tether distance and whether the device contains an epoxy tether coupler can be seen in Table A.1. While the different devices show different intensity distributions at different wavelengths, they all exhibit cutoffs at roughly the same wavelengths, making it unlikely that the cutoff are dependent on the tether distance or the presence of epoxy tipping.

	A_{13}	A_{41}	C_{41}
Epoxy Tipping	Yes	Yes	No
Tether distance	10 µm	15 µm	15 µm

Table A.1: Comparison of the design parameters for the three different devices compared in figure A.1

Appendix B

Derivation of the Lifetime of an Emitter near a Mirror

The spontaneous emission of a quantum emitter can be described in terms of Green's Tensor using Fermi's golden rule

$$\gamma = \frac{\pi \omega_A |\mathbf{d}|^2}{3\hbar\varepsilon_0} \rho(\mathbf{r}_0 \omega_A) \tag{B.1}$$

where $G_{1D}(x,x',\omega)$ is the partial local density of optical states (partial LDOS),

$$\rho(\mathbf{r}_0 \omega_A) = \frac{6\omega_A}{\pi c^2} \left[\mathbf{n}_\mathbf{d}^* \cdot \mathrm{Im} \overleftrightarrow{\mathbf{G}}(\mathbf{r}_0, \mathbf{r}_0; \omega_A) \cdot \mathbf{n}_\mathbf{d} \right]. \tag{B.2}$$

Here, ω_A is the energy between the ground state and excited state of the two-level system of the emitter, $\mathbf{d}$ is the transition dipole moment, $\mathbf{d} = \langle g|\hat{\mathbf{d}}|e\rangle$, $\mathbf{n_d}$ the unit vector of the transition dipole moment vector such that $\mathbf{d} = |\mathbf{d}|\mathbf{n_d}$, $\mathbf{r}_0$ the position of the emitter and $\overleftrightarrow{\mathbf{G}}(\mathbf{r}_0, \mathbf{r}_0; \omega_A)$ Green's function at the location of the emitter. Here, ω_A is the energy between the ground state and excited state of the two-level system of the emitter, $\mathbf{d}$ is the transition dipole moment, $\mathbf{d} = \langle g|\hat{\mathbf{d}}|e\rangle$, $\mathbf{n_d}$ the unit vector of the transition dipole moment vector such that $\mathbf{d} = |\mathbf{d}|\mathbf{n_d}$, $\mathbf{r}_0$ the position of the emitter and $\overleftrightarrow{\mathbf{G}}(\mathbf{r}_0, \mathbf{r}_0; \omega_A)$ Green's function at the location of the emitter. In an 1D waveguide oriented along the x-axis, Green's function is [189, 190]

$$\overleftrightarrow{\mathbf{G}}(\mathbf{r}_0, \mathbf{r}_0; \omega_A) = \frac{c^2}{\omega v_g N} \mathbf{E}(y,z) \left[\mathbf{E}^T(y',z') \right]^* k G_{1D}(x,x',\omega). \tag{B.3}$$

Here N is the normalization factor

$$N = \int \mathrm{d}y\, \mathrm{d}z\, \varepsilon_r(y,z) |\mathbf{E}(y,z)|^2 \tag{B.4}$$

and $G_{1D}(x,x',\omega)$ the one-dimensional Green's function,

$$G_{1D}(x,x',\omega) = \frac{\mathbf{i}}{2k} \exp(\mathrm{i}k|x-x'|) \tag{B.5}$$

The presence of the mirror at $x = L$ can be modeled using a mirror dipole placed at $x = 2L$ away from the position of the dipole. Due to the superposition principle, this can be modeled using a similar Green's function located at $x = 2L$, with a phase shift to account for the accumulated phase and a reflection coefficient $|r_t|$

$$\overleftrightarrow{\mathbf{G}}(0,0;\omega_A)_{TOT} = \overleftrightarrow{\mathbf{G}}(0,0;\omega_A) \pm |r_{tot}|\mathrm{e}^{\mathrm{i}2\phi}\overleftrightarrow{\mathbf{G}}(0,2L;\omega_A), \tag{B.6}$$

Here the + is in the case of an x-dipole, and the - is in the case of a y-dipole. Assuming we have a TE-mode, which has the largest electrical field in the polarization transverse to the waveguide (i.e. the y-axis), the perturbed decay rate of the quantum dot can be derived

$$\begin{aligned}\frac{\gamma_{x/y,\phi}}{\gamma_{x/y,0}} = \frac{\rho_{x/y,\phi}}{\rho_{x/y,0}} &= \frac{\left[\mathbf{n}_\mathbf{d}^* \cdot \mathrm{Im}\left(\overleftrightarrow{\mathbf{G}}(0,0;\omega_A) - |r_{tot}|\mathrm{e}^{\mathrm{i}2\phi}\overleftrightarrow{\mathbf{G}}(0,2L;\omega_A)\right)\cdot\mathbf{n}_\mathbf{d}\right]}{\left[\mathbf{n}_\mathbf{d}^* \cdot \mathrm{Im}\,\overleftrightarrow{\mathbf{G}}(0,0;\omega_A)\cdot\mathbf{n}_\mathbf{d}\right]}, \\ &= \frac{\mathrm{Im}\left(G_{1D}(0,0,\omega) - |r_{tot}|\mathrm{e}^{i2\phi}G_{1D}(0,2L,\omega)\right)}{\mathrm{Im}\left(G_{1D}(0,0,\omega)\right)}, \\ &= 1 - |r_{tot}|\cos(2\phi+\theta).\end{aligned} \tag{B.7}$$